

May 2023

Characterization of Hematite Coated Bedrock Fault Scarps in the Northern Colorado River Extensional Corridor Near Lake Mead, Nevada

Molly E. Pickerel

Follow this and additional works at: <https://digitalscholarship.unlv.edu/thesesdissertations>



Part of the [Geology Commons](#)

Repository Citation

Pickerel, Molly E., "Characterization of Hematite Coated Bedrock Fault Scarps in the Northern Colorado River Extensional Corridor Near Lake Mead, Nevada" (2023). *UNLV Theses, Dissertations, Professional Papers, and Capstones*. 4759.

<http://dx.doi.org/10.34917/36114784>

This Thesis is protected by copyright and/or related rights. It has been brought to you by Digital Scholarship@UNLV with permission from the rights-holder(s). You are free to use this Thesis in any way that is permitted by the copyright and related rights legislation that applies to your use. For other uses you need to obtain permission from the rights-holder(s) directly, unless additional rights are indicated by a Creative Commons license in the record and/or on the work itself.

This Thesis has been accepted for inclusion in UNLV Theses, Dissertations, Professional Papers, and Capstones by an authorized administrator of Digital Scholarship@UNLV. For more information, please contact digitalscholarship@unlv.edu.

CHARACTERIZATION OF HEMATITE COATED BEDROCK FAULT SCARPS IN THE
NORTHERN COLORADO RIVER EXTENSIONAL CORRIDOR NEAR LAKE MEAD,
NEVADA

By

Molly E. Pickerel

Bachelor of Science in Geology
University of Oregon
2019

A thesis submitted in partial fulfillment
of the requirements for the

Master of Science - Geoscience

Department of Geoscience
College of Sciences
The Graduate College

University of Nevada, Las Vegas
May 2023



Thesis Approval

The Graduate College
The University of Nevada, Las Vegas

April 5, 2023

This thesis prepared by

Molly E. Pickerel

entitled

Characterization of Hematite Coated Bedrock Fault Scarps in the Northern Colorado River Extensional Corridor Near Lake Mead, Nevada

is approved in partial fulfillment of the requirements for the degree of

Master of Science - Geoscience
Department of Geoscience

Margaret Odum, Ph.D.
Examination Committee Chair

Tomas Capaldi, Ph.D.
Examination Committee Member

Pamela Burnley, Ph.D.
Examination Committee Member

Karen Harry, Ph.D.
Graduate College Faculty Representative

Alyssa Crittenden, Ph.D.
*Vice Provost for Graduate Education &
Dean of the Graduate College*

ABSTRACT

Fault mirrors are reflective, thin, typically <1 mm thick, fault slip surfaces in exhumed fault zones that can provide a record of thermal, chemical, and rheological changes to fault materials during deformation. This study investigates a series of hematite coated fault mirrors along bedrock fault scarps in Miocene volcanic rocks near Lake Mead, Nevada. The studied faults are located in a structurally complex area that includes NE-SW trending left-lateral strike-slip faults of the Lake Mead fault system, NW-SE right-lateral strike-slip faults of the Las Vegas Shear Zone, and N-S striking extensional faults of the Northern Colorado River Extensional Corridor.

New zircon U-Pb ages from fault scarp host rocks 21-BC-03 and 21-BC-05 are 13.86 ± 0.27 Ma and 12.90 ± 0.31 Ma (2σ standard error), respectively. New apatite (U-Th)/He dates range from 5.64 ± 0.46 Ma to 12.4 ± 0.36 Ma (2σ standard error) and are interpreted to be partially reset after eruption due to reheating. Inverse thermal history modeling in HeFTy of apatite He dates indicates a thermal history of reheating to ~ 65 °C which is interpreted as shallow burial around $\sim 11 - 5$ Ma followed by cooling to the surface, interpreted as exhumation between $\sim 4.5 - 2$ Ma. The zircon U-Pb ages, apatite He dates, and inverse thermal history models indicate the fault host rocks were erupted to the surface and stayed within the upper ~ 2 km of the crust since the Miocene.

Nearly vertical fault scarps that host the fault mirror surfaces exhibit two sets of slickenlines, indicating oblique and strike-slip motion, with different orientations indicating that there have been multiple episodes of deformation along the surfaces. Three of the five studied fault scarps have E-W orientations, and one scarp is NW-SE, and one is NE-SW striking. The studied faults are interpreted to have been active during deformation associated with the Lake Mead Fault System and the Las Vegas Valley Shear Zone at $13 - 9$ Ma and record both strike slip and oblique

slip events in the complex strain field during this time. Micro-nano scale texture and grain morphology analysis of the hematite fault mirror volumes shows extreme strain localization along the fault mirror surface. Some fault mirrors exhibit multiple domains separated by discrete slip surfaces. Comminution and cataclasis appear to be the dominant deformation mechanisms in the fault mirror volume. Hematite textures and morphologies are consistent with observations from other fault systems that are interpreted to record aseismic to sub-seismic slip rates, and relatively low coseismic temperature rise. Fluid injection veins and post-deformation FeO mineralization in fractures are interpreted as evidence of high fluid pressures during slip and fluid circulation post-deformation. The new geochronologic and microstructural data inform on the processes operating along discrete fault surfaces in the shallow crust since the Miocene in the Lake Mead region.

ACKNOWLEDGEMENTS

The efforts of many individuals contributed to the success of this thesis project. I'd like to officially acknowledge them here out of appreciation for their expertise and help.

First, my advisor, Dr. Margo Odlum, for introducing me to the world of fault mirrors and guiding me through this learning process. My committee members, Dr. Tomas Capaldi, Dr. Pamela Burnley, and Dr. Karen Harry, deserve recognition for their continued support. A special thank you to Dr. Joel Desormeau of the University of Nevada, Reno for his microscopy assistance and time; Dr. Uttam Chowdry of the University of Arizona for his instruction and analysis help; Dr. Doug Sims of the College of Southern Nevada for his availability and offering his facilities; Odinaka Okwueze for his time, patience, and mineral separation expertise; and Dr. Minghua Ren of the University of Nevada, Las Vegas for his microscopy assistance. I'd like to thank Dr. Marisa Acosta of the University of Lausanne for being an amazing mentor and always making herself available to help. Finally, all of my friends and family who have supported me through graduate school.

TABLE OF CONTENTS

Abstract	iii
Acknowledgments.....	v
List of Tables	viii
List of Figures	ix
I. Introduction	1
II. Background	5
II.I. Hematite and Iron Oxides in Fault Zones	5
II.II. Geologic Settings	9
III. Samples and Methodology.....	15
III.I. Fieldwork	15
III.II. SEM/EDS Methodology	15
III.III. Mineral Separation/Dating Methodology	17
III.IV. U-Pb Zircon Geochronology	17
III.V. (U-Th)/He Thermochrometry	18
IV. Results	21
IV.I. Fieldwork	21
IV.II. SEM/EDS	30
IV.III. U-Pb Zircon Dating	38
IV.IV. (U-Th)/He Apatite Dating	41
IV.V. Thermal History Modeling	43
V. Discussion	45
V.I. Geologic History	45

V.II. Faulting History	46
V.III. Fault Processes and Deformation Mechanisms	49
V.IV. Recommended Future Work	51
VI. Conclusion	53
Appendix	54
References	67
Curriculum Vitae	74

LIST OF TABLES

Table 1. Timeline of major tectonic events in the Lake Mead region	10
Table 2. K-Ar ages from Lake Mead area	13
Table 3. U-Pb Zircon analysis results for 21-BC-03	39
Table 4. (U-Th)/He Apatite analysis results	41
Table A1. U-Pb Zircon Analysis Raw data	58
Table A2. (U-Th)/He Apatite Analysis Raw data.....	60
Table A3. U-Pb Zircon analysis results for 21-BC-05	65

LIST OF FIGURES

Figure 1. Anatomy of a brittle fault	1
Figure 2. Hematite textures and morphologies observed at the SEM scale	2
Figure 3. SEM images of different hematite grain morphologies and textures	7
Figure 4. Digital elevation model Map of the Lake Mead region	8
Figure 5. Map of the sample locations and study area in Lake Mead region	11
Figure 6. The volcanic column of Patsy Mine Volcanics	14
Figure 7. Field figure of 21-BC-01	22
Figure 8. Field figure of 21-BC-02	23
Figure 9. Field figure of 21-BC-03	24
Figure 10. Field figure of 21-BC-04	25
Figure 11. Field figure of 21-BC-05	27
Figure 12. Stereonet of average sample site orientations	28
Figure 13. Stereonet of average volcanic bedding orientations	29
Figure 14. Fault mirror domains of 21-BC-01	30
Figure 15. Multi-scale cross-section SEM images of 21-BC-01	31
Figure 16. Multi-scale cross-section SEM images of 21-BC-02	33
Figure 17. Multi-scale cross-section SEM images of 21-BC-04	35
Figure 18. Multi-scale cross-section SEM images of 21-BC-05	36
Figure 19. SEM images of slickenlines on fault mirror surface	36
Figure 20. Wetherill Concordia plots of zircon U-Pb ages from the volcanic host rock.....	40
Figure 21. (U-Th)/He Apatite results plots	42
Figure 22. HeFTy inverse model results	44

Figure 23. E-W orientated fault measurement comparison	48
Figure A1. EDS map of 21-BC-03 aliquot	54
Figure A2. EDS map of 21-BC-05 aliquot	55
Figure A3. EDS results from 21-BC-04	56
Figure A4. EDS results from 21-BC-02	57
Figure A5. Multiscale BSE SEM images of 21-BC-03	63

I. INTRODUCTION

Fault systems in the brittle crust are networks of slip surfaces and fractures experiencing different degrees of deformation as they accommodate deformation, migration of fluids, stress, and sometimes seismicity (Sibson, 1983; Faulkner et al., 2010; Thakur et al., 2020). Deformation in some fault zones occurs within the damage zones on either side of the fault with highest degrees of strain increasing towards the principal slip surface at the fault core (Fig.1; Thakur et al., 2020). Principal slip zones (PSZ) occur as thin, discrete regions of shear deformation (<10 cm) that accommodate most of the displacement along the upper-crustal faults (Fig. 1; Knipe, 2006; Verberne et al., 2019). PSZs play a critical role in the nucleation and spreading of earthquakes along faults (Brace and Byerlee, 1966; Fagereng and Toy, 2011; Verberne et al., 2019).

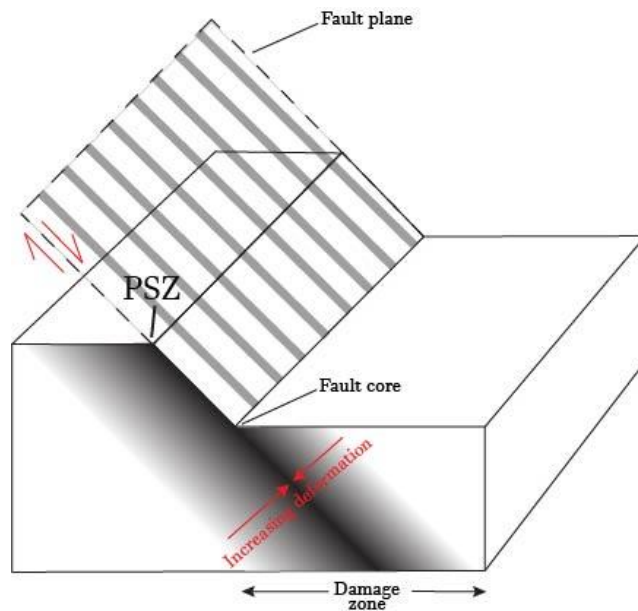


Figure 2. Anatomy of a brittle fault.

This diagram highlights the principle slip zone (PSZ), fault plane, fault core, and damage zone with increasing strain localization and deformation towards the fault core. Adapted from Verberne et al., 2019.

It has been shown that discrete slip events in the upper crust can occur within a thin, <1-5mm thick, highly granulated fault core (Knipe, 2006). It has also been shown that the mineralogic composition and geochemistry of the fault zone plays a significant role in fault strength during the seismic cycle (Rice, 2006; Faulkner et al., 2010; Gonclaves et al., 2015). Exhumed fault rocks, especially exhumed PSZs, can serve as a record of thermal, chemical, and mechanical processes associated with deformation and fault slip (e.g., Rowe & Griffith, 2015; McDermott et al., 2017; Ault, 2020).

Faults experience slip at different rates, from aseismic creep or subseismic slip ($\sim 10^{-10}$ m/s – 10^{-12} m/s) to seismic slip rates (10^{-4} m/s – 10^1 m/s), which can leave textural and/or geochemical signatures in the rock record (Rowe & Griffith, 2015). Microtextures/microstructures from the slip surfaces record can provide information about the deformation mechanisms operative during fault slip (Knipe, 1989; Sibson, 1983; Fagereng and Toy, 2011; Ault, 2020; Odlum et al., 2021).

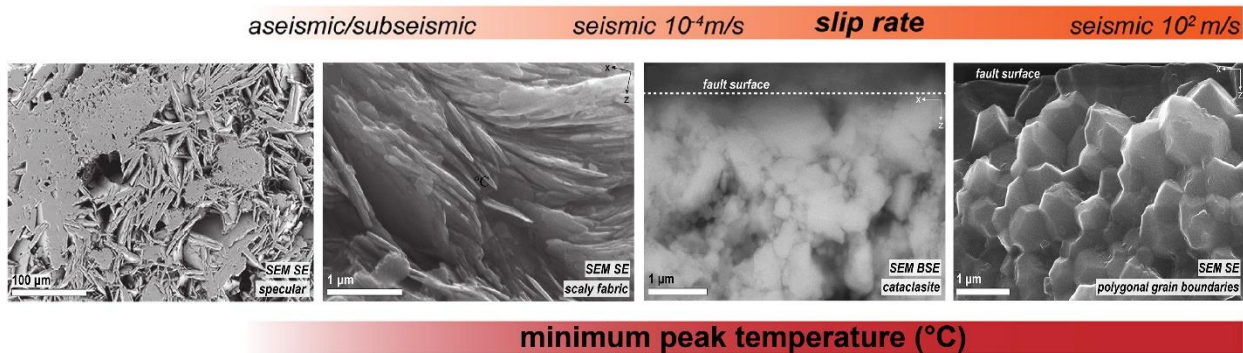


Figure 3. Hematite textures and morphologies observed at the SEM scale.

These features may represent different slip rates and coseismic temperature rise along faults. The table shows frictional heating temperature proxies for minimum peak temperatures associated with different slip rates shown in the orange bar. The proxies are based on heating rates on the order of 10s–100 s °C/m. Data from (1) Ishikawa et al. (2008), (2) Kameda et al. (2011), (3) Evans et al. (2014), (4) Savage et al. (2014), (5) Sheppard et al. (2015), (6) Rabinowitz et al., (2017), (7) Savage and Polissar (2019), (8) Collettini et al., (2013), (9) Isambert et al., (2003), (10) McIntosh et al. (1990), (11) Grim and Bradley (1940), (12) Ault et al., (2015), (13) McDermott et al. (2017); (Grim and Bradley, 1940; McIntosh et al., 1990; Isambert et al., 2003; Ishikawa et al., 2008; Kameda et al., 2011). Adapted from Ault, 2020.

Deformation mechanisms active on brittle faults include, but are not limited to, melting, recrystallization or annealing, cataclasis, frictional sliding, crystal plastic deformation, asperity flash heating, and solution creep (Knipe, 2006; Fagereng and Toy, 2011; Rowe and Griffith, 2015; McDermott et al., 2017; Ault, 2020; Odlum et al., 2021). Therefore, micro-scale to nano-scale textural analysis of exhumed thin slip fault surfaces can aid in interpretation of processes that may be active during slip, including potential dynamic weakening mechanisms, along the slip surfaces in the shallow crust (Ault et al., 2019; Ault, 2020; Odlum et al., 2021). This evidence combined with thermochronometric and/or geochronological analysis can aid in illustrating the depths and timing of deformation and the thermal and mechanical fault history (McDermott et al., 2017; Ault et al., 2019; Ault, 2020; Odlum et al., 2021).

Fault mirrors are one type of thin (typically <1 mm thick) slip surface that can represent the PSZ or slip surfaces within the damage zone in exhumed fault zones and have been observed in a variety of rock types at a variety of scales (cm² to m²) (e.g., Simon-Tov et al., 2013; Ault et al., 2016, 2019; Odlum et al., 2021). Fault mirrors are light reflective surfaces made up of layers of nanoparticles and their presence has sometimes been interpreted as an indication of seismicity in the rock record (Siman-Tov et al., 2013; Ault et al., 2016, 2019). Studies on naturally deformed rocks and laboratory experiments indicate that fault mirrors form during a range of slip conditions after friction is reduced (Siman-Tov et al., 2013; Ault et al., 2016). The formation of fault mirrors, both natural and experimental, have been observed to form under a process beginning with abrading the surface which reduces roughness and forms striations oriented in the direction of movement (i.e., slickenlines) (Siman-Tov et al., 2013).

This study aims to understand the evolution of locally mirrored hematite coated faults along the Old Historic Railroad Trail, Lake Mead National Preserve, through multi-scale structural,

geochemical, and textural characterization, geochronology, and low-temperature thermochronometry. The integration of observations and analytical data indicate highly localized deformation within the hematite rich zones and along discrete slip surfaces through comminution and cataclasis. These factors may govern the dynamic weakening of the fault strength and the propagation of slip along these shallow crustal faults.

II. BACKGROUND

II.1 Hematite and Iron Oxides in Fault Zones

The abundance of oxygen, hydrogen, and iron in Earth's crust has resulted in iron oxides and iron hydroxides being common occurrences in many geological environments (Guo et al., 2013). Of the 14 known iron oxides and iron hydroxides, hematite, goethite, and magnetite are the most common rock-forming minerals (Guo et al., 2013). Hematite formation is dependent on redox conditions: iron mobility requires reducing conditions, and secondary hematite mineralization precipitates from oxidizing fluids circulating through faults and fracture networks with high permeability (Cornell and Schwertmann, 2003; Catling and Moore, 2003; Guo et al., 2013;). Faults and fractures in the crust can be fluid pathways, so iron oxides are common secondary phases in fault and fracture zones (e.g., Ault, 2020). Hematite precipitation can occur at a range of crustal depths and fluid temperatures, making hematite occurrence in faults possible over an array of crustal depths and temperature conditions (Ault et al., 2016, 2019; Ault, 2020; Odlum et al., 2021). Investigation into hematite properties through deformation experiments has shown that hematite is generally weak with a coefficient of friction of $\mu = 0.28 \pm 0.12$ over a range of slip velocities (0.1 – 320 mm/s) and displacements (Calzolari et al, 2020). Since hematite is weak, strain can be localized along hematite rich zones and/or veins (McDermott et al., 2017). At high pressures at higher temperatures, hematite produces significant strain weakening (Gonclaves et al., 2015; Odlum et al., 2021). Lab deformation experiments show that presence of even minor amounts of hematite (≥ 5 %) within a polyaggregate matrix can localize strain (Gonclaves et al., 2015).

Previous work on hematite coated fault surfaces has characterized hematite grain morphologies and textures through Backscatter (BSE) and Secondary (SE) Scanning Electron Microscopy (SEM) (McDermott et al., 2017; Moser et al., 2017; Ault et al., 2015; 2019; Odlum et

al., 2021) (Fig. 3; Ault et al., 2019; surface (e.g., McDermott et al., 2017; Moser et al., 2017; Calzolari et al., 2018; Ault et al., 2016, 2019; Ault, 2020; Odlum et al., 2021). Hematite grain textures and morphologies on the fault surface and within the hematite rich volume, or the fault mirror (FM) volume, are influenced by fault activity, deformation mechanisms, presence or absence of fluids, and the ambient and co-slip thermal conditions (Ault, 2020; Fig. 2). A common mineralization grain morphology is specular hematite “plates”, sometimes clusters of these plates with preferred orientation forming botryoidal bubbles (Ault, 2020; Fig. 3A, 3B). A ‘scaly’ fabric with a preferred orientation in the direction of slip on the fault surface is interpreted to record aseismic slip and little to no post-mineralization temperature rise (figure 3C; Ault, 2020). A cataclasite texture, the result of a comminution of grains leading to a fuzzy ultra-fine-grained texture, is common along the fault surface as a result of fluid interaction, friction, and/or heat and can occur at a variety of slip rates (Fig. 3E; Ault, 2020). Polygonal grain morphologies developed from annealing and/or recrystallization are indicative of recrystallization and/or annealing and high coseismic temperature rise, and thus high slip rates (600 – >1000 °C) (Fig. 3F; McDermott et al., 2017; Ault, 2020).

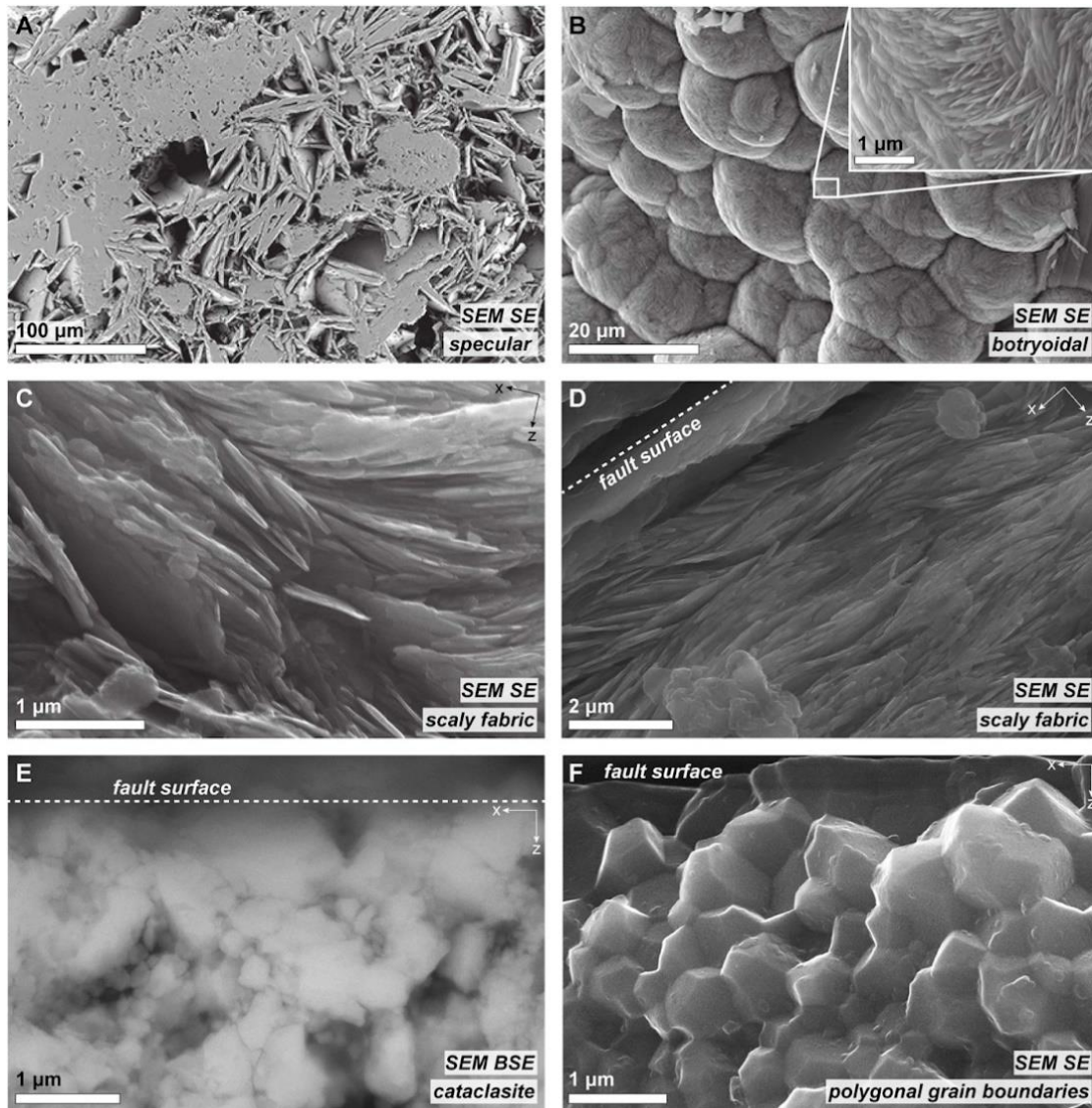


Figure 3. SEM images of different hematite grain morphologies and textures.

These features observed are indicative of mineralization and post-mineralization conditions. A) Specular hematite plates and B) Botryoidal texture made up of hematite plates which are indicative of original mineralization morphologies. C) Scaly fabric texture from a fault showing preferred orientation of the principal slip direction. D) Scaly fabric texture near the slip surface showing preferred orientation to the principal slip direction, interpreted to represent aseismic to sub-seismic slip rate. E) Cataclasite texture at a fault surface, interpreted to record comminution during post-mineralization deformation. F) Polygonal grain boundaries at a fault surface interpreted to indicate high coseismic temperatures at seismic slip rates and subsequent post-seismic annealing. Adapted from Ault, 2020.

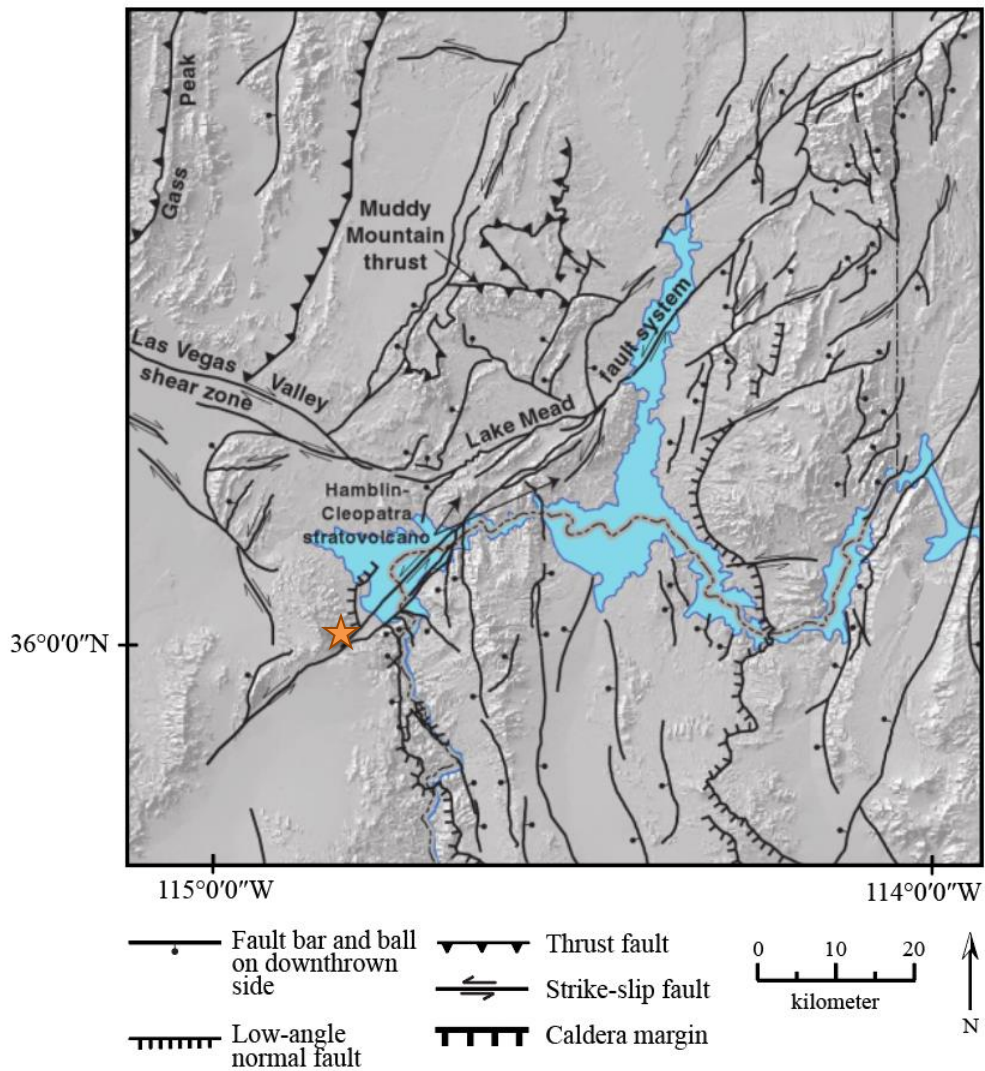


Figure 4. Digital elevation model Map of the Lake Mead region.

This map highlights the major regional fault systems including the NW-SE striking Las Vegas Valley shear zone, the NE-SW striking Lake Mead Fault zone, and the N-S extension of the Colorado River Extensional Corridor (CREC). The field area is designated by the orange star. Adapted from Felger and Beard, 2010.

II.II Geologic Setting

The western North American Cordillera experienced major periods of extension and magmatism in the Cenozoic, particularly the mid-late Miocene (Weber and Smith, 1987; Wernicke et al., 1987; Gans and Bohrson, 1998; Faulds et al., 2001). The field area is within the Lake Mead region which lies in the southeastern section of the Basin and Range which is a vast extensional province spanning most of the southwestern United States and into Mexico (e.g., Bohannon, 1979; Faulds et al., 2001). The Lake Mead area is located within the Northern Colorado River Extensional Corridor (CREC) and is considered to be in the eastern domain of the Walker Lane region (Faulds et al., 2001; Faulds and Henry, 2008). The CREC contains normal faults and nearly vertical blocks of the upper crust that have undergone extensive extension (>100% elongation; Gans and Bohrson, 1998).

The study area has a structurally complicated strain field of both dextral and sinistral shear, N-S shortening, and E-W extension (Faulds and Henry, 2008). The tectonic history of the Lake Mead region since ~19 Ma with associated features is summarized in Table 1. A significant amount of the deformation in this area occurred during the Miocene, when the CREC underwent multiple stages of episodic volcanism and magmatism before, during, and after major periods of crustal extension (Anderson et al., 1972; Faulds et al., 2001). The early Miocene is characterized by the largest amount of volcanism accompanied by a minor amount of north-south extension and development of E-W striking faults (Faulds et al., 2001). The mid-Miocene was marked by substantial magnitudes of east-west extension and the development of N-S striking faults that experienced tilt rates of 80 °/m.y. in the early extensional stages (Faulds et al., 2001; Zuza et al., 2019). Within the CREC, extension was accommodated along west-dipping normal fault systems in the north and east-dipping normal fault systems in the south which coalesce and dissipate in the

Black Mountain accommodation zone (Faulds et al., 2001). The Lake Mead region is north of the Black Mountain accommodation zone and characterized by west-dipping faults and east-tilted units that are (Faulds et al., 2001).

Event	Time (Ma)	Geologic Features
Pre-extension volcanism, sedimentation	~18.5 - 15.2	Pre-extension sedimentary basins formed on upper Paleozoic and Mesozoic rocks to north of Kingman uplift, volcanism and plutonism to south in area of uplift
Syn-extension volcanism, sedimentation	16 - 12	Syn-extension sedimentary basins to north, volcanism and plutonism to south
Extension-related normal and strike-slip faulting (peak at ~15 Ma)	~16 - 10	Lake Mead fault system, Las Vegas Valley shear zone, Saddle Island fault, smaller normal and strike-slip faults
Continued strike-slip faulting	10 - 6 or younger	Lake Mead fault system and LVVSZ continue to evolve
Late to post-extension volcanism	12 - 8	Mafic volcanism
Late to post-extension basin deposition	10 - 6	Syn- to post-extension sedimentation
Integration of Colorado River and development of modern landscape	6 - 0	Downcutting and deposition, development of modern landscape

Table 1. Timeline of major tectonic events in the Lake Mead region.

Associated geologic features in the Lake Mead Region. Adapted from Beard et al., 2014.

Initial upper crustal extension began in the Lake Mead region around 16 Ma and increased to a peak period around 12 Ma, then decreased until 9 Ma and resulted in 100% elongation in this area (Weber and Smith, 1987; Fuerbach et al., 1993; Gans and Bohrsen, 1998; Faulds et al., 2001). Major east-west extension in the western region of Lake Mead occurred between 14-12 Ma as evidenced by significant tilting (Faulds et al., 2001). The period of maximum extension was not

accompanied by volcanism (Duebendorfer and Wallin, 1991; Fuerbach et al., 1993; Gans and Bohrsen, 1998; Faulds et al., 2001). However, there were periods of synextensional magmatism between 16.5 - 15.2 Ma (Faulds et al., 2001). During the Miocene, the Lake Mead domain accommodated 20 - 65 km of sinistral shear (Faulds and Henry, 2008). The Lake Mead fault zone experienced active strike-slip faulting between 17 and 10 Ma (Anderson et al., 1972; Weber and Smith, 1987). More recent work has placed this faulting between 13 and 9 Ma (Faulds et al., 2022). The Las Vegas Shear Zone accommodated >60 km of dextral shear within 15 to 6 Ma, experiencing an oroclinal flexure that is marked by a 90° - 100° clockwise rotation (Duebendorfer and Wallin, 1991; Faulds and Henry, 2008). It has been suggested that these strike-slip faults occurred coevally with the extension of the regional detachment faulting (Weber and Smith, 1987).

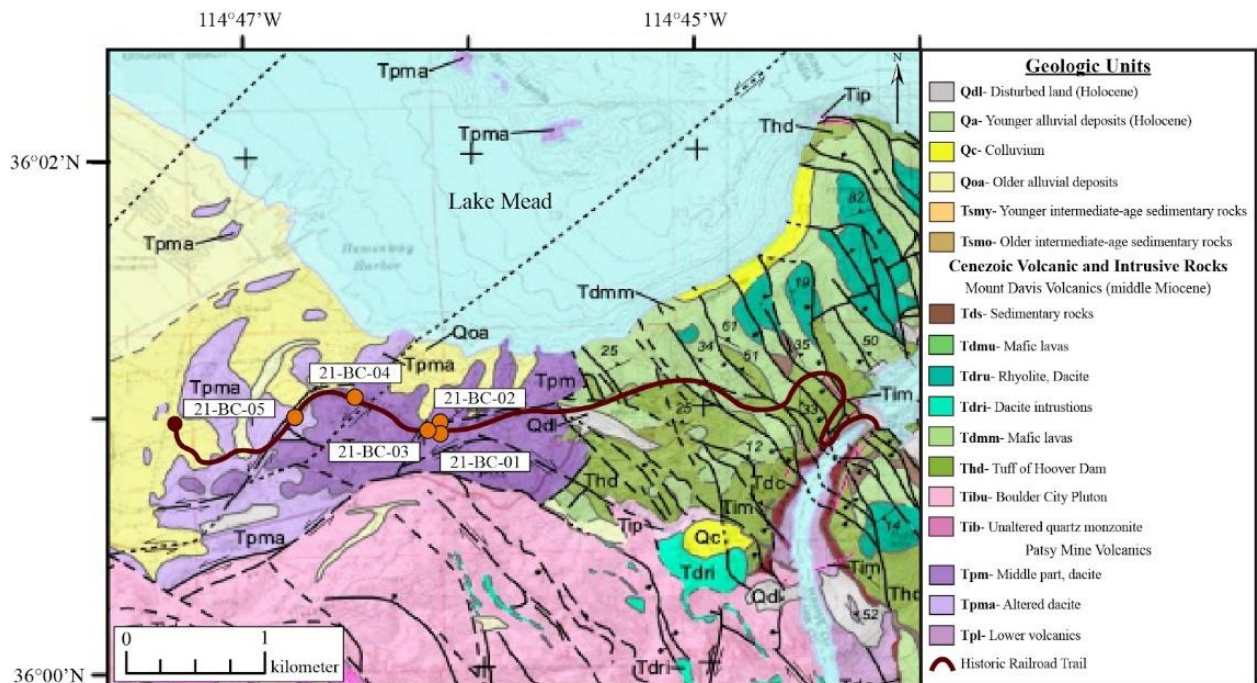


Figure 5. Map of the sample locations and study area in Lake Mead region.

This map includes the notated 5 outcrop sites along the Historic Railroad Trail. Adapted from Beard et al., 2014.

The studied fault scarps are located in the southern Boulder Beach portion of Lake Mead on the border of southern Nevada and northwestern Arizona (Fig. 4). The fault scarps have been exposed through the building of a railroad, including several tunnels whose walls host fault scarps, during the construction of the Hoover Dam in the 1930s and later repurposed into a recreational trail leading to the Hoover Dam. The area is structurally complex consisting of the generally N-W striking right-lateral Las Vegas Valley shear zone, the generally N-E striking left-lateral Lake Mead fault system, the N-S extensional faults of the Northern Colorado River Extensional Corridor (NCREC), the Hamlin Bay fault, and the Saddle Island detachment fault (Fig. 5; Weber & Smith, 1987; Fuerbach et al., 1993; Anderson and Beard, 2010).

The geologic map of the field area is shown in Figure 5 with the sample sites and the Old Historic Railroad trail annotated. The studied fault scarps are in a titled dacite outcrop that is mapped as an equivalent to the middle section of the Patsy Mine Volcanics (Smith, 1984; Beard et al., 2014). The area has been mapped as unit 'Mid-Tertiary Dacite' (Ted) which is described as consisting of "Dark-grey black flows of fine-grained biotite-plagioclase bearing dacite locally interbedded with debris flow breccias and volcanoclastic sedimentary rocks (sometimes containing clasts of plutonic rock)" (Smith, 1984). 'Mid-Tertiary Highly Altered Dacite' (Teda) is a "highly altered dacite, flows of white to red dacite, highly altered and locally mineralized." (Smith, 1984). In the USGS report by Beard et al., (2014) the unit is mapped as 'Tertiary Patsy Mine' (Tpm) which is designated as dacite belonging to the middle section of the Patsy Mine Volcanics.

Sample No.	Rock Type	N. Latitude	W. Longitude	General	Material Dated	Apparent Age (Ma)
36	Basal vitophyre of rhyodacite lava	35°45'00"	114°50'40"	3 mi NNW of Nelson, Nev.	Biotite	15.3 ± 0.6
37	Basal vitophyre of rhyolite lava	35°37'00"	114°52'13"	4.5 mi NW of Nelson, Nev.	Sanidine	16.1 ± 0.6
38	do.	35°37'00"	114°52'13"	do.	Biotite	15.8 ± 0.6
39	Basal vitophyre of rhyolite lava	35°45'15"	114°51'40"	3.8 mi NW of Nelson, Nev.	Sanidine	14.5 ± 0.6
40	do.	35°48'00"	114°51'40"	do.	Biotite	15.5 ± 0.7
41	Basal vitophyre of dacite lava	35°48'00"	114°52'50"	5 mi NW of Nelson, Nev.	Biotite	15.8 ± 0.2
42	do.	35°46'37"	114°52'50"	do.	Hornblende	18.6 ± 0.3
43	Densely welded mildly-altered ash-flow tuff	35°46'37"	114°36'03"	West flank of Black Mts., Ariz.	Hornblende	18.6 ± 0.7
44	do.	35°46'37"	114°36'03"	do.	Rock	22.8 ± 0.9
45	do.	35°46'37"	114°36'03"	do.	Sanidine	27.9 ± 1.1
46	do.	35°46'37"	114°36'03"	do.	Biotite	40.8 ± 1.6

Table 2. K-Ar ages from Lake Mead area.

Patsy Mine Volcanic samples taken from the Eldorado Mountains, south of the Lake Mead area. The highlighted box emphasizes the Patsy Mine Volcanics dacite results from biotite and hornblende. Adapted from Anderson et al., 1972.

The Patsy Mine Volcanics are moderate to highly tilted mafic to felsic lavas consisting mostly of rhyolite lavas with interbedded tuffaceous sedimentary rocks with occurrences of interbedded flow breccias and volcanoclastic sedimentary rocks (Fig. 6; Faulds et al., 2001; Felger et al., 2014). Patsy Mine Volcanics in the Eldorado Mountains have yielded K-Ar ages of 14.5 to

18.6 Ma (Table 2), this range spans the beginning of volcanism in the area and includes the period of synextensional magmatism (Anderson et al., 1972; Faulds et al., 2001).

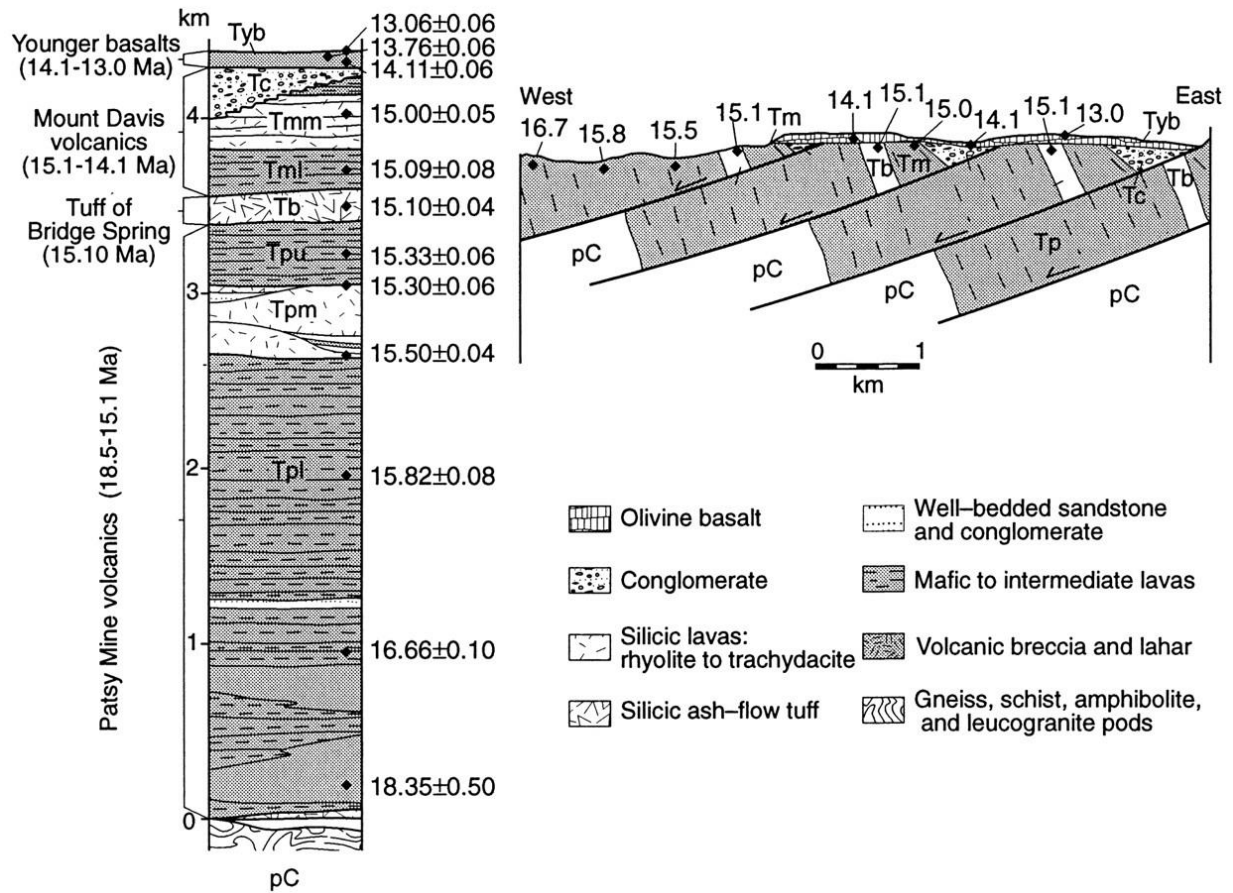


Figure 6. The volcanic column of Patsy Mine Volcanics.

The overlying rock units along with a cross section of the deposition of these units and their ages. From Gans and Bohrsen, 1998.

III. SAMPLES AND METHODOLOGY

III.I. Fieldwork

Detailed field characterization of the faults at the outcrop scale provides geologic context and relationships of the faults to make sense of the spatial and temporal relationships. The field analysis included rock and fault mirror characterization (mineralogy, structural features), measurements of the fault scarp dimensions, measurements of the orientations of the fault planes, documentation and measurements of the occurrence and orientations of slickenlines, and measurements of volcanic bedding orientations of the host rock and surrounding volcanic rock layering. Samples were collected from five separate fault scarp outcrops with fault mirror surfaces along the Old Historic Railroad Trail (Fig. 5) for hand sample characterization, detailed microtextural analysis, and elemental composition evaluation. Samples of the host rock were collected from the 21-BC-03 and 21-BC-05 sample locations for zircon U-Pb and apatite He geo- and thermochronology.

III.II SEM/EDS Methodology

Fault mirror surface samples from each sample were cut into cm x cm rectangles that could fit within a 1" round and mounted in cross section orientation in epoxy within ½" rounds, then carbon coated before being imaged with SEM. Hematite aliquots from the fault mirror layers were isolated from the host rock using manual tools and fine point tweezers. Fault mirrors with the thickest, most visibly pure hematite layers were selected from sample sites 21-BC-03, 21-BC-04, and 21-BC-05. Aliquots ranging from 50-400 μm were placed on carbon tape and stereograph images were taken. The aliquots were imaged using back scatter electron (BSE) and secondary electron (SE) SEM with EDS maps/spot analysis generated from the fault mirror surfaces for elemental distribution.

Microstructural characterization of the fault mirrors was performed specifically targeting the fault mirror surface, fault mirror domains, and contact with the host rock as areas of interest for representative grain morphologies and textures. This characterization was conducted for both plan and cross-section views of the fault mirror surfaces through SE and BSE (Odlum et al., 2021). SEM and EDS analysis were performed on four different instruments. The Hitachi S-4700 II SEM at University of Nevada, Reno's Department of Geological Sciences and Engineering (DGSE) was used to image sample 21-BC-03. The *JEOL JSM 5600 SEM* and *JEOL JSM-6700F FESEM* at University of Nevada, Las Vegas' Electron Microanalysis and Imaging Laboratory (EMiL) was utilized for EDS analysis, images of samples 21-BC-01, 21-BC-02, 21-BC-04, and 21-BC-05. The College of Southern Nevada JOEL-IT200 SEM was used for EDS maps, images of aliquots of 21-BC-03, 21-BC-04, and 21-BC-05.

Initial analysis began with overall images of the epoxy puck at x 35 – x 50 magnification; these images allow for measurement and designation of the fault mirror domain/s, general modal abundances, grain size distribution, and characterizing the nature of the contact of the fault mirror with the host rock. Once sufficient images were obtained to characterize the sample at this scale, textures and grain morphologies within the fault mirror domain were examined at a finer scale of x 250 – x 1,000. The textures, grain morphologies, and nature of the contact between the fault mirror domain and the volcanic host rock were also analyzed at this scale. The fault mirror surface is an area of particular importance for characterization in this study and these areas were examined initially at a similar scale to the fault mirror domain and host rock contact, however, an x 3,000 – x 70,000 magnification was needed to fully capture the micro-nano scale features present at the surface.

Collected SEM images were processed through ImageJ for measurements of the fault mirror domains, average grain sizes of the host rock and hematite in each domain (if applicable). The average grain size measurements were taken at high and low magnifications, close to and far away from the fault surface. Scales were set for each image according to the magnification and individual length x width measurements of 50-150 grains.

III.III. Mineral Separation/Dating Methodology

Host rock samples were collected from two of the outcrops 21-BC-03 and 21-BC-05 and were targeted for dating due to their distance apart and their different measured orientations. Host rock samples were crushed and ground using a Badger Rock Crusher, a Chipmunk Jaw Crusher, and a disk grinder. The resulting material was sieved through a 0.417 mm (0.0164 in) screen. The crushed host rock was separated by density using a gravity separator water table. The heavy materials collected were then sent through a Frantz magnetic separator tilted to 10° and was run at 0.2, 0.5, and 1.0 amps. The collected non-magnetic material was processed further using bromoform for heavy liquid density separation. The desired minerals were handpicked from the heavy separates.

III.IV. Zircon U-Pb Geochronology

The radioactive decay system of U and Th isotopes to Pb isotopes is a geochronological tool that can date the crystallization of zircon (Schoene, 2014). ^{238}U , ^{235}U , and ^{232}Th isotopes produce different Pb isotope daughter products, ^{206}Pb , ^{207}Pb , and ^{208}Pb , through a process of independent alpha and beta decays (Schoene, 2014). U-Pb utilizes two separate thermochronometers, $^{207}\text{Pb}/^{235}\text{U}$ and $^{206}\text{Pb}/^{238}\text{U}$ (Jackson et al., 2004; Bowring and Schmitz, 2003). Zircon has been one of the most used geochronometers in the U-Pb system because of its stability, high closure temperature (exceeding 900 °C), high U and Th content, and low amounts of natural

Pb (Cherniak and Watson, 2001; Wu and Zeng, 2004). Diffusion of radiogenic Pb within zircon requires temperatures typically higher than most magmatic conditions (>1000 °C) so zircon U-Pb ages represent the initial mineralization of the grain (Crowley et al., 2007).

Zircon was hand-picked and mounted on double-sided tape on 2.5 cm diameter acrylic mounts and laser spots were chosen targeting non-broken, inclusion-free grains. Analysis was conducted by laser ablation-inductively coupled plasma-mass spectrometry (LA-ICP-MS) to determine zircon U-Pb ages. Sample mounts were loaded into a TwoVol 1 ablation cell and ablated using an ESL 193 nm NWR193 excimer laser for analysis with a Quadrupole collector ThermoFisher Scientific TM iCAP ICP-MS at the Nevada Plasma Facility Lab at the University of Nevada, Las Vegas. Corrections for depth-dependent elemental and isotopic fractionation were performed using zircon standards FC1 (1099 ± 0.5 Ma; Paces and Miller, 1993), and secondary standards Plesovice (PL-1; 337.2 ± 0.4 Ma; Sláma et al., 2008) and Fish Canyon Tuff zircon (27.65 ± 0.34 Ma; Lanphere & Baadsgaard, 2001) were used to monitor data quality. A primary standard was analyzed for every five unknown analyses and one secondary standard was analyzed for every ten unknown analyses. Zircon analyses were reduced using the VizualAge™ workflow in the Iolite™ plugin for Igor Pro™ (Paton et al., 2010; Paton et al., 2011; Petrus & Kamber, 2012). Zircon U-Pb ages and 2σ errors are reported for analyses with <15% $^{206}\text{Pb}/^{238}\text{U}$ uncertainties, <40% discordance, and < 5% reverse discordance. Reported values for grains < 1200 Ma are $^{206}\text{Pb}/^{238}\text{U}$ ages with $^{206}\text{Pb}/^{238}\text{U}$ vs. $^{207}\text{Pb}/^{235}\text{U}$ discordance, whereas values for grains > 1200 Ma ages are $^{207}\text{Pb}/^{206}\text{Pb}$ ages with < 15% $^{206}\text{Pb}/^{238}\text{U}$ vs. $^{207}\text{Pb}/^{206}\text{Pb}$ discordance.

III.IV. Apatite (U-Th)/He Thermochronometry

The radiogenic decay system of U and Th isotopes, ^{238}U , ^{235}U , and ^{232}Th , to helium, ^4He , and the thermally activated diffusion of He is a well-established low-temperature

thermochronometer (e.g., Zeitler et al., 1987; Lippolt et al., 1994; Wolf et al., 1996; Stockli et al., 2000; Ehlers and Farley, 2003). A particular advantage to the (U-Th)/He system is negligible atmospheric helium concentrations (~5 ppm) indicating that the chances of contamination of He in a closed system are low (Zeitler et al., 1987).

The apatite (U-Th)/He system is sensitive to crustal temperatures of ~40 – 80 °C (Wolf et al., 1996; Stockli et al., 2000). ⁴He begins to accumulate within apatite below temperatures of ~70 – 75 °C, and ⁴He does not accumulate because diffusion is removing, He at the same rate as it is produced by decay above 80 °C (Stockli et al., 2000; Ehlers and Farley, 2003). The experimentally determined He closure temperature for apatite is 62 °C for apatite grains with a diameter of 60 μm that experienced cooling at rate of 10 °C/Ma (Flowers et al., 2009). Due to the low closure temperature, the (U-Th)/He dates represent the last cooling event in the upper ~1 – 3 km of crust assuming a surface temperature of 10 °C ± 5 °C and a geothermal gradient of 25 °C/km (England and Molnar, 1990; Stockli et al., 2000; Ehlers and Farley, 2003). Apatite He is a robust tool to constrain cooling in the upper few km of crust that higher temperature systems are not sensitive enough to record (Ehlers and Farley, 2003).

Apatite grains were selected from volcanic host rock samples within 3 mm of the fault mirror surface. The grains were hand-picked with tweezers under a Leica microscope and chosen based on purity, size, and pristine crystal form, excluding grains with large inclusions, broken ends, or widths less than 50 μm. Selected grains were imaged, rotated 90°, imaged again, and length and width measurements were taken from both images to calculate the effective spherical radius (ESR). Grains were generally characterized by noting cracks, inclusions, or breaks.

Apatite (U-Th)/He analysis was completed at the Arizona Radiogenic Helium Dating Laboratory (ARHDL). Apatite grains were packed individually in 1mm-diameter niobium packets.

The Nb packets were placed into a 43-hole planchette. The packets were heated to ~ 500 °C low glow using a CO₂ laser for a duration of 4 minutes to degas the apatite grains. The extracted ⁴He was collected, combined with a ³He spike at 16K for cryogenic and gettering processes for purification. The combined gases were then brought up to 37K and ⁴He was measured using a quadrupole mass spectrometer for isotope ratio analysis. The packets containing the degassed apatite grains were spiked with a ²³³U - ²²⁹U solution of known concentration, and then dissolved in a hydrochloric solution (e.g., Ault et al., 2015). The final U and Th concentrations were measured in solution mode on a ThermoFischer Element2 mass spectrometer (Zeitler et al., 1987; Farley and Stockli, 2002; Ault, 2020). The apatite He dates were calculated using measured contents of ⁴He, U, and Th (Farley and Flowers, 2012; Ault et al., 2015; Ault, 2020).

IV. RESULTS

IV.I. Fieldwork

The studied fault scarps are cm-m², locally mirrored, and near vertical. Samples of the fault surfaces and host rock were collected directly from the exhumed fault scarps hosting fault mirror surface layers accessed along the trail. The tunnels referred to going forward have been classified from the perspective of the trailhead, e.g., ‘Tunnel 1’ is the first tunnel accessed while traveling NE along the trail at 36°01’00”N, 114°46’31”W.

Outcrop 21-BC-01 is located at 36°00’56”N, 114°46’09”W and consists of a nearly vertical exposed fault scarp that makes up part of the northern wall of Tunnel 3 (Fig. 7A, 7B). The fault scarp is a large (~6 m tall and ~10 m long) smooth surface with one significant fracture down the center in an N-NW to nearly vertical orientation. Fault mirror surfaces are present in 10’s cm² sections, concentrated near the top of the fault scarp. There is a dusty weathering layer over much of the surface. Anthropogenic markings (i.e., carvings into the surface) have destroyed significant portions of the center and bottom areas of the fault scarp. There is one set of slickenlines parallel to the fault plane, indicating strike-slip motion. These slickenlines are 7 – 8 m long across the upper section of the fault scarp. The fault scarp has an average orientation of 74/82 E-NE (Fig. 7C).

The hematite fault mirror volume is quite thin with minor cracks randomly oriented throughout the surface. The host rock is coarse-grained, with sub-angular, fragmental, randomly oriented grains (Fig. 7E). The composition of the rock is predominantly quartz, plagioclase feldspar, and potassium feldspar with minor amounts of biotite and other minerals. The grains are cemented in a fine-grained brown red dacite matrix. The average grain size is ~66 μm, with a range of ~11 μm to ~350 μm.

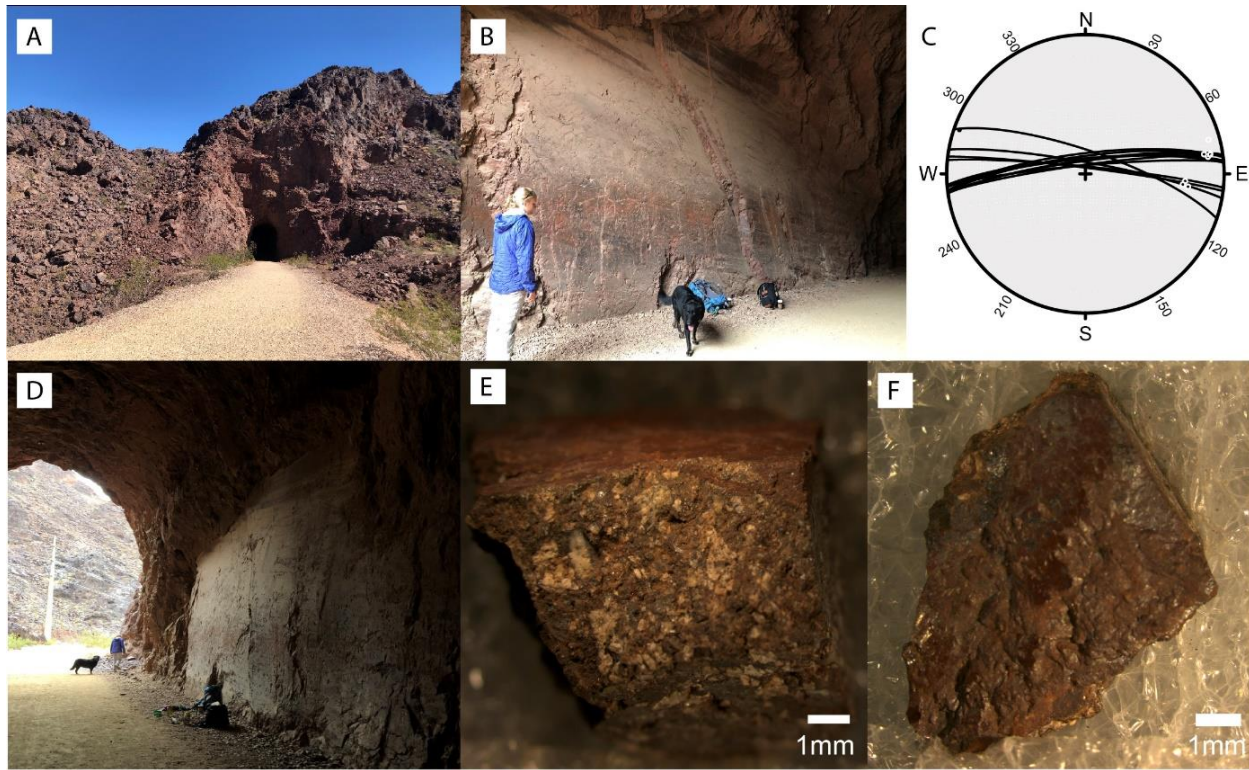


Figure 7. Field figure of 21-BC-01.

A) The outside of Tunnel 3 shows the host volcanic rock. B) The fault scarp inside of Tunnel 3 (view is looking ~NE). C) The corresponding stereonet of the measured fault scarp orientation and slickenlines D) The opposite perspective from B of the fault scarp (view looking ~SW). E) A stereograph image of the cross-sectional view of a sample from 21-BC-01 showing the fault mirror surface at the top of the samples and the underlying host rock. F) A stereograph image of the map view of the fault mirror surface.

Outcrop 21-BC-02 is located at $36^{\circ}00'56''\text{N}$, $114^{\circ}46'08''\text{W}$ and consists of a near vertical exposed fault scarp (~1 m tall, ~0.5 m long) near the ground along the northern wall of Tunnel 3, ~ 6 m west of site 21-BC-01 (Fig. 8B) The fault plane of 21-BC-02 is slightly oblique to the neighboring larger 21-BC-01 fault plane. The surface has a smooth, polished appearance and exhibits one set of slickenlines on the fault mirror surfaces oriented W-NW/E-SE; they are oblique to the fault plane, indicating strike-slip motion (Fig. 8C, 8F). The fault scarps have an average

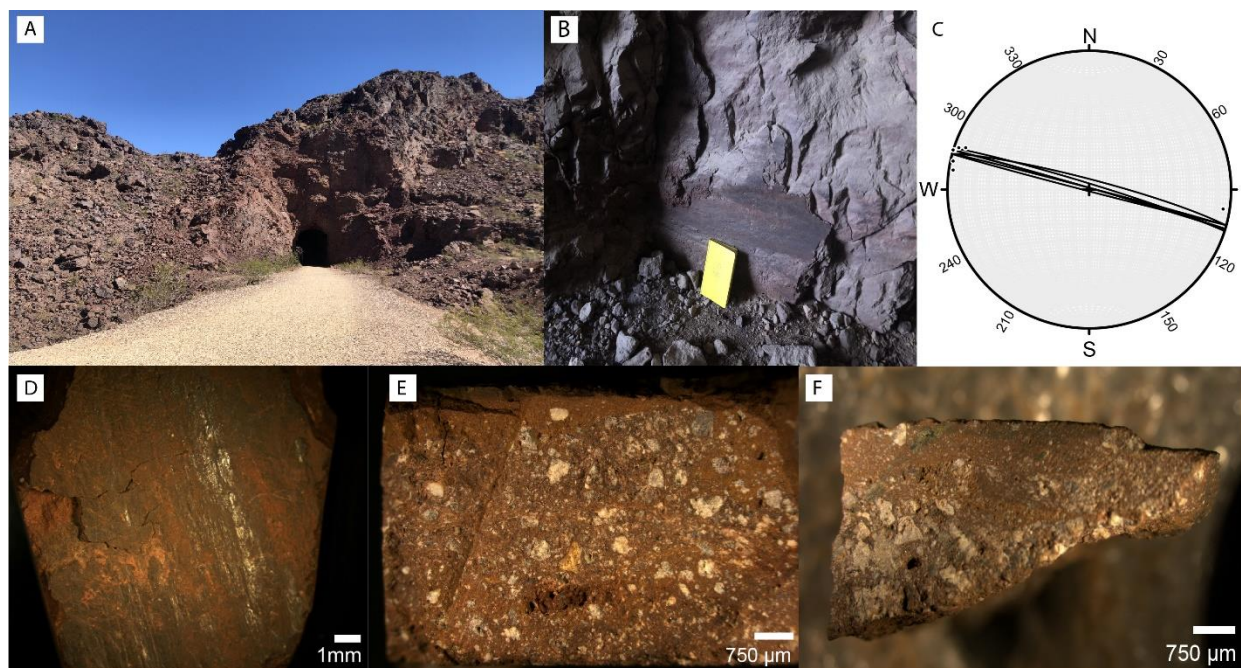


Figure 8. Field figure of 21-BC-02.

A) The outside of Tunnel 3 and the hosting volcanic unit. B) Image showing the fault scarp inside of the tunnel with a *Rite in the Rain* field notebook for scale (178 mm X 120 mm). C) The corresponding stereonet of the measured fault scarp orientation and slickenlines. D) A stereograph image of the map view of the fault mirror surface. Note the localized, highly reflective areas and slickenlines. E) stereograph image of the cross-sectional view of a sample from 21-BC-02 showing the fault mirror surface (top of image) and underlying volcanic host rock. F) A stereograph image of the cross-sectional view of a sample from 21-BC-02 showing the fault mirror surface (top) and the underlying host rock.

orientation of 256/88 E-SE (Fig. 8C). The volcanic host rock is medium grained, with sub-angular, fragmental, randomly oriented grains (Fig. 8D). The composition of the rock is predominantly quartz, plagioclase feldspar, and potassium feldspar with minor amounts of biotite and other accessory minerals. The grains are cemented in a fine-grained brown red dacite matrix. The average grain size is $\sim 150 \mu\text{m}$, with a range of $\sim 12 \mu\text{m}$ to $550 \mu\text{m}$.

Outcrop 21-BC-03 is located at $36^{\circ}00'56''\text{N}$, $114^{\circ}46'09''\text{W}$ and consists of nearly vertical exposed fault scarps that contain several relatively small (10's cm^2) fault mirror surfaces along the

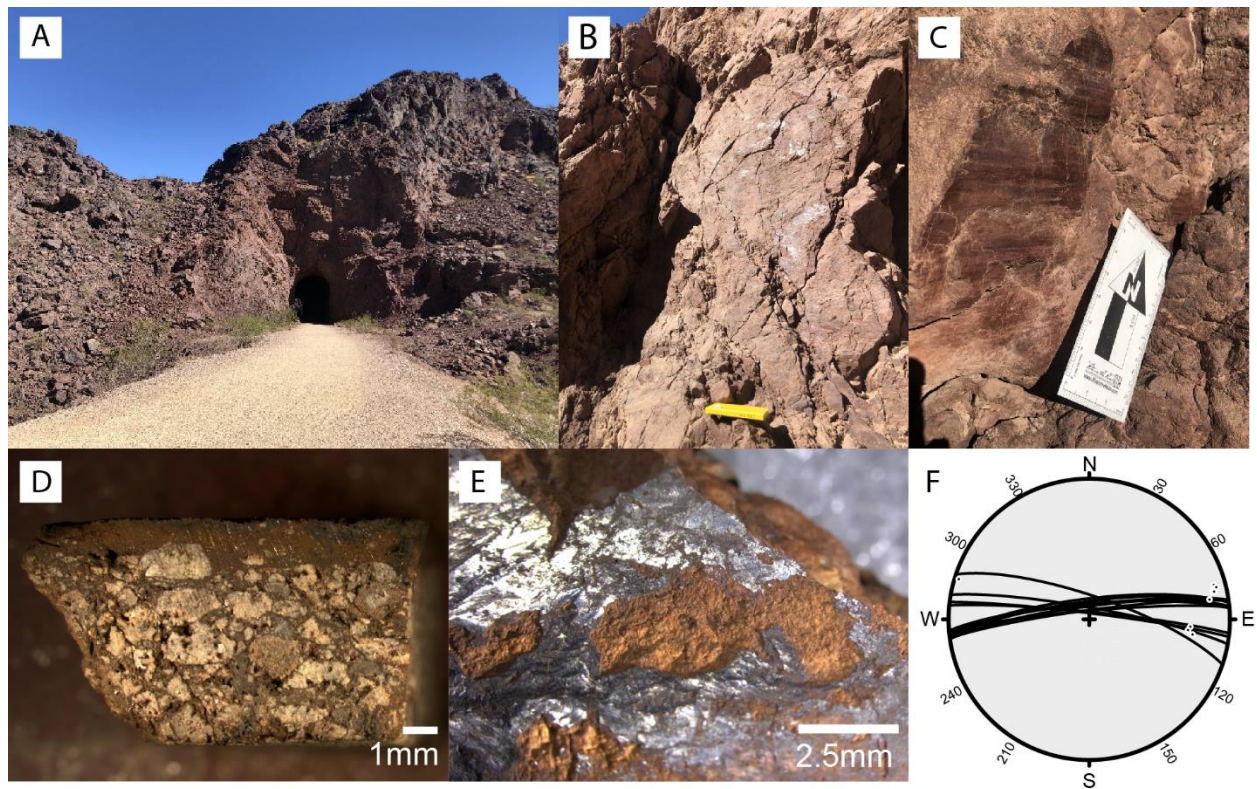


Figure 9. Field figure of 21-BC-03.

A) The outside of Tunnel 3 showing the host volcanic rock. B) Sampled fault scarp outside of the tunnel with a ruler in the rain notebook for scale (178mm X 120mm). C) Mirrored fault surface showing strike-slip slickenlines. D) Stereograph image of the cross-sectional view of a sample from 21-BC-03 showing the fault mirror surface at the top and underlying volcanic host rock. E) A stereograph image of the map view of a sample from 21-BC-03 showing the fault mirror surface and the host rock. F) The corresponding stereonet of the measured fault scarp orientation and slickenlines.

northern side of the trail near the entrance to Tunnel 3 (Fig 9A, 9B, and 9C). The surfaces are locally mirrored. The fault scarp surface contains one set of slickenlines slightly oblique to the fault plane consistent with strike-slip motion. The slickenlines are oriented predominantly E, the lengths range from 15 cm to 60 cm. The fault mirror surfaces are 1-2 m away from a vertical brecciated fault. The fault is N-S trending, ~7 m in height, tapered from ~1 m to just cm wide at the base near the ground. The average orientation of the fault scarps is 269/82 E-W (Fig. 9F).

The host rock of the fault scarp is fine-medium grained, with sub-angular, fragmental, randomly oriented grains (Fig. 9D). The composition of the rock is predominantly quartz, plagioclase feldspar, and potassium feldspar with minor amounts of biotite and other accessory minerals. The grains are cemented in a very fine-grained brown red dacite matrix. The average grain size of the host rock phenocrysts is $\sim 200 \mu\text{m}$, with a range of $26 \mu\text{m}$ to $\sim 1.2 \text{ mm}$.

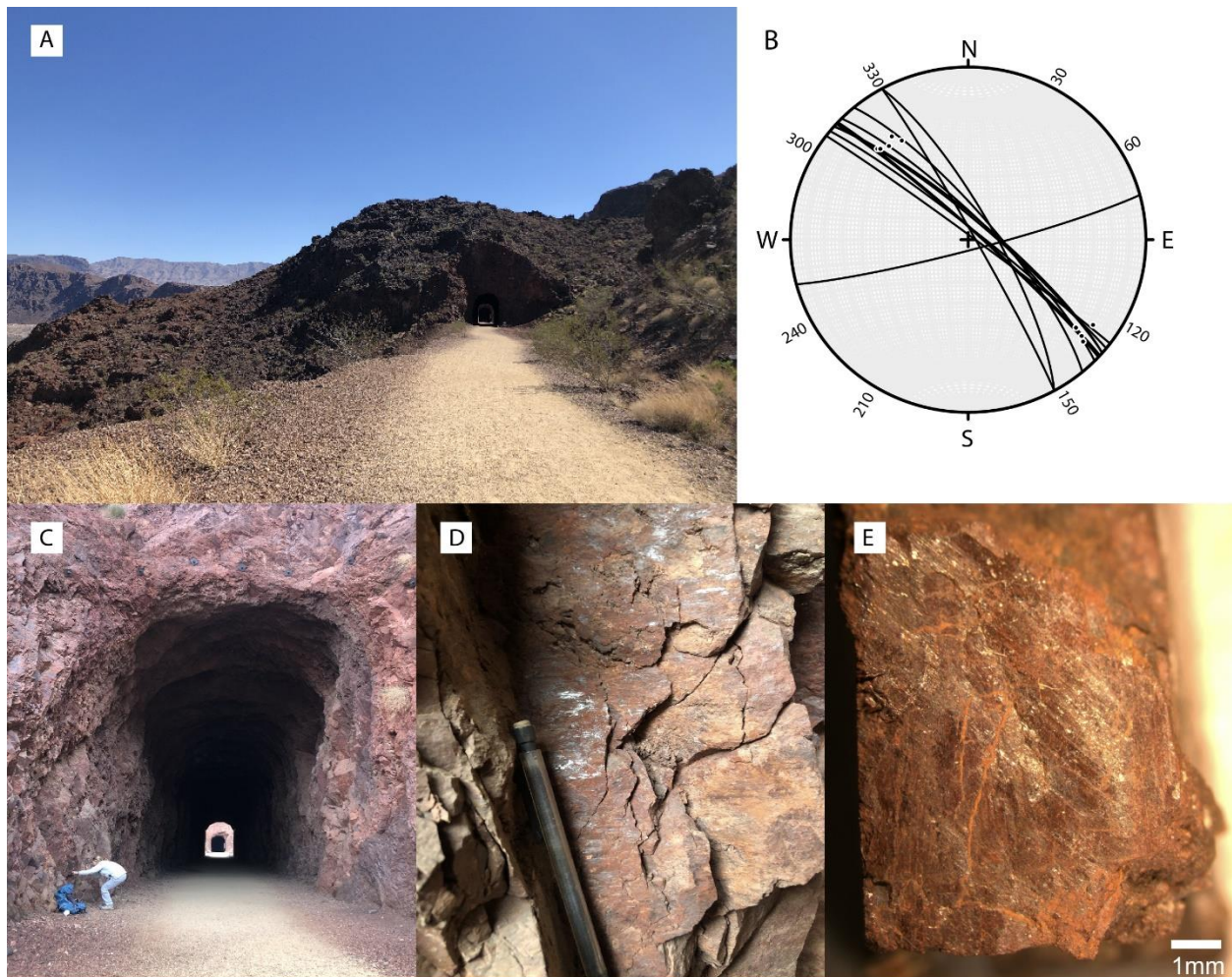


Figure 10. Field figure of 21-BC-04.

A) The outside of Tunnel 1 and the volcanic unit hosting the fault scarps. B) The corresponding stereonet of the measured fault scarp orientation and slickenlines. C) Image showing the location of the fault scarp outside of the tunnel on wall of the entrance. D) An image of one of the fault mirror surface exposures E) map view stereograph image of a sample from 21-BC-04 showing the mirrored fault surface and slickenlines.

Outcrop 21-BC-04 is located at 36°01'03"N, 114°46'32"W and consists of several parallel faults with many sections of exposed fault mirror surfaces on the NE wall of Tunnel 1 (Fig. 9A, 9C). These sections range from a few to 10's cm² (Fig. 9D). There are two main fault mirror surface exposures, each is ~20 cm by 50-55 cm, accompanied by significantly smaller exposures. Some of the surfaces, including one of the main exposures, have experienced anthropogenic vandalism. Many of these fault mirror surfaces have a specular luster and are locally polished. Two visible sets of slickenlines are present in two of the largest exposures with NW and SE orientations (Fig. 12). The slickenlines range from 6 to 41 cm in length across the surface. The obliquely oriented set appears to crosscut the horizontal, strike-slip set. The fault scarps have an average orientation of 297/83 NW-SE (Fig. 9B).

One of the fault mirror samples collected from 21-BC-04 contains two sets of parallel fault mirror surfaces ~2 mm away from each other on either side of the host rock. There are many minor cracks along the fault surface, their presence appears to have aided in the weathering process as some are filled with rust-orange dust. The host rock is fine-medium grained, with sub-angular, fragmental, randomly oriented grains. The composition of the rock is predominantly quartz, plagioclase feldspar, and potassium feldspar with minor amounts of biotite and other minerals. The grains are cemented in a very fine-grained brown red dacite matrix. The average grain size of phenocrysts in the host rock is ~102 μm, with a range of ~16 μm to ~400 μm.

Outcrop 21-BC-05 is located at 36°00'58"N, 114°46'50"W and consists of near vertical fault scarps hosting fault mirror surfaces on the north side of the trail (Fig. 10A). There are two large, exposed fault scarps ~4 to 5 m wide and ~6 to 10 m tall (Fig. 10B). The fault mirror surfaces have varied appearances, some of the fault mirror surface layers are thicker and darker with an iridescent luster; other exposures on the same fault scarp are specular and metallic (Fig. 10D, 10E).

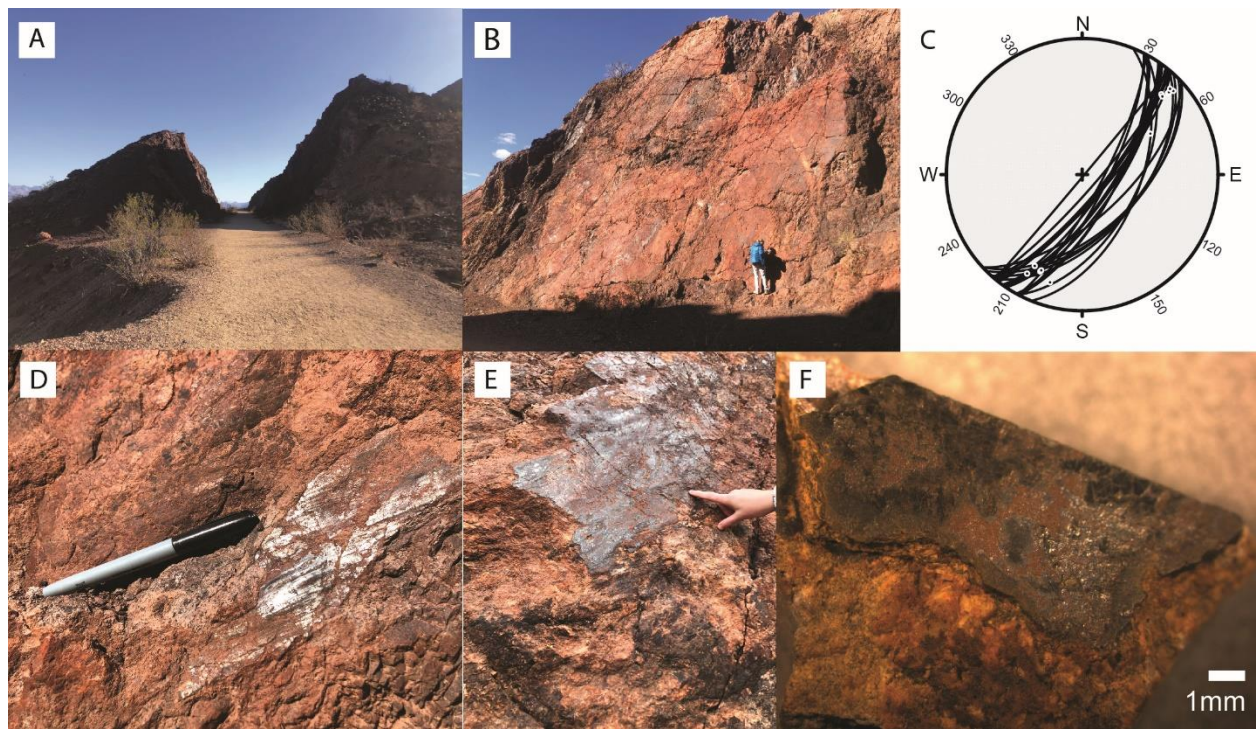


Figure 11. Field figure of 21-BC-05.

A) View looking ~E along the trail. The north side (right side in the photo) is the large, sampled fault scarp B) the large fault scarp outcrop hosting fault mirror surfaces. Note that the entire flat surface in the photo is the hematite coated fault scarp. C) The corresponding stereonet of the measured fault scarp orientation and slickenlines from the N side of the trail. D) A fault mirror surface on the fault scarp that exhibits slickenlines indicating oblique slip. E) mirrored hematite along a portion of fault scarp. F) stereograph image of a hand sample showing the fault mirror surface and the volcanic rock below.

The specular fault mirror surfaces have slickenlines. There are smaller mirrored fault surfaces on the scarps on the opposite, SE, side of the trail (Fig. 10A). The SE fault scarps contain small patches of fault mirror surfaces that range from 1 to 6 cm by 1 to 10 cm (Fig. 10D, 10E). The NW side of the fault scarp hosts the largest and most specular fault mirror surfaces. Many of the fault mirror surfaces have slickenlines ~2 cm to 20 cm. There are two distinct sets of slickenlines, ranging from a few to tens of cm long, orientated NE and S-SE. There is a visible hematite dominant vein, ~55 cm, at the center base of the outcrop. The outcrop, as a whole, is ~10 m tall,

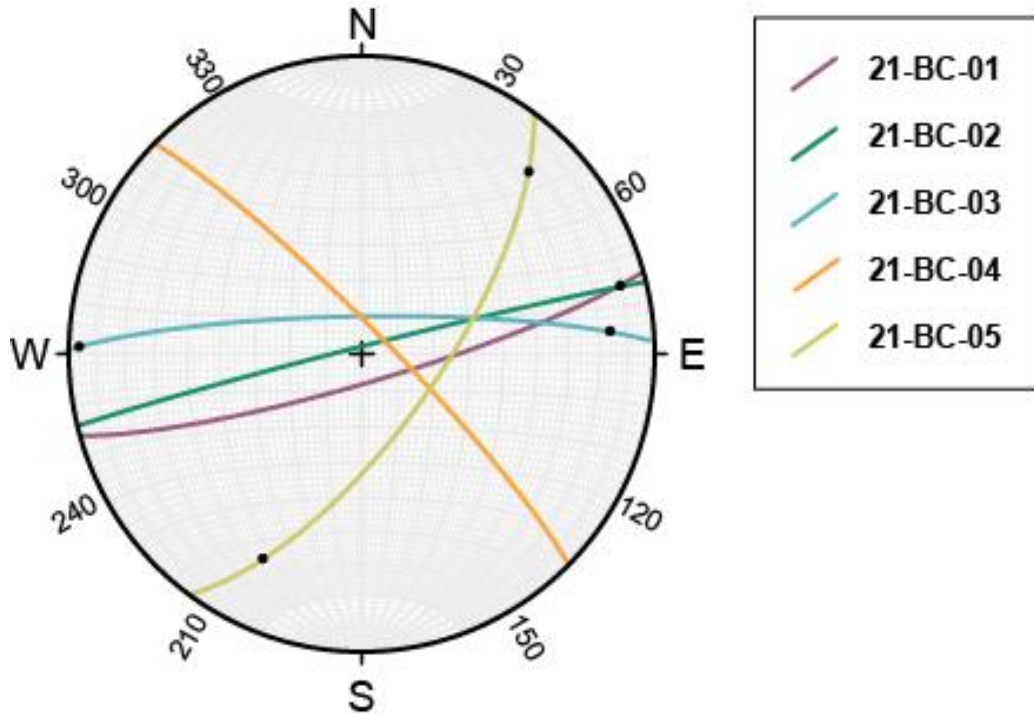


Figure 12. Stereonet of average sample site orientations.

This stereonet is displaying the five sample sites and their slickenline measurements. This figure displays the three general orientations that the outcrop sites exhibit. 21-BC-01 generally trends 74/82 E-NE, 21-BC-02 generally trends 256/88 E-NE, and 21-BC-03 generally trends 269/82 E-W. 21-BC-04 trends 269/82 NE-SW. 21-BC-05 generally trends 36/69 NW-SE.

~20 m long with sloping sides that taper down. The fault scarps have an average strike and dip of 36/69 NE-SW (Fig. 10C). The host rock is fine-medium grained, with sub-angular, fragmental, randomly oriented grains (Fig. 10F). The composition of the rock is predominantly quartz, plagioclase feldspar, and potassium feldspar with minor amounts of biotite and other accessory minerals. The grains are cemented in a fine-grained brown red dacite matrix. The average grain size of the host rock phenocrysts is ~74 μm , with a range of ~23 μm to ~307 μm .

Fieldwork also included measurements of volcanic layering from surrounding locations. The first location of volcanic layering measurements (36°01'74"N, 114°77'58"W) is located between 21-BC-04 and 21-BC-05, this outcrop is generally oriented 205/68 N (Fig. 13A). The

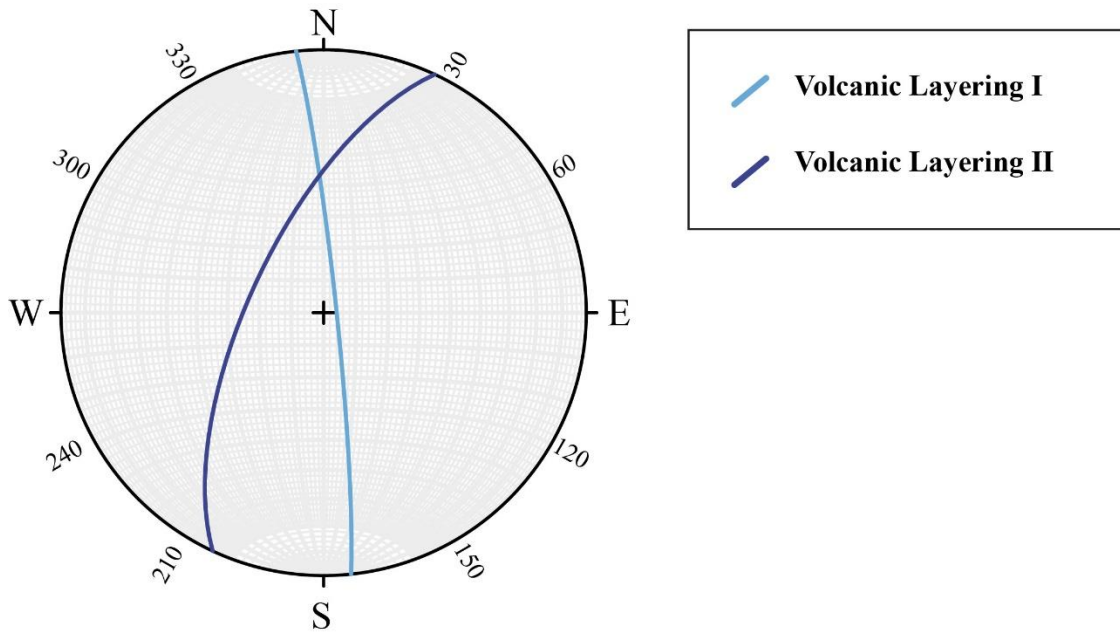


Figure 13. Stereonet of average volcanic bedding orientations.

Stereonet displaying the average orientations of volcanic bedding measured along the Historic Railroad trail. Volcanic Layering 1 is located on the other side of Tunnel 3 from 21-BC-03, the bedding trends 205/68 N-S. Volcanic Layering 2 is located between 21-BC-04 and 21-BC-05, the bedding trends 246/54 NE-SW.

second location ($36^{\circ}00'55''\text{N}$, $114^{\circ}46'10''\text{W}$) of volcanic layering measurements were taken on the southern wall of the Tunnel 3 entrance. The layering is oriented 246/54 W-NW on average (Fig. 13B). Measurements of the fault scarps on the northern wall of Tunnel 3 on the western end (the opposite end of the tunnel entrance from outcrops 21-BC-01, 21-BC-02, and 21-BC-03) were taken at ($36^{\circ}00'57''\text{N}$, $114^{\circ}46'04''\text{W}$). The faults are averagely oriented 280/86 SW-S. Measurements from an outcrop of the tuff of Bridge Spring were taken for comparison to the orientations of the Patsy Mine Volcanics in this study. These measurements included the volcanic layering, faults, and slickenlines. The volcanic layering measured from the tuff is oriented NW

and dipping NE. The faults of the tuff have an average orientation of 246/54 N. The slickenlines are oriented to the W.

IV.II SEM/EDS

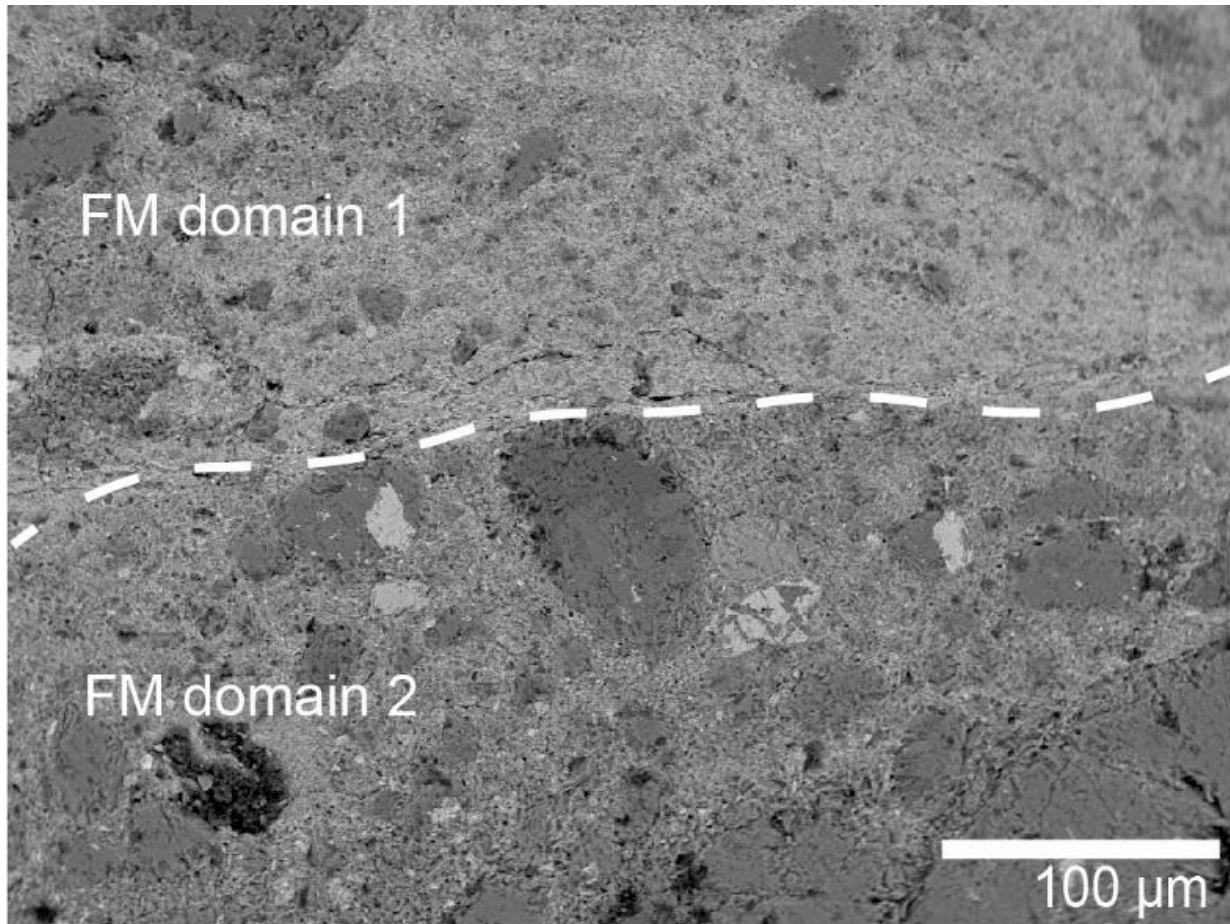


Figure 14. Fault mirror domains of 21-BC-01.

Scanning electron microscope (SEM) back scattered electron (BSE) image of the contact between domain 1 and domain 2 in sample 21-BC-01.

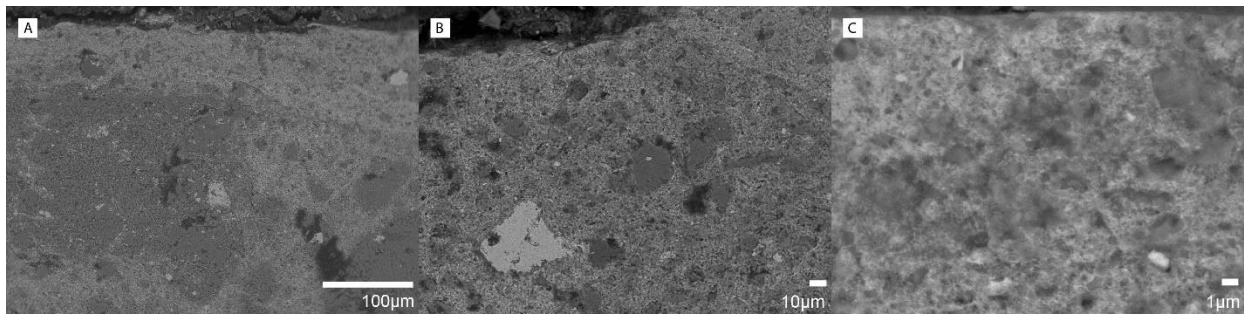


Figure 15. Multi-scale cross-section SEM images of 21-BC-01.

Scanning electron microscope (SEM) back scattered electron (BSE) images of 21-BC-01 in cross-section view. The light grey portions are hematite and the darker grey are volcanic host rock. A) The fault mirror domain at 100 μm scale showing the concentration of hematite and grain size reduction towards the surface. B) The fault mirror volume near the surface at a 10 μm scale showing host rock grain inclusions and the platey morphologies of the hematite matrix. C) The fault mirror surface and underlying volume at the surface at a 1 μm scale showing larger grains and more defined grains near the bottom and the cataclasite texture with nanoparticles of hematite at the slip surface (top of image).

The SEM images of the samples from 21-BC-01 show the fault mirror volume is ~ 1.8 mm thick and made up of two distinct domains of hematite dominated layers between the fault surface and host rock (Fig. 14). The domains have been designated into fault mirror domains, 1 & 2, based upon the relative abundance of hematite and host rock particles of hematite. The first domain is more hematite rich and contains the fault mirror surface. The fault mirror surface is undulatory with a comminuted cataclasite texture mixed with a fine-grained matrix of elongated hematite plates, the elongated axis shows a semi-preferred orientation (Fig. 15B). The average hematite grain size of these plates is 1.8 μm , with a range of 0.7 μm to 4.98 μm . The average grain size for host rock particles within domain 1 is 7.6 μm but the sizes range from 1.1 μm to 41.2 μm . The contact between domain 1 and domain 2 is a sharp change in composition between the hematite rich domain 1 and the mixing of host rock and hematite that makes up the composition of domain 2, seen in Figure 14. The second domain is composed of a similar matrix with significantly larger grains of hematite and host rock inclusions. The matrix of domain 2 is made up of a semi-scaly

fabric with the elongated grains showing a semi-preferred orientation intermixed with bimodally distributed fractured, sub-angular host rock grains. The average hematite grain size for domain 2 is 3.55 μm with a range of 0.88 μm to 22.87 μm . The average host rock grain size is 19.75 μm with a range of 2.49 μm to 90.12 μm . The average hematite grain size for the mixed contact between domain 2 and the host rock is 5.26 μm . The gradational contact between the domain 2 and the volcanic host rock is undulatory, appearing as a mix of both fault mirror volume domain 2 and the host rock. The contact contains tabular and rhombohedral host rock grains that are in contact with a platy hematite matrix. There is a clear pattern of grain size reduction from the host rock to the fault mirror surface through all the domains as seen in the decrease in average grain sizes of both hematite and host rock grains towards the surface (Figs. 14 and 15A).

The SEM images of the fault mirror volume of 21-BC-02 exhibit a mixed composition of host rock and hematite. The fault mirror surface has a cataclasite texture. The average hematite grain size in the upper 100 μm of the fault mirror domain is 4.48 μm , ranging from 1.98 μm to 18.43 μm . Further away from the fault surface the average grain size for hematite is 6.01 μm , ranging from 1.27 μm to 10.76 μm . The average host rock grains in the upper 100 μm of the fault domain is 14.68 μm with a range of 4.03 μm to 75.85 μm . The average host rock grain size in the rest of the fault mirror domain is 29 μm , ranging from 7.1 μm to 97.91 μm . Sections of the host rock, below the fault mirror domain, have large cracks and deformed grain boundaries that have been interstitially filled with unbroken hematite plates and needles (Fig. 16C). There is a clear grain size reduction pattern occurring in both the hematite and host rock from the contact with the host rock to the fault mirror surface. EDS analysis of sections of the fault mirror domain shows the composition to be dominantly Fe and O with some minor traces of Ti and Mn. The spot size

EDS analysis of the host rock indicated that the composition is made up mostly of K, Al, Si, O with minor amounts of P, Ca, C, Na, and Zr detected (Fig. A3).

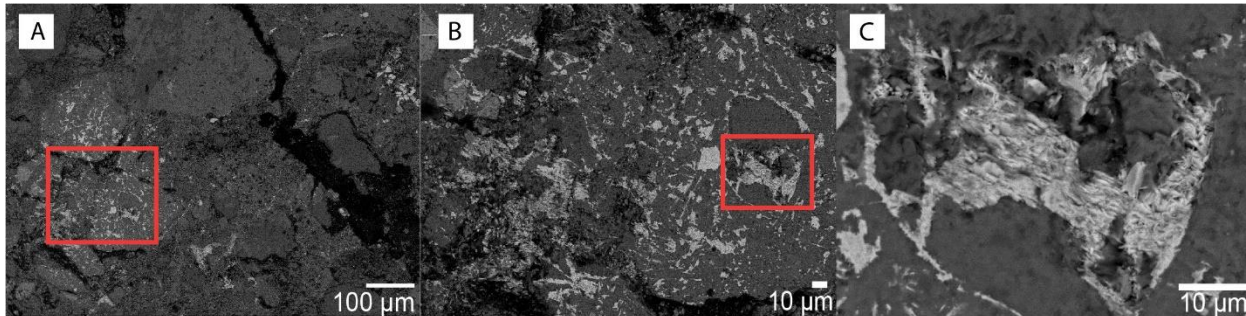


Figure 16. Multi-scale cross-section SEM images of 21-BC-02.

A) Representative BSE image of the fault mirror volume at 200 μm scale showing mixing between hematite and the host rock. B) Image the host rock at a 100 μm scale, the image shows hematite inclusions in the host rock and large fractures. C) image of hematite clusters in B. D) image of fractures in the host rock that have been filled with hematite plates.

The SEM images of the fault surface of samples from 21-BC-03 show the fault mirror volume thickness is undulatory, ranging from 1.72 mm to 2.03 mm, with an average thickness of 1.84 mm. The fault surface has a cataclasite texture made up of nano-particle hematite grains with small sections of scaly fabric where the elongated plates exhibit semi-preferred orientations (Fig. A5). The average hematite grain size on the fault mirror surface is 0.26 μm , with a range of 0.048 μm to 0.84 μm . Aliquots of 21-BC-03 show a relatively smooth fault mirror surface interrupted by long slickenlines across the whole surface, >200 μm in length (Fig.20). There is a range of fractures throughout the surface and fault mirror volume, some are fine and shallow while others are deep, large fractures. Crevices and craters have been interstitially filled with a mix of large rhombohedral host rock grains and hematite plates. The contact between the fault mirror volume and the host

rock is gradational (Fig. A5). The average hematite grain size at the contact is 0.43 μm , with a range of 0.09 μm to 1.39 μm . The tabular host rock grains on the other side of the contact range from 0.49 μm to 4.83 μm , with an average of 1.45 μm . There is a clear pattern of grain size reduction for both hematite and host rock (Fig. A5). EDS maps of the fault mirror domain show Fe, O, and Mn making up most of the composition with K, Al, and Si notably present, mixed with the FeO and MnO (Fig. A1).

SEM images of the fault mirror volume in sample 21-BC-04 display two distinct domains. In cross-section images the fault mirror volume varies in thickness from 200 μm to 1 mm. Domain 1, that includes the fault surface, is composed dominantly of hematite with sub-angular, randomly oriented host rock inclusions. The host rock inclusions make up ~65% of the composition near the contact with the host rock, away from the fault surface. In the upper ~30 μm of the fault mirror volume that contains the surface the percentage of the host rock in the composition decreases to ~25 – 30%. The fault surface is made up of comminuted grains with a cataclastic texture. The comminuted hematite grains on the surface are 0.58 μm on average. The plate fragments in the scaly fabric range from 60 nm to 0.86 μm with an average grain size of 0.32 μm . These two hematite dominant textures and morphologies are substantially mixed with host rock grains that range from 99 nm to 3.24 μm with an average size of 0.51 μm . Domain 2 is a mix of larger host rock grains within a hematite platey matrix. Within the host rock beneath the FM domain cracks have been interstitially filled with hematite plates, needles, and on a few occasions, clustered spheres composed of randomly oriented hematite plates. There is a visible grain size reduction pattern from the contact with the underlying host rock toward and including the fault surface. The contact between the second domain and host rock is uneven with hematite plates being mixed with rhombohedral/tabular host rock grains in irregular patterns. EDS results of the fault surface show

the composition of the fault mirror volume to be Fe and O, with trace amounts of Mn. The host rock EDS results show K, Al, and Si, with minor amounts of Na (Fig A3).

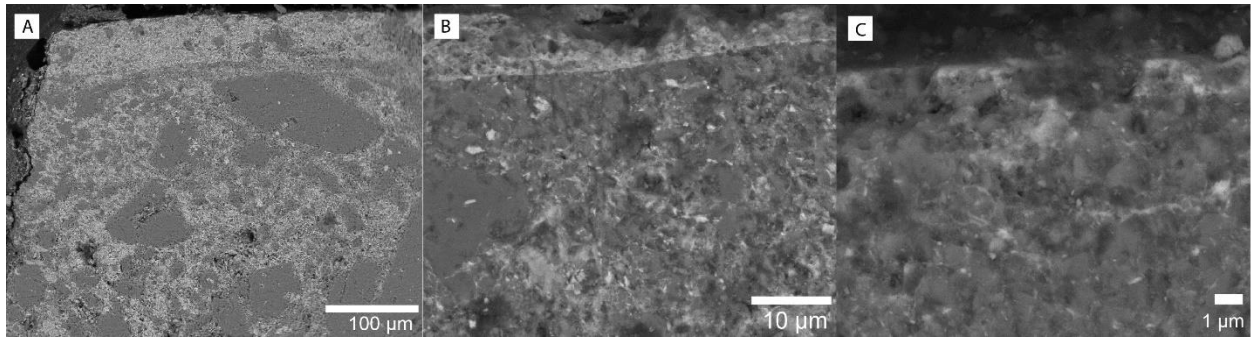


Figure 17. Multi-scale cross-section SEM images of 21-BC-04.

A BSE image of the fault mirror volume of 21-BC-04 showing the two domains at 100 μm scale. The first domain at the surface with a greater concentration of hematite and smaller host rock inclusions. The composition of the second domain is a mix of hematite and the host rock. The second domain has much larger host rock inclusions. B) An image of the contact between the domains at a 10 μm scale. This shows the mixing of hematite and host rock with a clean contact between the first and second domain. C) An image of the domain one near the fault mirror surface at a 1 μm scale. This image shows the nano-particle comminuted grains near the surface.

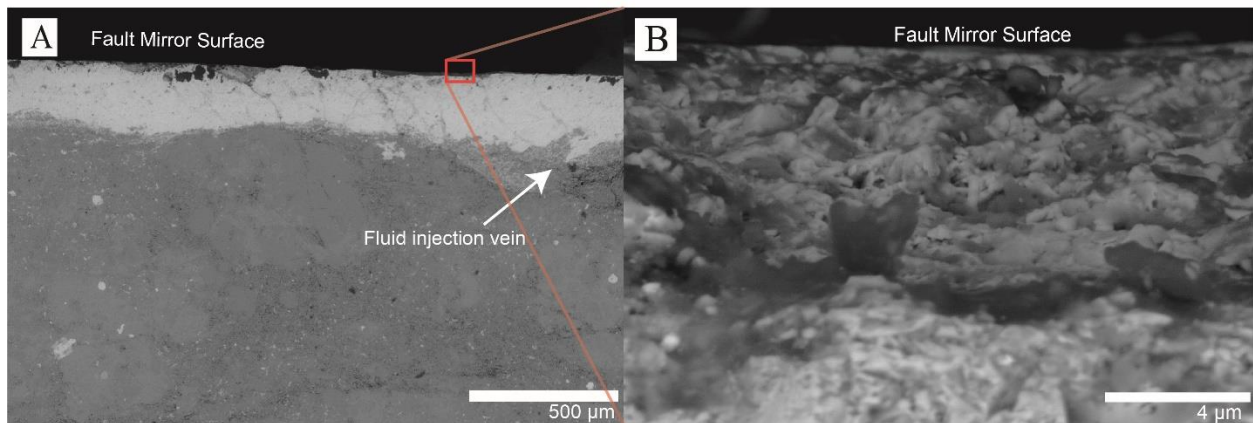


Figure 18. Multi-scale cross-section SEM images of 21-BC-05.

A) Image illustrates the fluid injection evidence from the fault mirror volume into the host rock beneath. B) Fault mirror surface showing nano-particle hematite plate fragments interpreted as comminuted grains with blobs of Si and C.

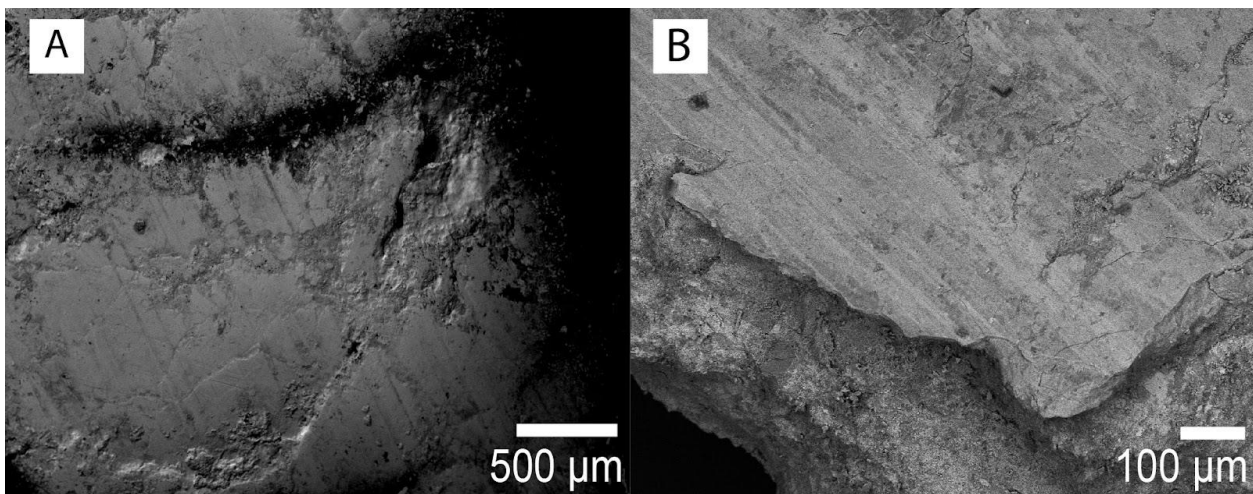


Figure 19. SEM images of slickenlines on fault mirror surface.

BSE SEM images of the fault mirror surfaces in plan view from samples 21-BC-03 and 21-BC-05 showing the smooth slip surfaces with slickenlines.

SEM images of samples collected from outcrop 21-BC-05 exhibit variations in the hematite concentration within the fault mirror volume. The fault mirror volume ranges in thickness from

98.7 μm to 280 μm . The fault mirror surface appears relatively smooth at a 500 μm scale, but under greater magnification the surface is undulatory. The contact between the FM volume and the underlying host rock is sharp with hematite stringers flowing into the host rock and evidence of a fluid injection. The upper 30 μm of the fault mirror volume, including the fault surface, is made up predominantly of randomly oriented hematite plates with varying degrees of damage. The hematite plates and plate fragments range from 1 nm to 10 μm and are randomly oriented.

Cataclasite textures are interbedded with fragments of host rock grains ranging from \sim 5 μm to 10 μm . The contact between the fault mirror volume and underlying host rock has veins of FeO that have morphologies of fluid injection veins. There is a clear grain size reduction pattern within the fault mirror domain from the contact with the host rock to the fault surface. In map view, the fault mirror surface is smooth with visible slickenlines. There are hematite grain inclusions in the host rock just below the fault mirror volume, some of which appear broken and fragmented. Map view images of 21-BC-05 show a set of slickenlines traversing most of the fault surface, seen in Figure 20. EDS map analysis of 21-BC-05 indicates the fault surface composition is composed primarily of Fe, O, and Mn mixed with K, Al, and Si. There is a small but notable Ca signature as well.

The volcanic host rocks are composed of potassium feldspar and quartz with minor occurrences of plagioclase feldspar. This is supported through EDS analysis and tabular host rock grain morphologies, characteristic of feldspars. The EDS examinations of the fault mirror volumes show that they are composed dominantly of FeO, most of which display grain morphologies and textures corresponding to hematite (Guo et al., 2013; Ault et al., 2019; Ault, 2020). Hematite plates are the most common hematite grain morphology. However, there are a few instances of FeO needles that are consistent with the common morphology of goethite (Guo et al., 2013). Other

elements present at the surface are carbon, silica, and manganese oxide. Carbon was detected on the surface of aliquots that were not carbon coated. Without further instrumentation analysis on the surface, these elemental surface contributions cannot be interpreted.

IV.III. U-Pb Zircon Dating

We present 43 new U-Pb ages from samples 21-BC-03 (n=13) and 21-BC-05 (n=30). The data is summarized in Table 3, with Miocene ages highlighted. The single grain U-Pb zircon ages from 21-BC-03 range from 13.4 ± 0.4 Ma to 1381.5 ± 25.4 Ma (2σ standard error). The single grain U-Pb zircon ages from 21-BC-05 range from 12.2 ± 0.4 to 2090.2 ± 23.4 with (2σ standard error). Both samples have ages that are Miocene. The Miocene ages in 21-BC-03 range from 13.4 ± 0.4 Ma to 14.5 ± 0.5 Ma (2σ standard error). The Miocene ages in 21-BC-05 are 12.2 ± 0.4 Ma to 14.9 ± 0.4 Ma (2σ standard error). There are three older zircons ages from 21-BC-03 ranging from 17.5 ± 0.9 Ma to 1381.5 ± 25.4 Ma (2σ standard error). There are 20 older zircon ages from 21-BC-05 ranging from 267.5 ± 2.5 Ma to 2090.2 ± 23.4 Ma (2σ standard error). Concordia plots for the Miocene grains in 21-BC-03 yield a calculated age of 13.86 ± 0.27 Ma (2σ standard error) (Fig. 21). Concordia plots for the Miocene age grains in 21-BC-05 yielded a calculated age of 12.90 ± 0.31 Ma (2σ standard error) (Fig. 21).

Table 3. U-Pb Zircon Sample 21-BC-03 (36.0166373 N, 114.767977 W)				
Sample name	U (ppm)	Age (Ma)	2σ error	Discordance %
BC-03_1	132.69949	13.4	0.4	27.0
BC-03_3	75.772389	14.4	0.6	16.9
BC-03_6	193.41058	13.8	0.5	12.6
BC-03_8	141.42014	13.6	0.5	16.4
BC-03_11	54.321431	364.6	50.9	29.6
BC-03_12	211.60605	14.5	0.5	8.6
BC-03_16	101.53738	13.5	0.5	37.8
BC-03_20	120.86406	17.5	0.9	75.8
BC-03_28	142.52789	14.3	0.5	28.7
BC-03_29	263.16472	13.7	0.4	17.4
BC-03_37	118.51422	14.2	0.4	0.9
BC-03_42	89.077813	1381.5	25.4	0.3
BC-03_43	315.30129	13.8	0.4	17.9
BC-03_45	113.14439	14.1	0.5	2.6

Table 3. U-Pb Zircon analysis results for 21-BC-03.

Results for zircon U-Pb analysis from 21-BC-03 includes Uranium concentration (ppm), U-Pb age (Ma), 2 σ standard error, and % of discordance. The Miocene aged grains in each sample are highlighted.

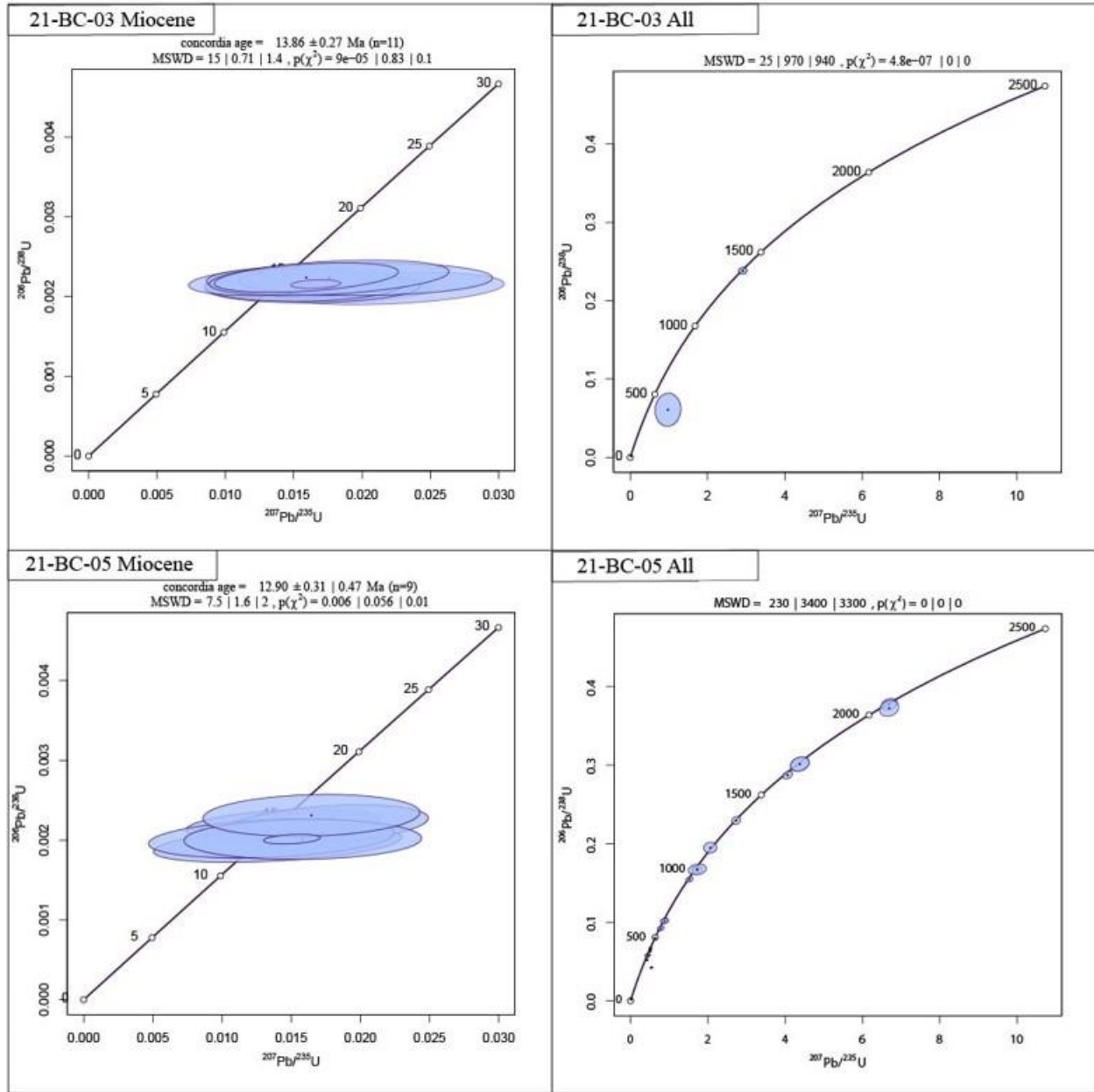


Figure 20. Wetherill Concordia plots of zircon U-Pb ages from the volcanic host rock.

A) 21-BC-03 Miocene ages. B) 21-BC-03 all ages. C) 21-BC-05 Miocene ages. D) 21-BC-05 all ages. The calculated age for 21-BC-03 is 13.86 ± 0.27 Ma (2σ standard error). The calculated age for 21-BC-05 is 12.90 ± 0.31 Ma (2σ standard error). Plots were made using IsoPlotR (Vermeesch, 2018).

IV.IV. (U-Th)/He Apatite dating

We report new dates from 8 apatite grains belonging to outcrops 21-BC-03 and 21-BC-05. The (U-Th)/He apatite dates are summarized in Table 4. The dates from 21-BC-03 (n =7) range from 5.64 ± 0.46 to 12.4 ± 0.36 Ma (2σ standard error). The date from 21-BC-05 (n=1) is 4.78 ± 0.16 Ma (2σ standard error). The dates are bimodal with two groups of 4 – 7 Ma and 10 – 12.5 Ma (Fig. 21A). There is no clear trend between apatite date and effective U (eU) or apatite date and equivalent spherical radius (ESR) (Fig. 21).

Table 5. (U-Th)/He apatite Sample 21-BC-03 (36.0166373 N, -114.767977W)			
Sample name	Dates (Ma)	eU (ppm)	Grain size (ESR)
21-BC-03_Ap2	12.4 ± 0.36	36.01	43.06
21-BC-03_Ap3	11.51 ± 0.52	25.99	35.01
21-BC-03_Ap4	5.64 ± 0.46	18.19	37.19
21-BC-03_Ap5	7.64 ± 0.22	120.05	43.29
21-BC-03_Ap6	7.63 ± 0.44	27.05	41.36
21-BC-03_Ap7	10.61 ± 0.32	14.72	64.62
21-BC-03_Ap8	7.24 ± 0.28	36.86	39.05
Sample 21-BC-05 (36.0161722 N, -114.780514 W)			
21-BC-05_Ap2	4.78 ± 0.16	15.61	66.87

Table 4. (U-Th)/He Apatite analysis results.

Results from Apatite (U-Th)/He analysis of the host rock of 21-BC-03 and 21-BC-05 presented with aliquot numbers, location in latitude and longitude, corrected dates in Ma (2σ standard error), the concentration of U (ppm), and the Equivalent Spherical Radium (ESR) of each grain.

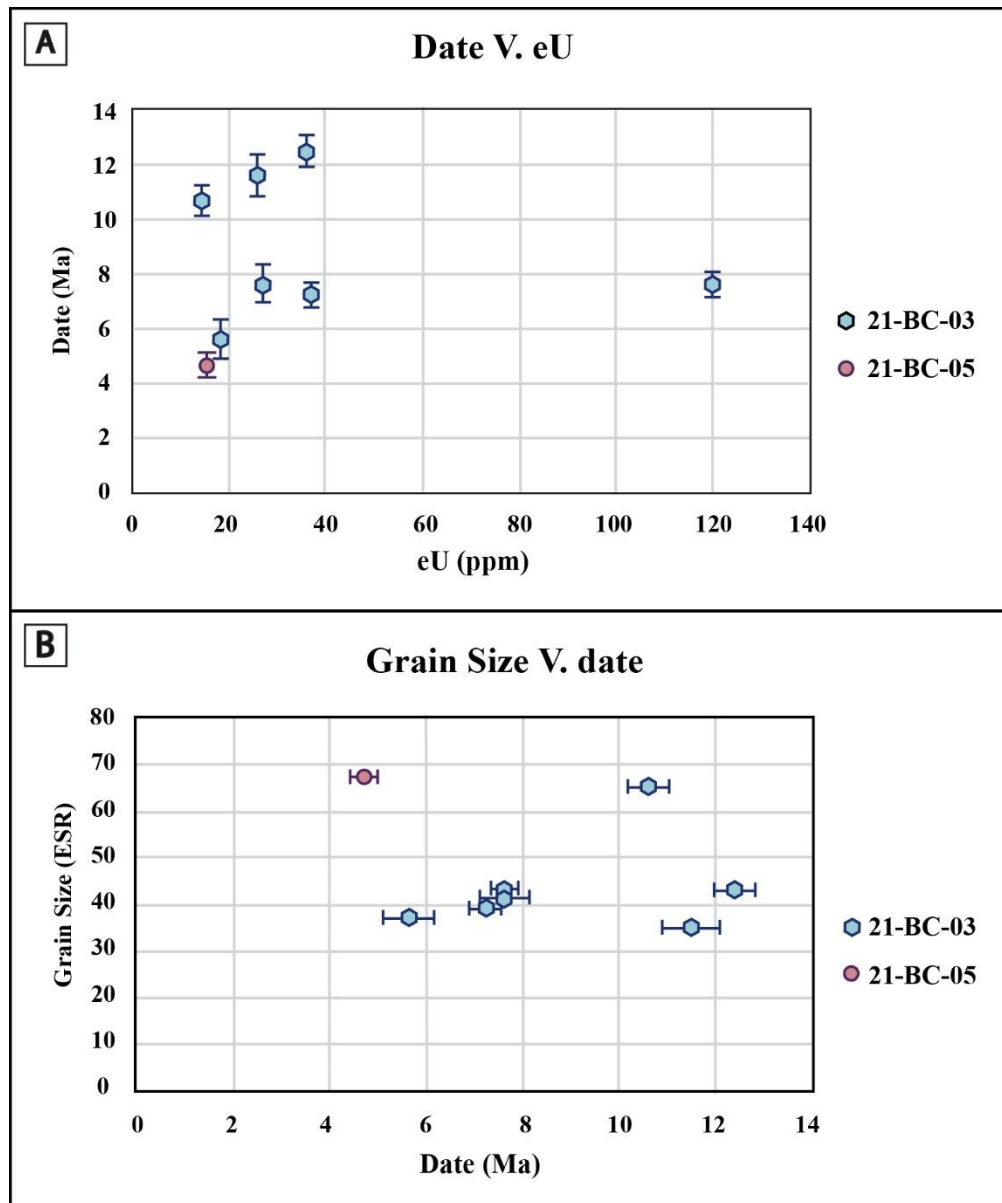


Figure 21. (U-Th)/He Apatite results plots.

A) Dates (Ma) with 2σ standard error bars plotted against the effective U (eU; $eU = [U] + 0.235[Th]$) The plot shows two groups of dates, one between 4.5 – 8 Ma and one between 10.5 – 12.8 Ma. There is one outlying apatite grain from 21-BC-03 that has a concentration of U $\sim 3x$ the amount of the other samples. B) ESR plotted against the date (Ma). There is no clear trend between date and ESR observed.

IV.V. Thermal History Modeling

Apatite He dates were input into an inverse thermal history model using the program HeFTy v. 1.9.1 (Ketcham, 2005). The grains were selected as model inputs due to the partial resetting they exhibit in the range of ~6 – 11 Ma in an attempt to capture the thermal history that could have reset/partially reset the apatite grains. The model simulated 10,000 paths and returned 0 good and 32 acceptable (good of fit using a K-S test defined as $p > 0.5$ for good and 0.05 for acceptable) potential time-Temperature paths for the thermal history that are consistent with the geologic constraints and dates used as inputs. The U-Pb ages from the zircon analysis were used as the parameter of initial mineralization. The surface constraint box at ~15 – 12 Ma is based on geologic context interpretations that the volcanics erupted at the surface. The constraint box between 11.5 – 0 Ma and 0 – 475 °C allows for reheating of the samples during inverse modeling. Inverse model “acceptable paths” all exhibit similar characteristics of initial mineralization between 14 – 12 Ma, rapid cooling to the surface as the volcanics were erupted, gradual reheating (up to ~65 °C), followed by cooling back to the surface temperature range between 4 and 0 Ma.

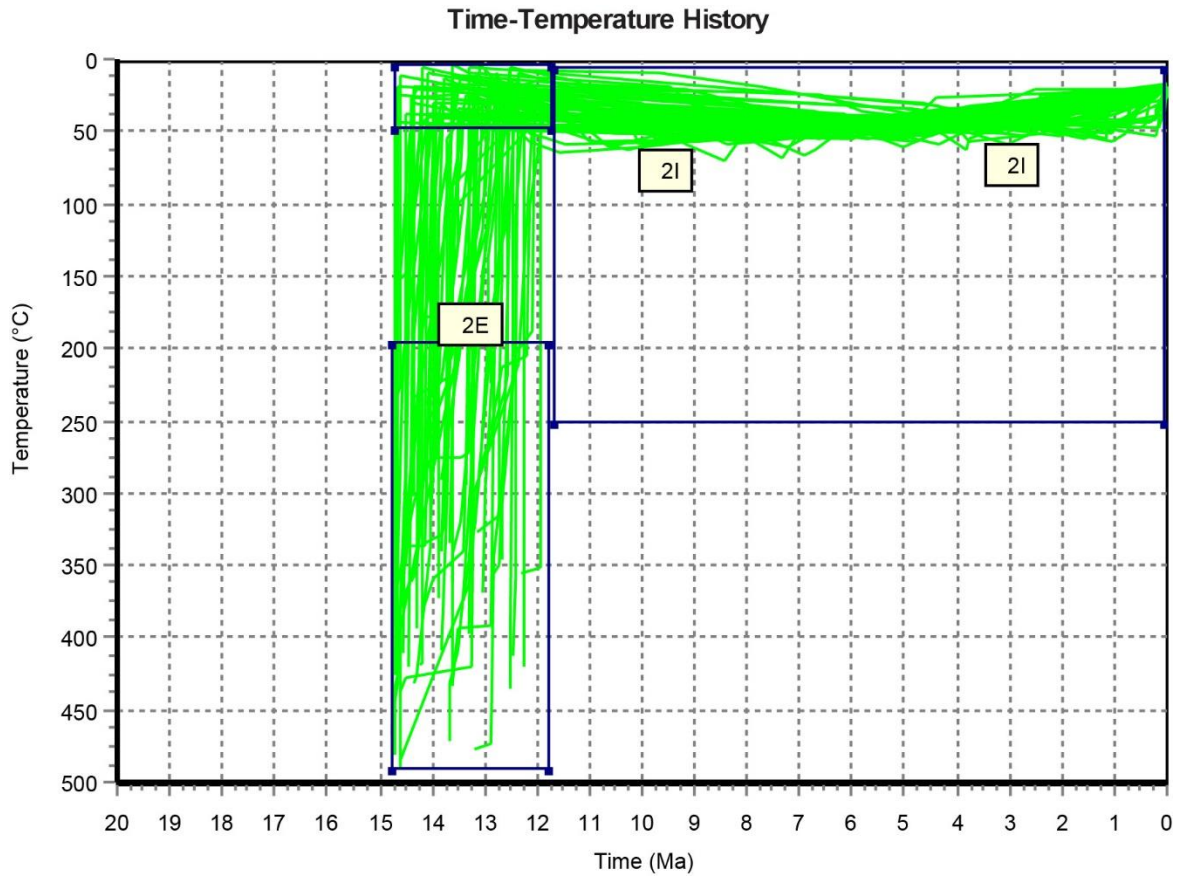


Figure 22. HeFTy inverse model results.

The model displays “acceptable” fits time-Temperature paths of the apatite from the volcanic host rock at site 21-BC-03 (U-Th)/He apatite dates from grains 4, 6, 7 and 8 and the diffusion kinetics for apatite RDAAM (Flowers, 2009). The inverse model paths show eruption between 14.5 – 12 Ma, minor reheating between ~11 and 5 Ma to a max T of ~65 °C, followed by cooling that begins between 4 and 2 Ma.

V. DISCUSSION

V.I. Geologic History

The zircon U-Pb ages date the Miocene volcanics, but have a clear component of older, inherited xenocrysts. Sample 21-BC-03 has a calculated age of 13.86 ± 0.27 Ma and 21-BC-05 has a calculated age of 12.9 ± 0.31 Ma. Both samples are late Miocene and younger than the published Patsy Mine Volcanics dates of 14.5 – 18.6 Ma from the south in the El Dorado Mountains (Anderson et al., 1972), but are consistent the Boulder City Pluton ages of ~13.5 to ~14.5 Ma (Anderson et al., 1972; Gans and Bohrsen, 1998; Faulds et al., 2001; Hinz et al., 2018). The proximity to the Boulder City Pluton and ages support that the studied volcanics are the volcanics associated with the Boulder City Pluton magmatism (Fig. 6). The xenocrystic zircons included in both samples imply that the volcanism plucked older zircon grains from the country rock below the volcanics. There are a significant number of zircons that are discordant which is interpreted to be due to Pb loss, likely from hydrothermal fluid alteration post-eruption.

The apatite (U-Th)/He dates from 21-BC-03 and 21-BC-05 are ~ 6 – 12 Ma. These dates both overlap within error and are younger than the zircon U-Pb ages from the same samples. There is a high dispersion of dates spanning ~6 Ma. The oldest dates are within error or slightly younger than the zircon U-Pb ages, while the youngest apatite He dates are several million years younger than the zircon U-Pb ages. Both the spread of dates and the similarities of the upper range with the U-Pb zircon ages indicate partial resetting of the apatite He system. In order to partially reset the apatite He system, the rocks had to have been reheated to the range of 40 °C to 80 °C (Wolf et al., 1996; Stockli et al., 2000; Elhers and Farley, 2003). If the temperature conditions remained below 40 °C, the apatite He dates and zircon U-Pb ages would overlap within error and represent the original mineralization and eruption age. If the rocks were reheated to temperatures > 80 °C for a

prolonged period, the apatite would have been fully reset and the apatite He dates would reflect the timing of cooling below the closure temperature. The maximum reheating temperature of these rocks reached based on the inverse thermal history model is ~ 63 °C. Assuming a surface temperature of 10 °C \pm 5 °C and a geothermal gradient of 25 °C/km which is consistent with extensional settings with high geothermal gradients, the rocks could not have been buried > 2 km (England and Molnar, 1990; Stockli et al., 2000; Ehlers and Farley, 2003). Episodic volcanism in the Lake Mead area from $\sim 18.5 - 8$ Ma could have buried these volcanics very shallowly, < 2 km (Anderson et al., 1972; Faulds et al., 2001; Beard et al., 2014). A geothermal gradient of 25 °C/km is a minimum estimate as the geothermal gradient is higher in other parts of the Basin and Range today at > 30 °C/km (Natheson and Guffanti, 1987; Kron and Grant, 1980) and was likely higher in the Miocene during extension and magmatism (Eaton, 1987). Therefore, it is possible that the high heat flow of the tectonic setting was the reheating mechanism, and the volcanic units were only minimally buried or not buried post-eruption. Collectively, partial resetting of the apatite (U-Th)/He system and the inverse thermal history models are evidence that the rocks erupted to the surface and stayed within the upper < 2 km of the crust for their entire history. Thus, the studied faults record faulting and mineralization processes that occurred over the last ~ 14 Ma in the shallow crust.

V.II. Faulting history

The orientations measured from the studied fault are interpreted to indicate the faults may belong to three significant fault zone systems in the area. These include the regional CREC extension with N-S oriented faults, the Las Vegas Valley Shear Zone with NW-SE orientations, and the Lake Mead Fault System with NE-SW orientations. Fault scarps 21-BC-01, 21-BC-02, and 21-BC-03 have generally E-W, or near E-W, striking orientations and are within a few meters

of one another. Evidence of strike-slip motion is seen in the multiple sets of slickenlines with orientations parallel to the fault scarp at the field and hand sample scale, consistent with strike-slip motion (Fig. 12). The E-W orientation of these faults is consistent with the minor amounts of N-S extension of the Lake Mead area in the early Miocene (Anderson et al., 1972; Faulds et al., 2001), however, the U-Pb zircon ages of 21-BC-03 indicate that the volcanics are younger than the phase of N-S extension. E-W strike-slip faults were measured in the southern Lake Mead area, within one km of the studied scarps, by Beard et al., 2014 though the kinematic model in that study did not explain the origin of the E-W strike-slip faults and they were attributed to complex faulting and rotation (Fig. 23; Beard et al., 2014).

The measured orientations of the fault scarps in outcrop 21-BC-04 are generally NW-SE, nearly vertical dipping slightly toward the E, with slickenlines that indicate dominantly strike-slip motion (Fig. 10B, 12). The orientation is consistent with faults in the NW-SE right-lateral Las Vegas Valley Shear Zone (Anderson et al., 1972; Weber & Smith, 1987; Fuerbach et al., 1993; Anderson and Beard, 2010), however, 21-BC-04 is a minor fault and may be a conjugate or a shear from other larger faults in this area.

The measured NE-SW strike, E-SE dip orientations, strike-slip to slightly oblique slip slickenline orientations, and scale of 21-BC-05 outcrops suggests that it is associated with the left-lateral strike-slip faults of the Lake Mead fault zone (Anderson et al., 1972; Faulds et al., 2001). The 21-BC-05 fault scarp is mapped as the southern end of the NE-SW striking Hamblin Bay Fault (Weber and Smith, 1987). The results of this study support that the fault scarps in outcrop 21-BC-05 are genetically related to the Lake Mead fault zone and sits at the end of the NE-SW portion of the Hamblin Bay fault.

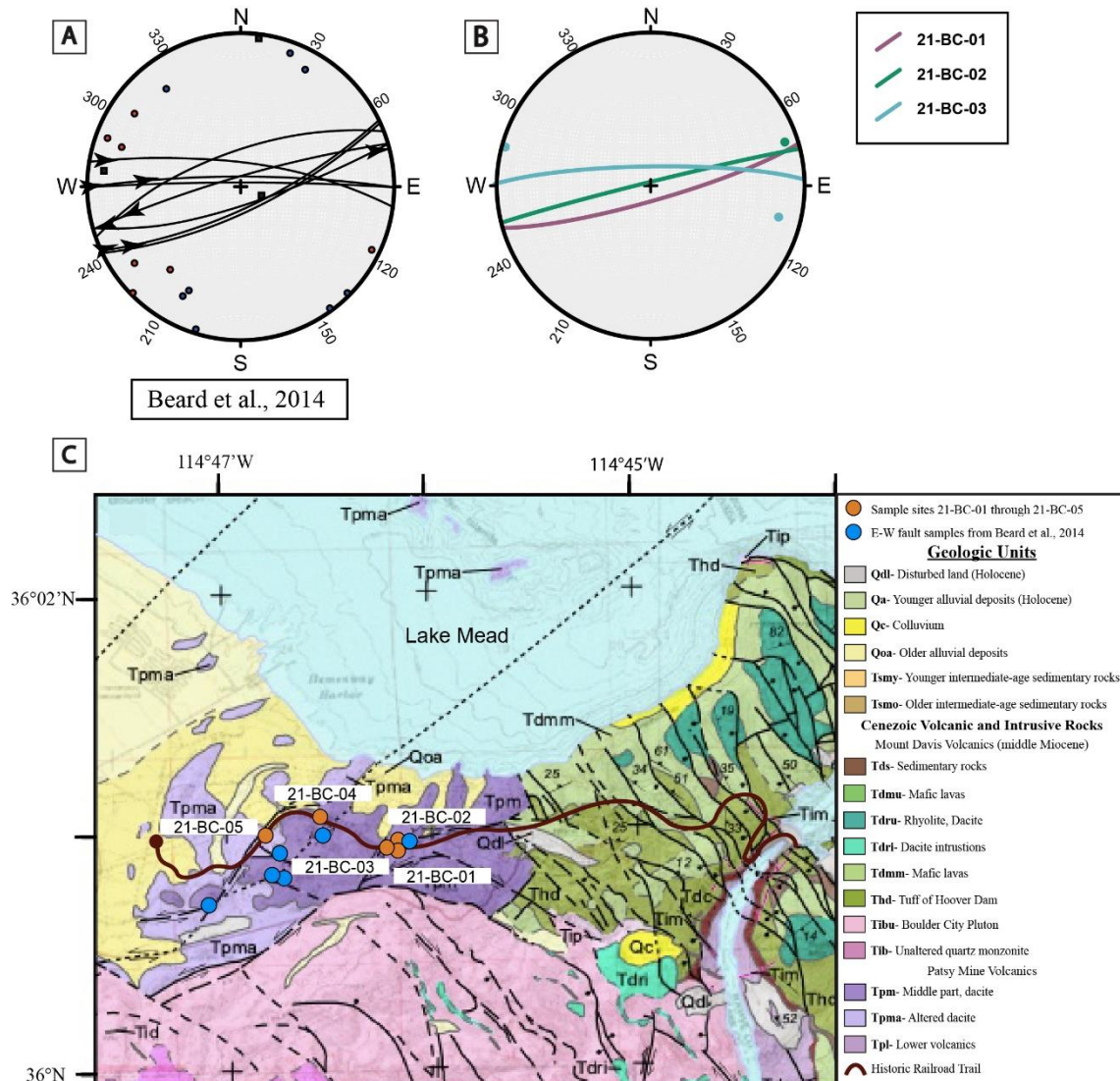


Figure 23. E-W orientated fault measurement comparison.

Comparison of fault orientations from A) the E-W faults from the Beard et al., 2014 (A, blue dots on map) and E-W trending faults from 21-BC-01, 21-BC-02, 21-BC-03. C) geologic map of the field area with the sample sites from the Beard et al., 2014 study (blue circles) and the sample sites in this study (orange circles) Adapted from Beard et al., 2014.

All the hematite coated faults from this study must be younger than ~13 Ma and show evidence of multiple slip events (i.e., two or more slip events). The timing, orientations, and dominantly strike-slip motion of these faults are consistent with being associated with the coeval

Lake Mead fault zone and Las Vegas Valley Shear zone between 13 – 9 Ma (Hinz et al., 2018; Faulds et al., 2022). Activity along the studied faults was likely influenced by multiple tectonic drivers during this time in the complex strain field produced by the intersection between Las Vegas Valley Shear Zone, Lake Mead Fault System, and the Northern Colorado River Extensional Corridor.

V.III. Fault Processes and Deformation Mechanisms

The presence of hematite plate morphologies is interpreted as the primary mineralization morphology of the hematite along the faults (McDermott et al., 2017; Ault, 2020). The strain localization and evidence of fault reactivation along the hematite-rich fault surfaces is likely because the hematite is weaker than the surrounding host rocks (Ault et al., 2015; McDermott et al., 2017; Calzolari et al., 2019). The fault surfaces have a cataclastic texture of micro-nano particles of comminuted hematite plates along the surface and top portions of the fault mirror volumes. The sub-angular fragments of plates at the surface require post-mineralization cataclasis and comminution. All five samples have host rock particles in the fault mirror volumes, with varying relative abundances. Comminution, as evident by the grain size reduction of both hematite and host rock particles toward the slip surface, is observed in all samples. Four of the five outcrop sites, all except 21-BC-05, show multiple domains in the fault mirror volume which may record multiple discrete mineralization and/or slip events. Samples 21-BC-01 – 21-BC-04 also contain gradational contacts between the fault mirror volume and host rock (Fig. 14, 15A, 15B, 17A, 17B). These contacts have the largest grain sizes within the fault mirror volume and are undulatory (on a <500 μm scale), showing a small amount of mixing between the two populations (Fig. 14, 17A). The mixing that suggests deformation was accommodated through the hematite-rich fault mirror volume, with the highest strain being localized along the slip surface. These observations suggest

deformation in the fault mirror volume by granular flow, which can occur at strain rates ranging from subseismic to seismic (e.g., Rowe and Griffith, 2015). The plucking and sorting of host rock clasts, cataclasite, and injection of hematite into off-fault cracks support that the granular flow may have been fluidized (Rowe and Griffith, 2015). Hematite grain morphologies along slip surfaces are distinct from polygonal or sintered grains associated with high coseismic friction-generated temperatures (Fig. 2; Fig. 3), suggesting there were not high coseismic temperatures along these surfaces. Together, the cataclastic textures and lack of sintering/recrystallization morphologies suggest that the slip events that occurred on the fault surface were at the lower end of seismic to aseismic slip rates. However, the presence of fault mirrors along all the studied fault scarps is evidence that the slip rates were seismic because fault mirrors have only been produced in laboratory deformation experiments at seismic slip rates (e.g., Rowe and Griffith, 2015) suggesting that the studied fault mirrors experienced seismic slip rates. The injection veins filled with hematite observed in sample 21-BS-05 (Fig. 19A) are evidence of transient fluid overpressure events associated with deformation.

The studied faults likely hosted seismicity in the past. During slip along the weak hematite-rich areas of the host rock, the comminution of surface particles and fluid overpressure would have further weakened the surfaces. The surfaces may have experienced some frictional heating and thus weakening, but not at high enough temperatures to cause hematite sintering or recrystallization. The occurred strain was localized within the fault mirror volumes, culminating along the mirrored surfaces which are interpreted to represent the PSZs. There is no textural evidence of neomineralization (i.e., platy hematite growth) over-printing the cataclastic hematite textures in the studied faults implying that this deformation was the most recent event to affect the samples.

The samples also indicate that fluids were present associated with the hematite mineralization, during, and after deformation. There is not sufficient evidence to discriminate if hematite mineralization occurred before deformation began, but fluid injection veins in 21-BC-05 suggest that hematite mineralization and deformation may have been coeval, at least in some cases. The discordant zircons that record Pb loss further support hydrothermal fluid circulation along the faults. The interstitially filled cracks in 21-BC-02, 21-BC-03, and 21-BC-04 have FeO needles that have a high-aspect ratio and are consistent with goethite morphologies (Cornell and Schwertmann, 2003). The ‘needles’ look fragile and appear undeformed, suggesting that they mineralized after the deformation ceased. Therefore, the faults may have acted as fluid pathways after deformation. The evidence for post-deformation mineralization is most prevalent in the samples from 21-BC-04 that have the largest population of filled-in fractures as well as undeformed goethite needles.

V.IV. Recommended Future Work

Further work recommended includes a detailed mapping project of the units in the SW portion of the Lake Mead region, specifically designating the sections of the Patsy Mine Volcanics, for a greater understanding of the episodic Miocene volcanism and the combined influence of significant faulting systems with the shear zone in a region that has experienced a significant amount of extension.

Further elemental and microtextural analysis to expand on the observations from this study includes a comparative study between the elemental compositions and geochronology of the tuff of Hoover Dam and the tuff of Bridge Spring is recommended to analyze any genetic compatibility and to better understand the temporal and spatial parameters of the volcanics in this area. The tuff of Hoover Dam is near the field area of the volcanics featured in this study. The tuff of Bridge Spring is the unit overlying the Patsy Mine Volcanics (Fig. 6) (Anderson et al., 1972; Gans and

Bohrson, 1998). Further investigation into the temporal and geochemical history of the fault mirror surfaces would include analysis using Transmission Electron Microscopy (TEM). Cathodoluminescence (CL) should be used to map the fault surfaces and better characterize the fault surface on a nano-particle scale.

Continued geochronological and thermochronological examinations of the volcanic host rock and fault mirrors would contribute to further illuminating the thermal and mechanical histories. (U-Th)/He analysis of the hematite on the fault surface, with a closure temperature range of ~25 – 250 °C (assuming a 10 °C/Myr cooling rate) would provide better constraints on hematite mineralization timing and the most recent deformation event that increased temperature conditions enough to partially or fully reset the hematite dates (Farley and Flowers, 2012; Evenson et al., 2014; Farley, 2018; Ault et al., 2019).

VI. CONCLUSION

New U-Pb zircon dating results from the exposed Patsy Mine Volcanic fault scarps hosting fault mirror surfaces near Lake Mead, NV exhibit dates of crystallization as 12.90 ± 0.31 Ma and 13.86 ± 0.27 Ma with 2σ error. The new (U-Th)/He apatite data set and HeFTy inverse modeling indicate a geologic history of shallow burial around $\sim 10 - 8$ Ma followed by exhumation $\sim 4 - 2$ Ma. The apatite He dates are partially reset and range from 5.64 ± 0.46 Ma to 12.4 ± 0.36 Ma with 2σ standard error uncertainty. These interpretations have been reinforced through the micro-nano particle grain textures and morphologies within the fault mirror volume. These surfaces provide evidence of deformation post-mineralization, sub-seismic to aseismic slip rates, frictional sliding or dislocation creep, low-temperature conditions, accommodation of multiple episodes of deformation, and indications of the presence of fluids. The orientations of these fault scarps indicate three different tectonic system genetics, E-W strike-slip faults, the NE-SW right-lateral strike-slip faults of the Lake Mead fault system, and the NW-SE right-lateral strike-slip faults of the Las Vegas Valley shear zone. The Lake Mead region is a locally and regionally tectonically complex area within the North American Western Cordillera, this study aims to illuminate the temporal and spatial history of the localized fault mirror surfaces present in the Patsy Mine Volcanics.

APPENDIX

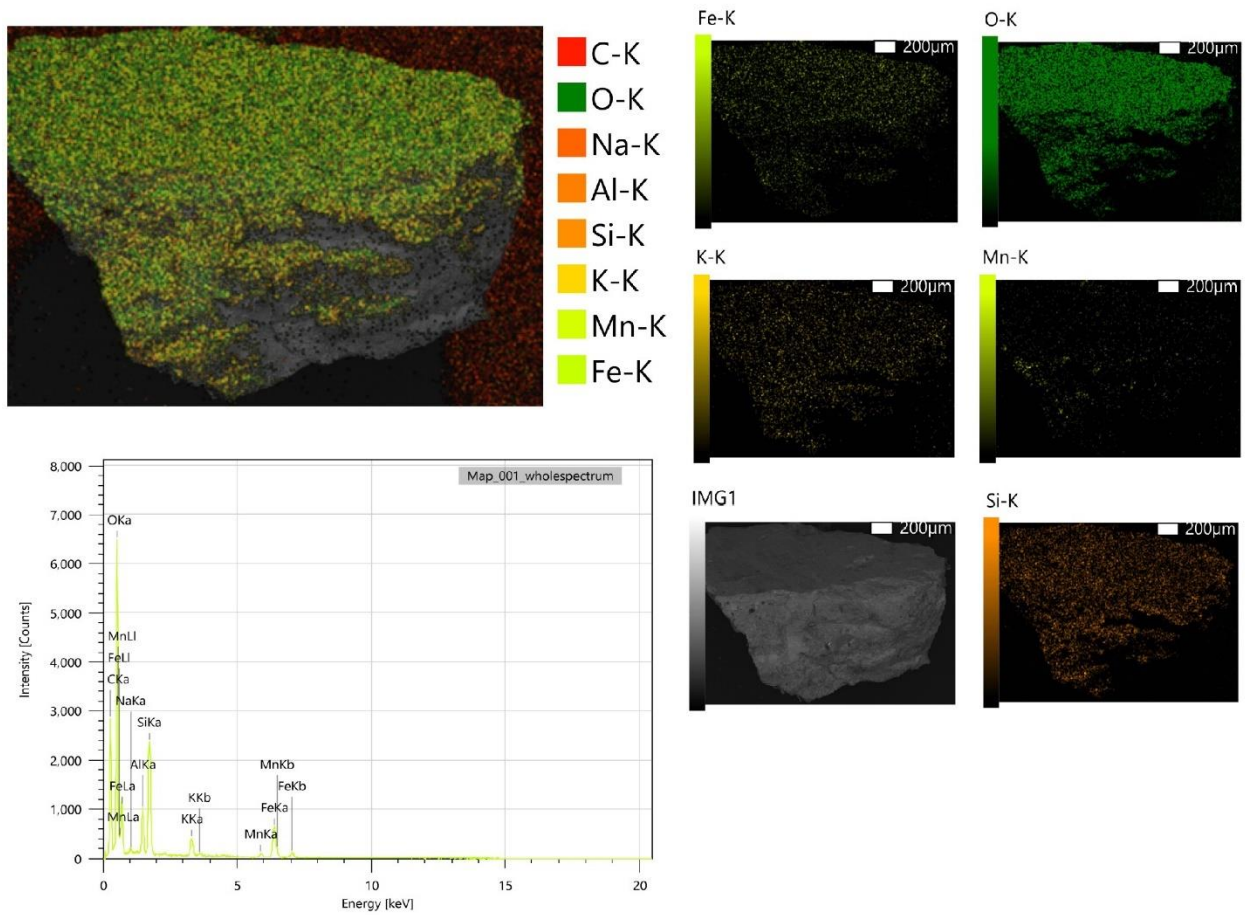


Figure A1. EDS map of 21-BC-03 aliquot.

No carbon-coating. Elemental map of fault mirror surface (top left), individual elemental maps (right), and elemental spectrum plot of intensity (Counts) v. Energy (keV) (bottom left).

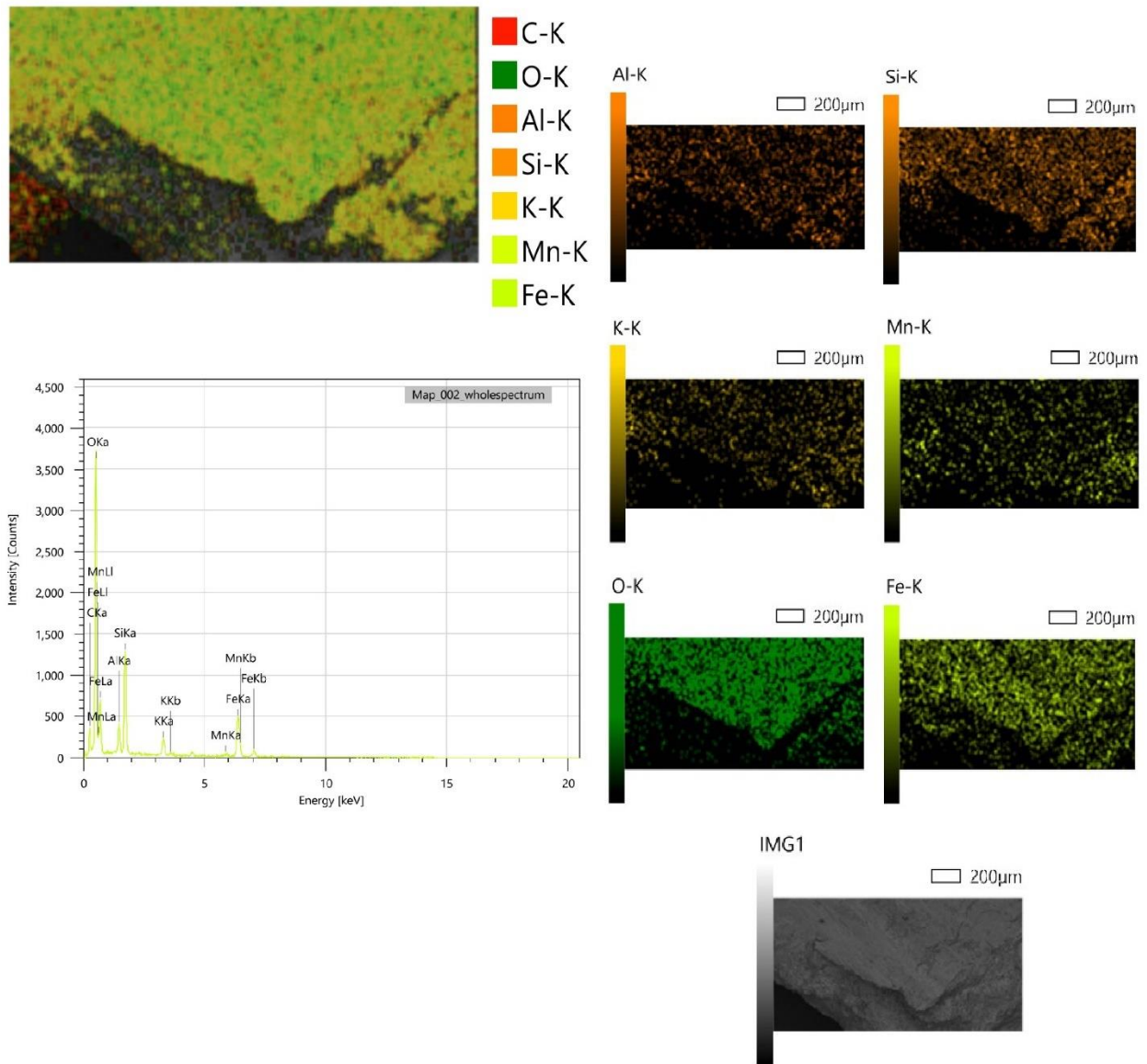


Figure A2. EDS map of 21-BC-05 aliquot.

No carbon-coating. Elemental map of fault mirror surface (top left), individual elemental maps (right), and elemental spectrum plot of intensity (Counts) v. Energy (keV) (bottom left).

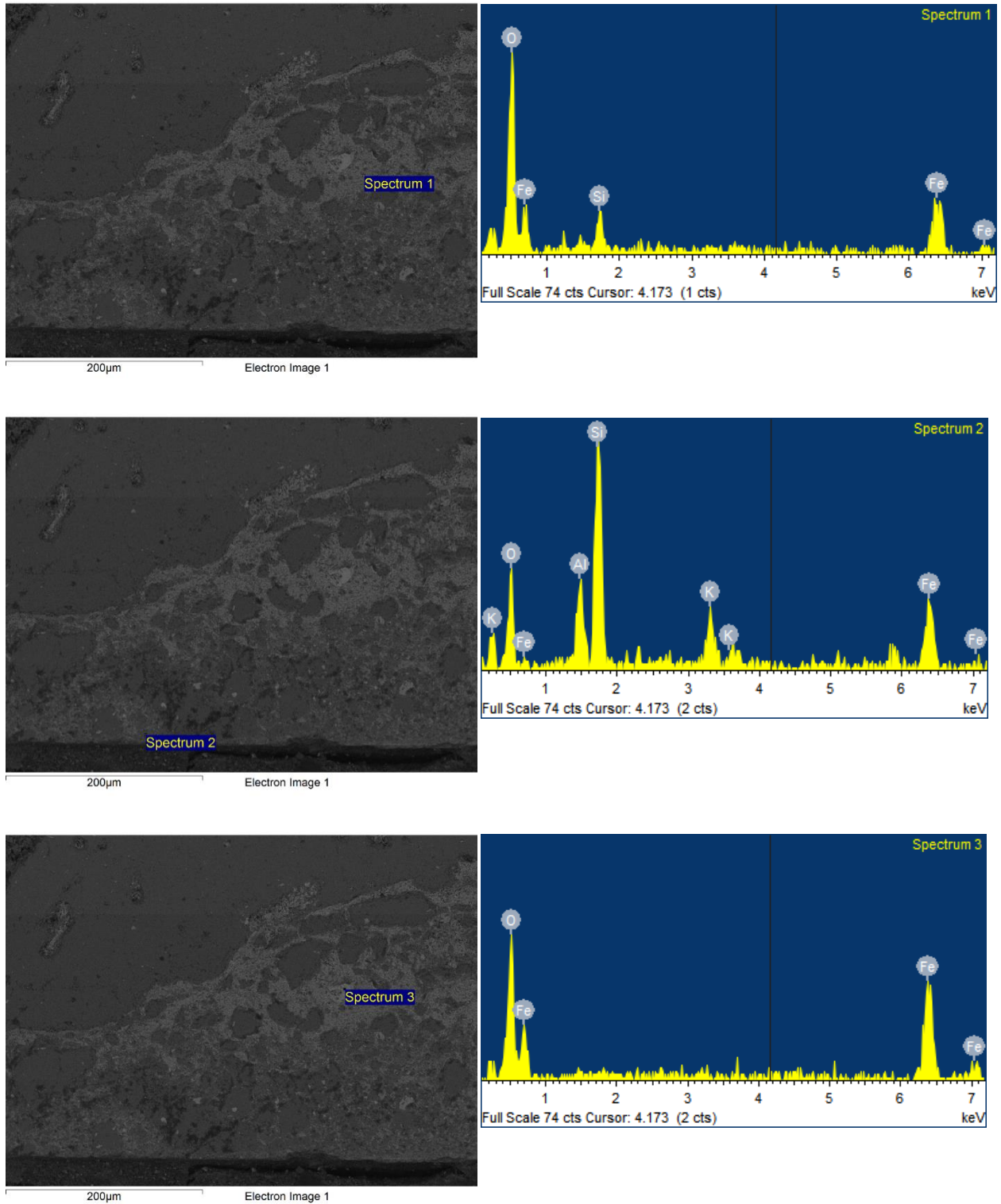


Figure A3. EDS results from 21-BC-04. SEM images showing EDS spot analysis locations (left) with corresponding spectra showing elemental detection and intensity of concentration through counts vs. energy (keV).

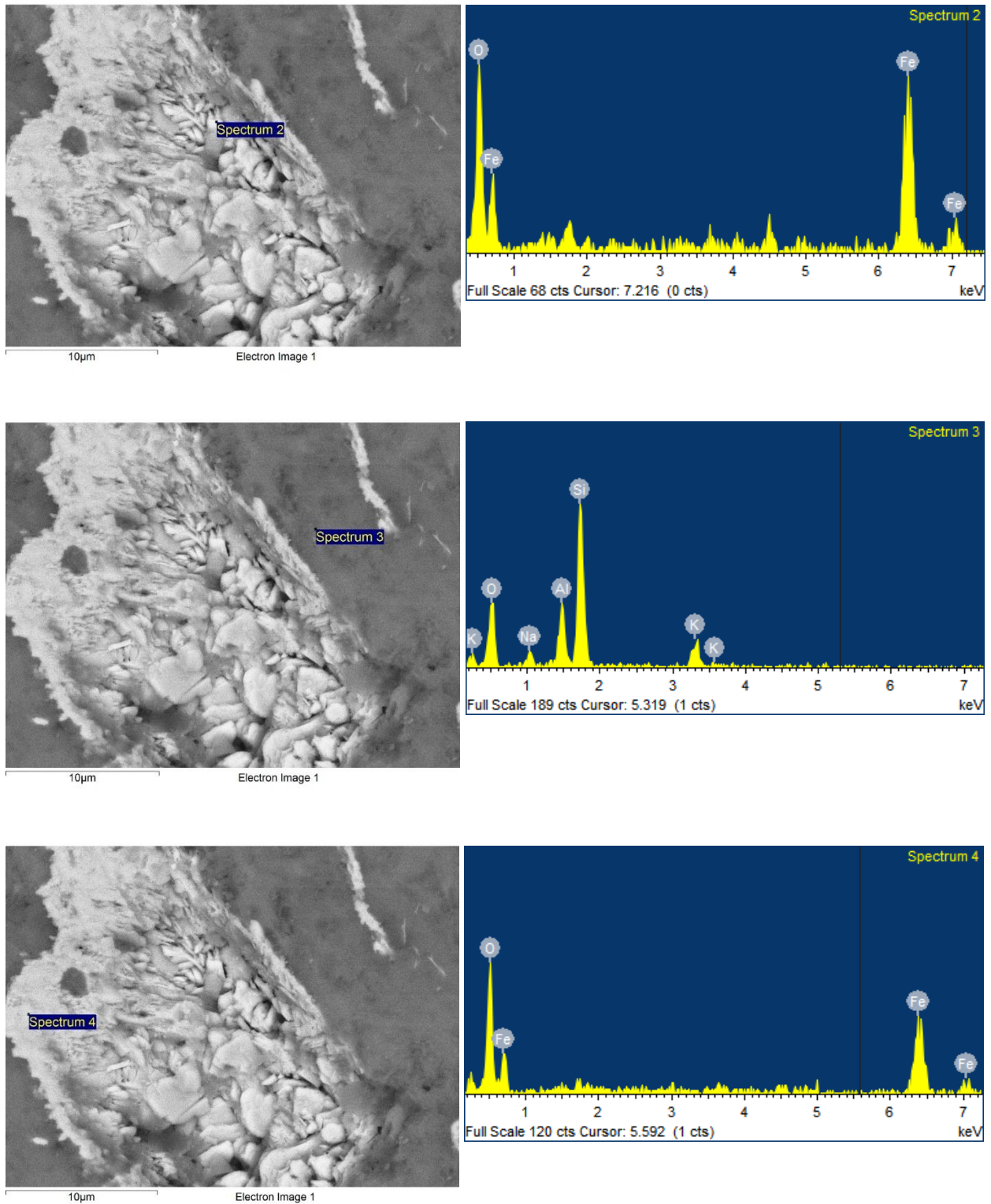


Figure A4. EDS results from 21-BC-02. SEM images showing EDS spot analysis locations (left) with corresponding spectra showing elemental detection and intensity of concentration through counts vs. energy (keV).

Table A1. U-Pb Zircon Analysis Raw data

Table 1: Raw U-Pb Zircon Analysis																			
Sample Name:										207/235		206/238		207/206		Best age			
Grain#	[U] ppm	Th/U	207/235	2σ error	206/238	2σ error	RHO	207/206	2σ error	Age Ma	2σ error	Age (Ma)	2σ error	Age (Ma)	2σ error	(Ma)	2σ error	% Discordance*	
BC-03_1	133	2.71	0.02	2.66E-03	2.08E-03	6.60E-05	0.23	0.07	1.04E-02	18.4	2.5	13.4	0.4	680	244	13.4	0.4		27
BC-03_3	75.8	1.58	0.02	3.59E-03	2.23E-03	9.06E-05	0.36	0.06	1.32E-02	17.3	3.6	14.4	0.6	1230	251	14.4	0.6		16.9
BC-03_6	193	2.47	0.02	2.99E-03	2.14E-03	8.16E-05	0.1	0.06	1.05E-02	15.8	3	13.8	0.5	136	436	13.8	0.5		12.6
BC-03_8	141	1.81	0.02	3.21E-03	2.12E-03	7.93E-05	0.1	0.06	1.10E-02	16.3	3.2	13.6	0.5	714	305	13.6	0.5		16.4
BC-03_9	37.1	1.99	0.06	9.21E-03	2.69E-03	1.35E-04	0.39	0.18	3.39E-02	57.8	8.7	17.3	0.9	2460	189	17.3	0.9		70
BC-03_10	65.1	2.14	0.06	1.15E-02	2.70E-03	1.31E-04	0.05	0.13	2.17E-02	56.8	11	17.4	0.8	1780	222	17.4	0.8		69.4
BC-03_11	54.3	1.52	0.98	1.35E-01	6.09E-02	8.61E-03	0.04	0.11	1.11E-02	518	64.5	365	50.9	1810	132	364.6	50.9		29.6
BC-03_12	212	0.83	0.02	2.75E-03	2.24E-03	7.55E-05	0.39	0.05	1.03E-02	15.8	2.7	14.5	0.5	680	254	14.5	0.5		8.6
BC-03_13	32.4	2.49	0.05	9.79E-03	2.51E-03	1.57E-04	0.36	0.19	3.80E-02	51.5	9.3	16.1	1	2630	189	16.1	1		68.7
BC-03_14	144	2.03	0.04	4.33E-03	2.27E-03	7.58E-05	0.09	0.12	1.34E-02	36.2	4.1	14.6	0.5	1780	187	14.6	0.5		59.6
BC-03_16	102	1.55	0.02	3.45E-03	2.10E-03	8.27E-05	0.3	0.08	1.26E-02	21.8	3.4	13.5	0.5	1140	255	13.5	0.5		37.8
BC-03_20	121	1.6	0.07	1.20E-02	2.71E-03	1.40E-04	0.25	0.18	2.72E-02	72	11.4	17.5	0.9	2010	329	17.5	0.9		75.8
BC-03_24	87.2	2.77	0.47	4.84E-02	6.23E-03	4.10E-04	0.59	0.44	3.22E-02	347	32.3	40	2.6	3510	158	40	2.6		88.5
BC-03_25	78.5	1.33	0.06	5.80E-03	2.60E-03	9.53E-05	0.31	0.18	1.87E-02	57.9	5.5	16.7	0.6	2410	165	16.7	0.6		71.1
BC-03_28	143	2.37	0.02	3.79E-03	2.22E-03	8.34E-05	0.08	0.07	1.28E-02	20	3.7	14.3	0.5	983	264	14.3	0.5		28.7
BC-03_29	263	3.65	0.02	1.95E-03	2.13E-03	5.63E-05	0.23	0.05	6.27E-03	16.6	1.9	13.7	0.4	188	260	13.7	0.4		17.4
BC-03_35	65.5	1.32	0.07	1.07E-02	2.65E-03	1.38E-04	0.06	0.17	2.69E-02	65	10	17.1	0.9	2740	173	17.1	0.9		73.7
BC-03_37	119	1.13	0.01	2.36E-03	2.20E-03	6.74E-05	0.05	0.05	8.78E-03	14.3	2.4	14.2	0.4	1020	170	14.2	0.4		0.9
BC-03_42	89.1	1.02	2.91	4.37E-02	2.38E-01	1.68E-03	0.05	0.09	1.18E-03	1380	11.2	1380	8.9	1380	25.4	1381.5	25.4		0.3
BC-03_43	315	2.12	0.02	1.49E-03	2.14E-03	5.82E-05	0.31	0.06	5.48E-03	16.8	1.5	13.8	0.4	265	229	13.8	0.4		17.9
BC-03_45	113	1.48	0.01	2.58E-03	2.19E-03	7.15E-05	0.26	0.05	9.74E-03	13.7	2.6	14.1	0.5	1240	193	14.1	0.5		2.6
BC-03_4	22.1	2.02	0.12	2.55E-02	3.05E-03	2.58E-04	0.38	0.27	8.70E-02	97.5	22.2	19.6	1.7	3400	188	19.6	1.7		79.9

Sample Name:										207/235		206/238		207/206	Best age			
Grain#	[U] ppm	Th/U	207/235	2σ error	206/238	2σ error	RHO	207/206	2σ error	Age Ma	2σ error	Age (Ma)	2σ error	Age (Ma)	2σ error	(Ma)	2σ error	% Discordance*
BC-05_1	38.7	2.62	0.28	7.31E-02	3.97E-03	4.79E-04	0.36	0.35	4.29E-02	170	29.4	25.5	3.1	3380	165	25.5	3	85
BC-05_2	48.4	1.2	0.89	3.29E-02	1.02E-01	1.20E-03	0.23	0.06	2.36E-03	640	17.8	625	7	627	85.9	624.8	7	2.3
BC-05_5	51.1	0.78	2.73	4.63E-02	2.30E-01	2.06E-03	0.19	0.09	1.35E-03	1330	12.7	1330	10.8	1320	30.4	1319.7	30.4	0.9
BC-05_6	24.4	1.88	0.44	2.67E-02	5.78E-02	9.32E-04	0.24	0.06	3.51E-03	362	19.1	362	5.7	278	146	362.2	5.7	0.2
BC-05_8	22.9	0.71	0.88	4.10E-02	1.02E-01	1.34E-03	0.21	0.06	3.00E-03	629	22.4	624	7.8	615	104	623.8	7.8	0.9
BC-05_9	22.7	0.57	2.06	6.83E-02	1.95E-01	2.79E-03	0.07	0.08	2.40E-03	1130	22.7	1150	15	1060	64.5	1147	15	1.8
BC-05_10	167	1.66	0.02	3.21E-03	2.31E-03	1.07E-04	0.14	0.06	2.27E-02	16.4	3.2	14.9	0.7	414	291	14.9	0.7	9.2
BC-05_11	142	2.36	0.15	1.40E-02	3.47E-03	1.50E-04	0.06	0.32	2.57E-02	141	12	22.3	1	3210	142	22.3	1	84.2
BC-05_12	642	0.53	0.54	1.30E-02	4.24E-02	4.09E-04	0.47	0.09	2.45E-03	435	8.6	267	2.5	1410	52.4	267.5	2.5	38.4
BC-05_13	128	1.27	6.69	1.01E-01	3.72E-01	4.17E-03	0.19	0.13	1.72E-03	2070	14.1	2040	19.6	2090	23.4	2090.2	23.4	2.4
BC-05_14	30	0.44	1.73	9.56E-02	1.67E-01	2.78E-03	0.2	0.07	4.18E-03	983	37.2	995	15.3	869	125	995.3	15.3	1.2
BC-05_15	1210	0.87	4.06	5.02E-02	2.87E-01	1.95E-03	0.36	0.1	1.31E-03	1640	9.9	1630	9.8	1650	24.1	1645.6	24.1	1.1
BC-05_16	1430	0.67	0.88	2.41E-02	1.01E-01	1.05E-03	0.04	0.06	1.65E-03	633	13.1	623	6.2	637	58.3	622.5	6.2	1.6
BC-05_17	464	1.89	0.03	6.29E-03	2.32E-03	1.40E-04	0.36	0.1	2.91E-02	28.9	6.2	14.9	0.9	2460	202	14.9	0.9	48.4
BC-05_19	1290	1.91	0.01	1.95E-03	1.90E-03	5.58E-05	0.28	0.05	8.01E-03	13.4	1.9	12.2	0.4	720	211	12.2	0.4	8.8
BC-05_20	747	0.24	0.75	1.87E-02	9.09E-02	7.69E-04	0.18	0.06	1.45E-03	567	10.7	561	4.6	556	55.2	560.6	4.5	1.1
BC-05_21	470	2.41	0.02	3.51E-03	2.01E-03	1.02E-04	0.06	0.06	1.48E-02	15.7	3.5	12.9	0.7	1640	221	12.9	0.7	17.5
BC-05_22	232	2.2	0.04	7.52E-03	2.36E-03	1.27E-04	0.48	0.14	2.88E-02	37.6	7	15.2	0.8	2590	176	15.2	0.8	59.6
BC-05_23	582	2.97	0.01	2.87E-03	2.19E-03	7.94E-05	0.33	0.05	1.10E-02	14.3	2.8	14.1	0.5	1090	229	14.1	0.5	1
BC-05_24	349	2.72	0.01	3.67E-03	1.95E-03	9.14E-05	0.4	0.06	1.93E-02	13.7	3.6	12.5	0.6	2070	203	12.5	0.6	8.3
BC-05_25	132	0.69	1.72	5.21E-02	1.66E-01	1.93E-03	0.26	0.08	2.34E-03	1010	19	989	10.6	1010	64.9	989.5	10.6	1.6
BC-05_27	672	2.65	0.02	2.96E-03	2.20E-03	9.84E-05	0.32	0.06	1.27E-02	17.6	2.9	14.2	0.6	1080	252	14.2	0.6	19.4
BC-05_28	301	0.27	1.52	3.69E-02	1.54E-01	1.35E-03	0.31	0.07	1.80E-03	934	14.6	925	7.5	937	52.6	925	7.5	1
BC-05_29	1110	1.73	0.02	2.17E-03	2.03E-03	6.71E-05	0.45	0.06	9.15E-03	16.3	2.2	13.1	0.4	828	232	13.1	0.4	20.1
BC-05_30	329	0.42	6.69	7.99E-02	3.77E-01	3.06E-03	0.22	0.13	1.36E-03	2070	10.7	2060	14.5	2070	18.4	2070.9	18.4	0.3
BC-05_31	1590	2.78	0.01	1.63E-03	1.93E-03	4.93E-05	0.29	0.06	6.47E-03	14.7	1.6	12.4	0.3	119	251	12.4	0.3	15.4
BC-05_32	151	1.13	0.79	3.37E-02	9.25E-02	1.21E-03	0.28	0.06	2.75E-03	581	19.4	570	7.1	534	103	570.1	7.1	1.9
BC-05_34	460	0.66	0.52	1.60E-02	6.68E-02	6.02E-04	0.24	0.06	1.79E-03	419	10.9	417	3.6	346	78	416.6	3.6	0.5
BC-05_35	244	1.96	0.31	3.57E-02	4.15E-03	3.02E-04	0.26	0.55	6.51E-02	253	26.3	26.7	1.9	3400	163	26.7	1.9	89.5
BC-05_36	263	0.71	0.64	2.21E-02	7.93E-02	8.15E-04	0.18	0.06	2.05E-03	493	13.6	492	4.9	396	81.4	492	4.9	0.2
BC-05_37	359	2.79	0.03	5.75E-03	2.14E-03	1.08E-04	0.23	0.09	2.46E-02	25.1	5.6	13.8	0.7	2280	193	13.8	0.7	45
BC-05_38	253	0.92	4.38	9.84E-02	3.01E-01	3.69E-03	0.25	0.11	2.34E-03	1710	18.6	1700	18.3	1710	41.1	1706.4	41.1	0.6
BC-05_41	449	0.29	0.5	1.51E-02	6.35E-02	6.15E-04	0.27	0.06	1.78E-03	410	10.1	397	3.7	408	72.6	396.5	3.7	3.3
BC-05_43	1200	0.62	0.42	1.11E-02	5.20E-02	4.62E-04	0.15	0.06	1.56E-03	358	7.8	327	2.8	505	56.6	327	2.8	8.6
BC-05_44	589	2.72	0.01	3.63E-03	2.02E-03	1.00E-04	0.27	0.05	1.49E-02	14.3	3.8	13	0.6	1720	253	13	0.6	8.7
BC-05_45	366	2.6	0.02	4.88E-03	2.25E-03	1.17E-04	0.33	0.06	2.16E-02	14.8	4.8	14.5	0.8	2260	235	14.5	0.8	2.2

Sample Name:																	207/235	206/238	207/206	Best age		
Grain#	[U] ppm	Th/U	207/235	2σ error	206/238	2σ error	RHO	207/206	2σ error	Age Ma	2σ error	Age (Ma)	2σ error	Age (Ma)	2σ error	(Ma)	2σ error	% Discordance*				
PLES_1	237	0.1	0.39	7.61E-03	5.28E-02	3.53E-04	0.23	0.05	1.04E-03	336	5.5	331	2.2	333	45.6	331.4	2.2	1.3				
PLES_2	172	0.11	0.4	8.22E-03	5.48E-02	4.22E-04	0.23	0.05	1.12E-03	340	6	344	2.6	292	49.8	344.1	2.6	1.2				
PLES_4	197	0.11	0.4	9.17E-03	5.37E-02	4.44E-04	0.1	0.05	1.20E-03	337	6.7	337	2.7	295	51.9	337.2	2.7	0				
PLES_3	1650	0.12	0.38	8.94E-03	5.16E-02	4.38E-04	0.17	0.05	1.25E-03	324	6.6	324	2.7	255	56.4	324.3	2.7	0.2				
PLES_5	1560	0.12	0.39	7.74E-03	5.29E-02	3.67E-04	0.08	0.05	1.06E-03	331	5.6	332	2.3	316	44.8	332.3	2.2	0.5				
FC1_1	457	0.61	1.95	1.63E-02	1.86E-01	1.24E-03	0.17	0.08	5.01E-04	1100	5.6	1100	6.8	1090	13.2	1099.6	6.8	0.1				
FC1_2	457	0.65	1.95	1.59E-02	1.86E-01	1.19E-03	0.21	0.08	4.96E-04	1100	5.5	1100	6.5	1090	13.2	1097.6	6.5	0.1				
FC1_3	457	0.68	1.95	1.62E-02	1.86E-01	1.27E-03	0.18	0.08	5.18E-04	1100	5.6	1100	6.9	1100	13.3	1099.1	6.9	0.1				
FC1_4	457	0.67	1.95	1.56E-02	1.86E-01	1.20E-03	0.24	0.08	4.96E-04	1100	5.4	1100	6.5	1090	13	1099.2	6.5	0.1				
FC1_5	457	0.67	1.95	1.60E-02	1.86E-01	1.13E-03	0.22	0.08	5.09E-04	1100	5.5	1100	6.1	1100	13.2	1098.3	6.1	0.1				
FC1_6	457	0.67	1.95	1.47E-02	1.86E-01	1.16E-03	0.73	0.08	4.86E-04	1100	5.1	1100	6.3	1100	12.3	1099.2	6.3	0.1				
FC1_7	456	0.47	1.95	2.02E-02	1.86E-01	1.47E-03	0.18	0.08	7.89E-04	1100	7	1100	8	1100	16.6	1098	8	0.1				
FC1_8	457	0.49	1.95	2.05E-02	1.86E-01	1.43E-03	0.52	0.08	6.55E-04	1100	7	1100	7.6	1080	17.4	1100.4	7.6	0.2				
FC1_9	458	0.49	1.95	1.79E-02	1.86E-01	1.38E-03	0.25	0.08	5.50E-04	1100	6.1	1100	7.5	1090	14.4	1097.6	7.5	0.1				
FC1_10	456	0.49	1.96	1.77E-02	1.86E-01	1.39E-03	0.38	0.08	6.13E-04	1100	6.1	1100	7.6	1090	16	1100.3	7.6	0.1				
FC1_11	458	0.49	1.95	1.86E-02	1.85E-01	1.50E-03	0.5	0.08	6.02E-04	1100	6.5	1100	8.2	1080	16.7	1096.4	8.2	0.1				
FC1_12	453	0.66	1.96	3.10E-02	1.86E-01	1.40E-03	0.2	0.08	1.14E-03	1100	10.8	1100	7.6	1080	30.8	1099.9	7.6	0				
FC1_13	458	0.66	1.95	3.17E-02	1.86E-01	1.39E-03	0.5	0.08	1.18E-03	1090	11	1100	7.6	1080	30.8	1098.6	7.6	0.4				
FC1_14	457	0.66	1.95	3.09E-02	1.86E-01	1.32E-03	0.23	0.08	1.18E-03	1090	10.8	1100	7.2	1090	30.3	1098.2	7.2	0.4				
FC1_15	457	0.65	1.96	3.20E-02	1.86E-01	1.33E-03	0.34	0.08	1.27E-03	1100	11	1100	7.2	1070	33.4	1099.1	7.2	0.3				
FC1_16	457	0.63	1.95	3.11E-02	1.86E-01	1.42E-03	0.19	0.08	1.21E-03	1100	10.8	1100	7.7	1060	32.3	1099	7.7	0.3				
FC1_17	457	0.63	1.95	3.17E-02	1.86E-01	1.35E-03	0.19	0.08	1.24E-03	1100	11.1	1100	7.4	1070	32.7	1099.1	7.3	0.4				
FC1_18	456	0.6	1.96	3.49E-02	1.85E-01	1.45E-03	0.14	0.08	1.36E-03	1100	12.3	1100	7.9	1110	34.9	1096.5	7.9	0				
FC1_19	456	0.6	1.95	3.67E-02	1.86E-01	1.55E-03	0.11	0.08	1.36E-03	1090	12.2	1100	8.6	1080	36.4	1101.4	8.6	0.7				
FishCyn_1	181	0.6	0.03	2.42E-03	4.25E-03	7.16E-05	0.17	0.05	4.27E-03	30.1	2.4	27.3	0.5	415	148	27.3	0.5	9.3				
FishCyn_4	114	0.45	0.03	3.34E-03	4.24E-03	9.72E-05	0.21	0.05	5.79E-03	29.7	3.3	27.3	0.6	-229	288	27.3	0.6	7.9				
FishCyn_3	2500	0.64	0.03	2.73E-03	4.09E-03	7.86E-05	0.05	0.05	4.61E-03	28.5	2.7	26.3	0.5	-105	230	26.3	0.5	7.7				
FishCyn_2	926	0.63	0.03	2.55E-03	4.10E-03	8.08E-05	0.28	0.05	4.77E-03	25.9	2.5	26.4	0.5	-97.9	225	26.4	0.5	1.7				
FishCyn_5	890	0.55	0.03	2.98E-03	4.09E-03	1.09E-04	0.21	0.05	5.41E-03	28.1	3	26.3	0.7	177	209	26.3	0.7	6.3				
Sample Name:																	207/235	206/238	207/206	Best age		
Grain#	[U] ppm	Th/U	207/235	2σ error	206/238	2σ error	RHO	207/206	2σ error	Age Ma	2σ error	Age (Ma)	2σ error	Age (Ma)	2σ error	(Ma)	2σ error	% Discordance*				
BC-05_7	0.66	11.2	46.6	3.67E+00	3.92E-01	3.17E-02	0.59	1	6.43E-02	3720	80.8	2010	136	4420	76.8	DISC	DISC	54.6				
BC-05_26	4.15	5.91	102	4.04E+00	8.43E-01	3.24E-02	0.34	0.9	2.89E-02	4660	40.6	3860	109	4640	49.8	4639	49.8	16.7				

Table A2. (U-Th)/He Apatite Analysis Raw Data

Table 2: Raw (U-Th)/He Apatite Analysis												
sample name	He date	pmol He	1s ± pmol He	% 1s ± He	U+Th date	(238/233)m	(238/233)m 1s ±	(232/229)m	(232/229)m 1s ±	(152/147)m	(152/147)m 1s ±	
22A912_MO22_21-BC-03_Ap2	11/16/2022	1.59E-03	1.55E-05	0.97	12/2/2022	3.17E-02	3.74E-04	1.78E-01	5.01E-04	1.54E-01	1.02E-03	
22A913_MO22_21-BC-03_Ap3	11/16/2022	9.48E-04	1.95E-05	2.06	12/2/2022	3.30E-02	3.36E-04	8.45E-02	4.29E-04	2.55E-01	2.14E-03	
22A914_MO22_21-BC-03_Ap4	11/16/2022	4.13E-04	1.65E-05	3.98	12/2/2022	2.38E-02	2.53E-04	9.36E-02	2.05E-04	2.22E-01	1.26E-03	
22A915_MO22_21-BC-03_Ap5	11/16/2022	4.22E-03	2.16E-05	0.51	12/2/2022	2.19E-02	2.08E-04	1.18E+00	1.21E-03	3.04E-01	1.44E-03	
22A916_MO22_21-BC-03_Ap6	11/16/2022	6.19E-04	1.70E-05	2.75	12/2/2022	2.29E-02	1.70E-04	1.06E-01	5.25E-04	2.12E-01	1.90E-03	
22A917_MO22_21-BC-03_Ap7	11/16/2022	1.48E-03	1.77E-05	1.20	12/2/2022	2.26E-02	2.16E-04	1.89E-01	6.89E-04	2.99E-01	1.12E-03	
22A918_MO22_21-BC-03_Ap8	11/16/2022	9.54E-04	1.61E-05	1.69	12/2/2022	3.92E-02	3.03E-04	1.66E-01	1.32E-04	2.52E-01	1.11E-03	
22A920_MO22_21-BC-05_Ap2	11/17/2022	1.26E-03	1.65E-05	1.32	12/2/2022	5.05E-02	3.52E-04	3.06E-01	1.08E-03	5.24E-01	4.06E-03	
22A922_MO22_21-BC-05_Ap4	11/17/2022	3.70E-01	5.97E-04	0.16	12/2/2022	2.79E-02	3.02E-04	1.05E-01	1.57E-04	1.45E-02	5.31E-04	
22A895_LG22_DUR_Ap1	11/15/2022	1.77E-02	8.80E-05	0.50	12/2/2022	4.28E-02	1.67E-04	6.50E-01	1.65E-03	1.33E-01	1.26E-03	
22A924_LG22_DUR_Ap2	11/17/2022	5.09E-04	1.83E-05	3.60	12/2/2022	5.09E-03	7.60E-05	1.86E-02	1.05E-04	7.34E-03	3.32E-04	
Nbblk2	11/17/2022	5.61E-05	1.76E-05	31.36	12/2/2022	4.03E-03	5.30E-04	2.22E-03	8.33E-04	3.48E-03	1.35E-04	
					12/2/2022	2.88E-03	3.90E-05	1.62E-03	3.70E-05	3.67E-03	2.11E-04	
sample name	(44/42)m	(44/42)m 1s	ng U	1s ± ng U	% 1s ± ng U	ng Th	1s ± ng Th	% 1s ± ng Th	ng Sm	1s ± ng Sm	% 1s ± ng Sm	
22A912_MO22_21-BC-03_Ap2	1.19E-01	6.78E-03	1.38E-02	2.14E-04	1.55	9.48E-02	1.35E-03	1.43	2.98E-01	4.48E-03	1.51	
22A913_MO22_21-BC-03_Ap3	1.21E-01	1.84E-03	1.44E-02	2.19E-04	1.52	4.47E-02	6.43E-04	1.44	5.32E-01	8.16E-03	1.54	
22A914_MO22_21-BC-03_Ap4	1.42E-01	8.01E-03	9.96E-03	1.53E-04	1.54	4.96E-02	7.06E-04	1.42	4.52E-01	6.78E-03	1.50	
22A915_MO22_21-BC-03_Ap5	1.45E-01	8.69E-03	9.00E-03	1.37E-04	1.52	6.35E-01	9.03E-03	1.42	6.54E-01	9.76E-03	1.49	
22A916_MO22_21-BC-03_Ap6	1.09E-01	6.19E-03	9.52E-03	1.42E-04	1.49	5.63E-02	8.10E-04	1.44	4.28E-01	6.59E-03	1.54	
22A917_MO22_21-BC-03_Ap7	2.35E-01	3.74E-03	9.33E-03	1.42E-04	1.52	1.01E-01	1.44E-03	1.43	6.41E-01	9.51E-03	1.48	
22A918_MO22_21-BC-03_Ap8	1.25E-01	8.38E-03	1.75E-02	2.58E-04	1.48	8.87E-02	1.26E-03	1.42	5.23E-01	7.78E-03	1.49	
22A920_MO22_21-BC-05_Ap2	3.78E-01	1.88E-02	2.30E-02	3.37E-04	1.47	1.64E-01	2.34E-03	1.43	1.33E+00	2.07E-02	1.55	
22A922_MO22_21-BC-05_Ap4	3.07E-02	2.99E-04	1.19E-02	1.83E-04	1.53	5.56E-02	7.91E-04	1.42	1.99E-02	5.29E-04	2.65	
22A895_LG22_DUR_Ap1	1.98E-01	9.57E-03	1.92E-02	2.77E-04	1.44	3.49E-01	4.97E-03	1.42	2.53E-01	3.90E-03	1.54	
22A924_LG22_DUR_Ap2	5.91E-02	4.21E-03	8.13E-04	2.59E-05	3.19	9.24E-03	1.34E-04	1.45	6.79E-03	2.94E-04	4.33	
Nbblk2	2.58E-02	3.26E-04	2.96E-04	1.17E-04	39.50	4.37E-04	2.01E-04	45.98	-2.05E-04	1.25E-04	-60.95	
	1.97E-02	7.41E-04	-2.65E-04	1.87E-05	-7.03	1.16E-04	1.47E-05	12.70	1.39E-04	1.81E-04	130.14	

sample name	ng Ca	Is ± ng Ca	% Is ± ng Ca	Th/U	raw date (Ma)	Is ± date (M)	Is ± date %	Ft 238U	Ft 235U	Ft 232Th	Ft 147Sm	Rs (um)
22A912_MO22_21-BC-03_Ap2	412.63	18.35	4.45	7.05	8.1	0.1	1.42	0.68	0.63	0.63	0.89	43.06
22A913_MO22_21-BC-03_Ap3	418.82	12.54	2.99	3.18	6.9	0.2	2.30	0.61	0.56	0.56	0.87	35.01
22A914_MO22_21-BC-03_Ap4	517.53	22.41	4.33	5.11	3.4	0.1	4.11	0.63	0.58	0.58	0.88	37.19
22A915_MO22_21-BC-03_Ap5	532.21	23.80	4.47	72.41	4.9	0.1	1.43	0.68	0.63	0.63	0.90	43.29
22A916_MO22_21-BC-03_Ap6	363.18	16.45	4.53	6.07	4.9	0.1	2.93	0.66	0.62	0.62	0.89	41.36
22A917_MO22_21-BC-03_Ap7	970.69	28.88	2.98	11.09	8.0	0.1	1.62	0.78	0.75	0.75	0.93	64.62
22A918_MO22_21-BC-03_Ap8	438.79	21.48	4.90	5.21	4.5	0.1	1.96	0.65	0.60	0.60	0.88	39.05
22A920_MO22_21-BC-05_Ap2	1,721.02	67.43	3.92	7.32	3.7	0.1	1.66	0.78	0.75	0.75	0.93	66.87
22A922_MO22_21-BC-05_Ap4	12.47	0.91	7.32	4.78	2,321.4	28.3	1.22	0.74	0.71	0.71	0.92	55.81
22A895_LG22_DUR_Ap1	787.12	30.65	3.89	18.63	32.1	0.4	1.28	1.00	1.00	1.00	1.00	
22A924_LG22_DUR_Ap2	138.22	9.31	6.74	11.66	31.3	1.2	3.84	1.00	1.00	1.00	1.00	
Nbblk2	na	na	na	1.51								
	na	na	na	-0.45								

sample name	corr date (Ma)	Is ± date (M)	Is ± date %	ppm eU w/S	ppm eU (morph)	ppm eU w/S	ppm U (morph)	d ppm U (mo)
22A912_MO22_21-BC-03_Ap2	12.4	0.2	1.42	36.01	28.64	29.68	10.96	0.17
22A913_MO22_21-BC-03_Ap3	11.5	0.3	2.30	25.99	20.63	22.66	11.94	0.18
22A914_MO22_21-BC-03_Ap4	5.6	0.2	4.11	18.19	16.65	18.25	7.67	0.12
22A915_MO22_21-BC-03_Ap5	7.6	0.1	1.42	120.05	88.96	90.33	5.06	0.08
22A916_MO22_21-BC-03_Ap6	7.6	0.2	2.93	27.05	21.51	23.36	9.00	0.13
22A917_MO22_21-BC-03_Ap7	10.6	0.2	1.61	14.72	10.67	11.61	3.01	0.05
22A918_MO22_21-BC-03_Ap8	7.2	0.1	1.96	36.86	37.50	39.81	17.10	0.25
22A920_MO22_21-BC-05_Ap2	4.8	0.1	1.66	15.61	13.12	14.42	4.90	0.07
22A922_MO22_21-BC-05_Ap4	3010.9	39.0	1.30	798.12	7.09	7.10	3.39	0.05
22A895_LG22_DUR_Ap1	32.1	0.4	1.28	51.53				
22A924_LG22_DUR_Ap2	31.3	1.2	3.84	8.64				
Nbblk2								

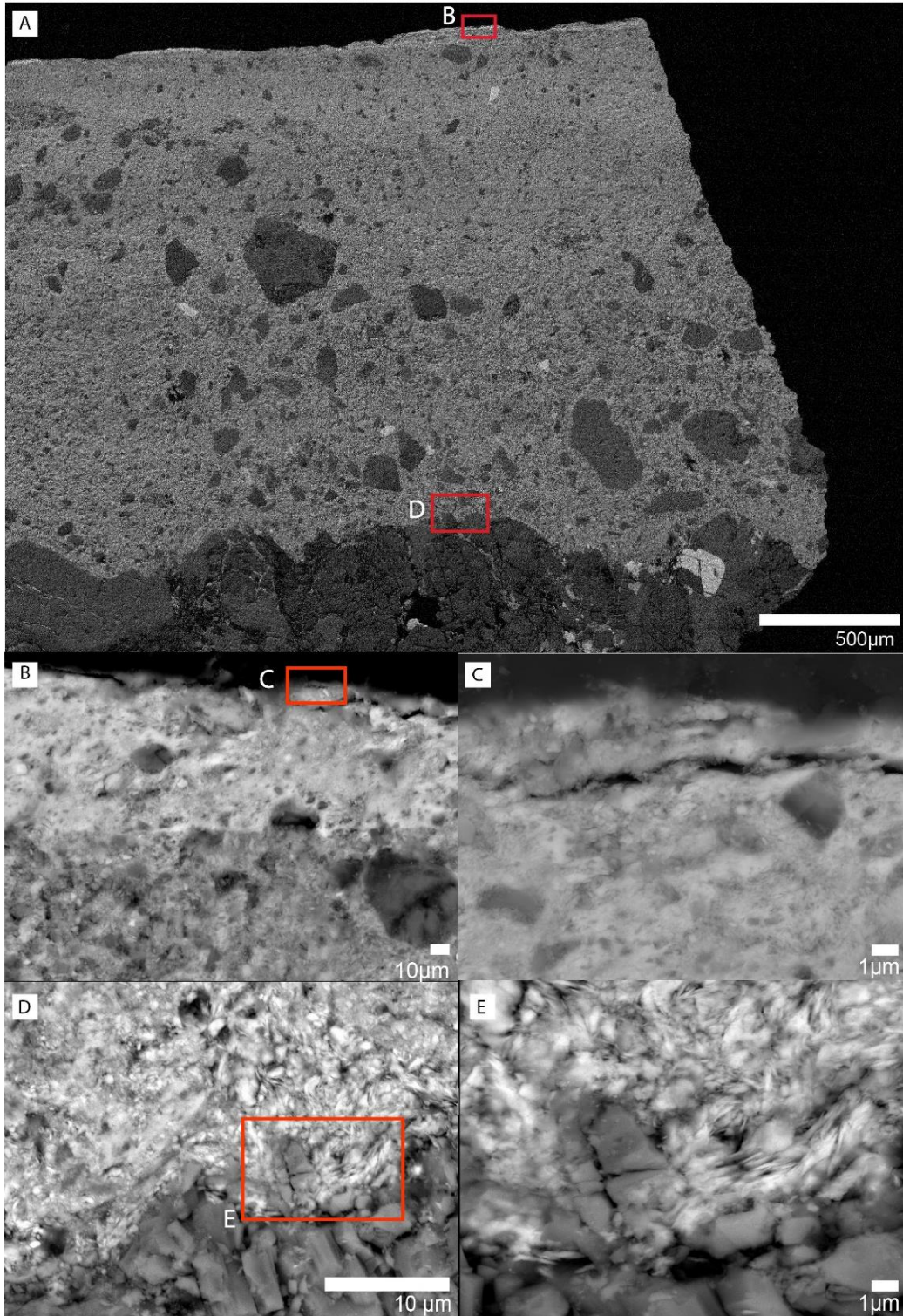


Figure A5. Multiscale BSE SEM images of 21-BC-03.

A) The fault mirror volume and contact with the host rock showing the concentration of host rock grains within the fault mirror volume. The image also shows the undulating but sharp contact between the fault mirror volume and host rock. B) Image of the fault mirror surface showing grain comminution near the fault mirror surface evidenced by nano-particles C) Image of the fault mirror surface at 1 μm scale from image B. This image demonstrates the cataclasite texture on the surface as well as the host rock grains (right) present on the surface. D) Image of the contact between the fault mirror volume and host rock. E) Image of the contact shown in D highlighting the hematite plate fragments with semi-preferred orientations and the tabular host rock morphologies.

Sample 21-BC-05 (36.0161722 N, 114.780514 W)				
Sample name	U (ppm)	Age (Ma)	2σ error	Discordance %
BC-05_2	48.361699	624.8	7.0	2.3
BC-05_5	51.075845	1319.7	30.4	0.9
BC-05_6	24.381598	362.2	5.7	0.2
BC-05_8	22.914445	623.8	7.8	0.9
BC-05_9	22.735902	1147.0	15.0	1.8
BC-05_10	167.00793	14.9	0.7	9.2
BC-05_12	641.79641	267.5	2.5	38.4
BC-05_13	127.65424	2090.2	23.4	2.4
BC-05_14	30.019488	995.3	15.3	1.2
BC-05_15	1212.0563	1645.6	24.1	1.1
BC-05_16	1430.2931	622.5	6.2	1.6
BC-05_19	1291.7924	12.2	0.4	8.8
BC-05_20	746.98302	560.6	4.5	1.1
BC-05_21	470.09983	12.9	0.7	17.5
BC-05_23	581.67072	14.1	0.5	1.0
BC-05_24	348.94386	12.5	0.6	8.3
BC-05_25	132.29979	989.5	10.6	1.6
BC-05_27	672.18238	14.2	0.6	19.4
BC-05_28	300.58413	925.0	7.5	1.0
BC-05_29	1107.6603	13.1	0.4	20.1
BC-05_30	329.14996	2070.9	18.4	0.3
BC-05_31	1593.8796	12.4	0.3	15.4
BC-05_32	151.4823	570.1	7.1	1.9
BC-05_34	460.0743	416.6	3.6	0.5
BC-05_36	262.63225	492.0	4.9	0.2
BC-05_38	253.01422	1706.4	41.1	0.6

BC-05_41	448.62141	396.5	3.7	3.3
BC-05_43	1201.0576	327.0	2.8	8.6
BC-05_44	588.50431	13.0	0.6	8.7
BC-05_45	366.32774	14.5	0.8	2.2

Table A3. U-Pb Zircon analysis results for 21-BC-05.

Results for zircon U-Pb analysis from 21-BC-05 includes Uranium concentration (ppm), U-Pb age (Ma), 2σ standard error, and % of discordance. The Miocene aged grains in each sample are highlighted.

REFERENCES

- Ault, A., Reiners, P., Evans, J., Thomson, S. (2015). Linking Hematite (U-Th)/He dating with the Microtextural Record of Seismicity in the Wasatch Fault Damage Zone, Utah, USA, *Geology*, V. 43, No. 9, P. 771-774.
- Ault, A., Jensen, J., McDermott, R., Shen, F.-A., Van Devener, B. (2019). Nanoscale evidence for temperature-induced transient rheology and postseismic fault healing, *Geologic Society of America, Geology*, V. 47, N. 12.
- Ault, A., Gautheron, C., King, G. (2019). Innovations in (U-Th)/He, Fission Track, and Trapped Charge Thermochronometry with Applications to Earthquakes, Weathering, Surface-Mantle Connections, and the Growth and Decay of Mountains, *American Geophysical Union: Advancing Earth and Space Science 100*, Tectonics Section.
- Ault, A. (2020). Hematite Fault Rock Thermochronometry and Textures Inform Fault Zone Processes, *Journal of Structural Geology*, V. 133.
- Anderson, R., Longwell, C., Armstrong, R., et al. (1972). Significance of K-Ar Ages of Tertiary Rocks from the Lake Mead Region, Nevada-Arizona, *Geological Society of America Bulletin*, V. 83, P. 273-288.
- Anderson, R., Beard, S. (2010). Geology of Lake Mead Region: An Overview, Umhoefer, P., Beard, S., Lamb, M., eds., Miocene Tectonics of the Lake Mead Region, Central Basin and Range: *Geological Society of America*, Special Paper 463, P. 1-28.
- Beard, L.S., Anderson, Z.W., Felger, T.J., and Seixas, G.B. (2014). Geologic framework of thermal springs, Black Canyon, Nevada and Arizona: *U.S. Geological Survey Open-File Report 2013-1267-B*, P. 65.
- Bohannon, R. (1979). Strike-slip Faults of the Lake Mead Area in Southern Nevada, Pacific Coast Paleogeography Symposium 3: Cenozoic Paleogeography of the Western United States, *Society of Sedimentary Geology*, Pacific Section.
- Bowring, S., and Schmitz, M. (2003). High-Precision U-Pb Zircon Geochronology and the Stratigraphic Record, *Reviews in Minerals and Geochemistry*, V. 53, P. 305-326.
- Brace, W., Byerlee, J. (1966). Stick-Slip as a Mechanism for Earthquakes, *Science*, V. 153, No. 3739, P. 990-992.
- Calzolari, G., Rossetti, F., Ault, A., Lucci, F., Olivetti, V., Nozaem, R. (2018). Hematite (U-Th)/He Thermochronometry Constrains Intraplate Strike-Slip Faulting on the Kuh-e-Faghan Fault, Central Iran, *Tectonophysics*, V. 728-729, P. 41-54.

- Calzolari, G., Ault, A., Hirth, G., McDermott, R. (2020). Hematite (U-Th)/He Thermochronometry Detects Asperity Flash Heating During Laboratory Earthquakes, Geologic Society of America, *Geology*, V. 48.
- Catling, D., Moore, J. (2003). The Nature of Coarse-grained Crystalline Hematite and its Implications for the Early Environment of Mars, *Icarus*, V. 165, P. 277-300.
- Cherniak, D., Lanford, W., Ryerson, F. (1991). Lead Diffusion in Apatite and Zircon Using Ion Implantation and Rutherford Backscattering Techniques, *Geochimica et Cosmochimica Acta*, V. 55, I. 6, P. 1663-1673.
- Cherniak, D., Watson, E. (2001). Pb Diffusion in Zircon, *Chemical Geology*, V. 172, I. 1-2, P. 5-24.
- Collettini, C., Viti, C., Tesei, T., Mollo, S. (2013). Thermal Decomposition Along Natural Carbonate Faults During Earthquakes, *Geology*, V. 41, I. 8, P. 927-930.
- Cowan, D. (1999). Do Faults Preserve a Record of Seismic Slip? A Field Geologist's Opinion, *Journal of Structural Geology*, V. 21, P. 995-1001.
- Crowley, J., Schoene, B., Bowring, S. (2007). U-Pb Dating of Zircon in the Bishop Tuff at the Millennial Scale, *Geology*, V. 35, No. 12, P 1123-1126.
- Duebendorfer, E., Wallin, E. (1991). Basin Development and Syntectonic Sedimentation Associated with Kinematically Coupled Strike-slip and Detachment Faulting, Southern Nevada, *Geology*, V. 19, P 87-90.
- Eaton, G. (1984). The Miocene Great Basin of Western North America as an Extending Back-Arc Region. *Tectonophysics*, 102(1), 275–295.
- Ehlers, T., Armstrong, P., Chapman, D. (2001). Normal Fault Thermal Regimes and the Interpretation of Low-Temperature Thermochronometer, *Physics of the Earth and Planetary Interiors*, V. 126, Issues 3-4, P. 179-194.
- Elhers, T., Farley, K. (2003). Apatite (U-Th)/He thermochronometry: Methods and Applications to Problems in Tectonics and Surface Processes, *Earth and Planetary Science Letters*, V. 206, I. 1-2, P. 1-14.
- England, P., Molnar, P. (1990). Surface Uplift, Uplift of Rocks, and Exhumation of Rocks, *Geology*, V. 18, P. 1173-1177.
- Evans, J., Prante, M., Janecke, S., Ault, A., Newell, D. (2014). Hot Faults: Iridescent slip surfaces with metallic luster document temperature ancient seismicity in the Wasatch fault zone, Utah, USA, Geologic Society of America, *Geology*, V. 42, No. 7, P. 623-626.

- Fagereng, A., and Toy, V. (2011). Geology of the Earthquake Source: an Introduction, from: Fagereng, A., Toy, V., and Rowland, J (eds.), *Geology of the Earthquake Source: A Volume in Honour of Rick Sibson, Geological Society of London, Special Publications*, 359, P. 1-16.
- Farley, K., Wolf R., Silver L. (1996). The Effects of Long Alpha-Stopping Distance on (U-Th)/He Ages, *Geochimica et Cosmochimica*, V. 60, P. 4223-4229.
- Farley, K. (2000). Helium Diffusion from Apatite: General Behavior Illustrated by Durango Fluorapatite, *Journal of Geophysical Research*, V. 105, No. B2, P. 2903-2914.
- Farley, K., Stockli, D. (2002). (U-Th)/He Dating of Phosphates: Apatite, Monazite, and Xenotime, *Reviews in Mineralogy and Geochemistry*, V. 48, P. 559-577.
- Farley, K., Flowers, R. (2012). (U-Th)/Ne and Multidomain (U-Th)/He Systematics of a Hydrothermal Hematite from Eastern Grand Canyon, *Earth and Planetary Science Letters*, 359-360, P. 131-140.
- Farley, K. (2018). Helium Diffusion Parameters of Hematite from a Single-Diffusion-Domain Crystal, *Geochimica et Cosmochimica*, V. 231, P. 117-129.
- Faulkner, D., Jackson, C., Lunn, R., Schlische, R., Shipton, Z., Wibberley, C., Withjack, M. (2010). A Review of Recent Developments Concerning the Structure, Mechanics, and Fluid Flow Properties of Fault Zones, *Journal of Structural Geology*, V. 32, I. 11.
- Faulds, J., Mawer, C, and Geissman, J. (1990) Possible Modes of Deformation Along “Accommodation Zones” in Rifted Continental Crust: An Example from the Southern Basin and Range Province, in Wernike, P., eds., *Basin and Range Extensional Tectonics near the Latitude of Las Vegas, Nevada*. P. 39-45.
- Faulds, J., Feuerbach, D., Miller, C., and Smith, E. (2001). Cenozoic Evolution of the Northern Colorado River Extensional Corridor, Southern Nevada and Northwest Arizona, *Utah Geological Association, Publication 30, Pacific Section American Association of Petroleum Geologists GB78*, P. 239-271.
- Faulds, J. (2022) Plate Boundary Influences on the Complex Miocene Strain Field of the Lake Mead Region and Northern Colorado River Extensional Corridor, Southern Nevada and Northwestern Arizona: From Propagating Rifts to Indenter Tectonics, *Geological Society of America Abstracts with Programs*, V. 54, No. 2.
- Felger, T., Beard, S. (2010). Geologic Map of Lake Mead and Surrounding Regions, Southern Nevada, Southwestern Utah, and Northwestern Arizona, in Umhoefer, P., Beard, S., and Lamb M., eds., *Miocene Tectonics of the Lake Mead Region, Central Basin and Range: Geological Society of America Special Publication 463*, P. 29-38.

- Felger, T., Beard, S., Anderson, Z., Fleck, R., et al. (2014). Preliminary Geologic Map of Black Canyon and Surrounding Region, Nevada and Arizona, *USGS open-file report 2013-1257-A*.
- Feuerbach, D., Smith, E., Walker, J., et al. (1993). *The Role of the Mantle During Crustal Extension: Constraints from Geochemistry of Volcanic Rocks in the Lake Mead Area, Nevada and Arizona*, V. 105, P 1561-1575.
- Flowers, R., Ketcham, R., Schuster, D., Farley, K. (2009). Apatite (U-Th)/He Thermochronometry Using Radiation Damage Accumulation and Annealing Model, *Geochimica et Cosmochimica*, V. 73, I. 8, P. 2347-2365.
- Gans, P., Bohrsen, W. (1998). Suppression of Volcanism During Rapid in the Basin and Range Province, United States, *Science*, V. 279.
- Gonclaves, C., Gonclaves, L., Hirth, G. (2015). The Effects of Quartz Recrystallization and Reaction on Weak Phase Interconnection, Strain Localization, and Evolution of Microstructure, *Journal of Structural Geology*, V. 71, P. 24-40.
- Guo, H., Barnard, A. (2013). Naturally Occurring Iron Oxide Nanoparticles: Morphology, Surface Chemistry, and Environmental Stability, *Journal of Materials Chemistry A*, V. 1, P. 27-42.
- Grim, R., Bradley, W. (1940). Investigation of the Effect of Heat on the Clay Minerals Illite and Montmorillonite, *Journal of the American Ceramic Society*, V. 23, I. 8, P. 242-248.
- Hinz, N., Dee, S., Smith, E., Johnsen, R. (2018). Update on the Timing, Magnitude of Offset, and Geomechanics of the Southern Part of the Lake Mead Fault System, Nevada, Joint 70th Rocky Mountain Annual Section/114th Cordilleran Annual Section Meeting. *Geological Society of America*, Abstracts with Programs, V. 50, No. 5
- Isambert, A., Valet, J.-P., Gloter, A., and Guyot, F. (2003). Stable Mn-magnetite Derived From Mn-siderite by Heating in Air, *Journal of Geophysical Research*, V. 108, P. 2283.
- Ishikawa, T., Tanimizu, M., Nagaishi, K. et al. (2008). Coseismic fluid–rock interactions at high temperatures in the Chelungpu fault, *Nature Geoscience* 1, P. 679–683.
- Jackson, S., Pearson, N., Griffin, W., Belousova, E. (2004). Application of Laser Ablation-Inductively Coupled Plasma-Mass Spectrometry to In Situ U-Pb Zircon Geochronology, *Chemical Geology*, V. 211, I. 1-2, P. 47-69.

- Kameda, J., Ujiie, K., Yamaguchi, A., Kimura, G. (2011). Smectite to Chlorite Conversion by Frictional Heating Along a Subduction, *Earth and Planetary Science Letters*, V. 305, I. 1-2, P. 161-170.
- Ketcham, R., Donelick, R., Carlson, W. (1999) Variability of Apatite Fission-Track Annealing Kinetics: III. Extrapolation to Geologic Timescales, *American Mineralogist*, V. 84, P. 1235-1255.
- Ketcham, R., Guenther, W., Reiners, P. (2013) Geometric Analysis of Radiation Damage Connectivity in Zircon, and its Implications for Helium Diffusion, *American Mineralogist*, V. 98, P. 350-360.
- Knipe, R. (1989). Deformation Mechanisms— Recognition from Natural Tectonites, *Journal of Structural Geology*, V. 11, No. ½, P. 127-146.
- Kron, Andrea & Heiken, Grant. (1980) Geothermal Gradient Map of the Conterminous United States, map, Los Alamos, New Mexico, University of North Texas Libraries, UNT Digital Library, crediting UNT Libraries Government Documents Department.
- Langenheim, V., Beard, S., Faulds, J. (2010). Implications of Geophysical Analysis on Basin Geometry and Fault Offsets in the Northern Colorado River Extensional Corridor and Adjoining Lake Mead Region, Nevada and Arizona, *Geologic Society of America*, Special Paper 463, Umhoefer, J., Beard, S., Lamb, M, eds, Miocene Tectonics of the Lake Mead Region, Central Basin and Range, P. 39-59.
- McDermott, R., Ault, A., Evans, J., Reiners, P. (2017). Thermochronometric and textural evidence for seismicity via asperity flash heating on exhumed hematite fault mirrors, Wasatch fault zone, UT, USA, *Earth and Planetary Science Letters*, V. 471, P. 85-93.
- McIntosh, R., Sharp, J., Wilburn, F. (1990). The Thermal Decomposition of Dolomite, *Thermochimica Acta*, V. 165, I. 2, P. 281-296.
- Molnar, P., England, P. (1990). Late Cenozoic Uplift of Mountain Ranges and Global Climate Change: Chicken or Egg?, *Nature*, V. 346.
- Moser, A., Evans, J., Ault, A., et al. (2017). (U-Th)/He Thermochronometry Reveals Pleistocene Punctuated Deformation and Synkinematic Hematite Mineralization in the Mecca Hills, Southernmost San Andreas Fault Zone, *Earth and Planetary Science Letters*, V. 476, P. 87-99.
- Nathenson, M., Guffanti, M. (1987). Compilcation of Geothermal-Gradient Data in the Conterminous United States, USGS open-file report, Series. 87-592.
- Odlum, M., Ault, A., Channer, M., Calzolari, G. (2021). Seismicity Recorded in Hematite Fault Mirrors in the Rio Graft Rift, *Geosphere*.

- Pluymakers, A. and Royne, A. (2017). Nanograin Formation and Reaction-Induced Fracturing Due to Decarbonation: Implications for the Microstructures of Fault Mirrors, *Earth and Planetary Scientific Letters*, V. 476, P. 59-68.
- Rabinowitz, H., Polissar, P., Savage, H. (2017). Reaction Kinematics of Alkenone and n-Alkane thermal alteration at seismic timescales, *Geochemistry, Geophysics, Geosystem*, V. 18, I. 1, P. 204-219.
- Reiners, P., Ehlers, T., Zeitler, P. (2005). Past, Present, and Future of Thermochronometry, *Reviews in Mineralogy and Geochemistry*, V. 58, P. 1-18.
- Rice, J. (2006). Heating and Weakening of Faults During Earthquake Slip, *Journal of Geophysical Research, Solid Earth*, V. 111, I. B5.
- Rowe, C. and Griffith, A. (2015). Do Faults Preserve a Record of Seismic Slip: A Second Opinion, *Journal of Structural Geology*, V. 78, P. 1-26.
- Savage, H., Polissar, P., Sheppard, R., Rowe, C., Brodsky, E. (2014). Biomarkers heat up during earthquakes: New evidence of seismic slip in the rock record, *Geology*, V. 42, I.2, P. 99–102.
- Savage, H., Polissar, P. (2019). Biomarker Thermal Maturity Reveals Localized Temperature Rise From Paleoseismic Slip Along the Punchbowl Fault, CA, USA. *Geochemistry, Geophysics, Geosystems*, V. 20, I. 7, P. 3201-3215.
- Schoene, B. (2014). U-Th-Pb Geochronology, *Treatise on Geochemistry*, 2nd Edition, P. 341-370.
- Sheppard, R., Polissar, P., Savage, H. (2015). Organic Thermal Maturity as a Proxy for Frictional Fault Heating: Experimental Constraints on Methylphenanthrene Kinetics at Earthquake Timescales, *Geochimica et Cosmochimica Acta*, V. 151, P. 103-116.
- Sibson, R. (1983). Continental Fault Structure and the Shallow Earthquake Source, *Journal of Geologic Society*, V. 180, P. 741-767.
- Siman-Tov, S., Aharonov, E., Sagy, A., Emmanuel, S. (2013). Nanograins from Carbonate Fault Mirrors, *Geology*, V. 41, P. 703-706.
- Smith, E. (1984). Map 81: Geologic Map of the Boulder Beach Quadrangle, Nevada: *Nevada Bureau of Mines and Geology*, 1:24,000.

- Spiegel, C., Kohn, B., Belton, D., et al. (2009). Apatite (U-Th-Sm)/He Thermochronology of Rapidly Cooled Samples: The Effect of He Implantation, *Earth and Planetary Science Letters*, V. 285, I. 1-2, P. 105-114.
- Stockli, D., Farley, K., Dumitru, T. (2000). Calibration of (U-Th)/He Thermochronometer on an Exhumed Fault Block, White Mountains, California, *Geology*, V. 28, P. 983-986.
- Thakur, P., Huang, Y., Kaneko, Y. (2020). Effects of Low-Velocity Fault Damage Zones on Long-term Earthquakes on Mature Strike-slip Faults, *Journal of Geophysical Research: Solid Earth*, V. 125, I. 8.
- Verberne, B., Plumper, O., Spiers, C. (2019). Nanocrystalline Principal Slip Zones and Their Role in Controlling Crustal Fault Rheology, *Minerals*, V. 9, 328.
- Vermeesh, P. (2018). IsoplotR: a free and open toolbox for geochronology. *Geoscience Frontiers*, V. 9, P. 1479-1493.
- Weber, M., & Smith, E. (1987). Structural and Geochemical Constraints on the Reassembly of Disrupted Mid-Miocene Volcanoes in the Lake Mead-Eldorado Valley Area of the Southern Nevada, *Geology*, V. 15, P. 553-556.
- Wernicke, B., England, P., Sonder, L., Christiensen, R. (1987). Tectonomagmatic Evolution of Cenozoic Extension in North America Cordillera, *Geological Society, London, Special Publications*, V. 28, P. 203-221.
- Wolf, R., Farley, K., Silver, L. (1996). Helium Diffusion and Low-Temperature Thermochronometry of Apatite, *Geochimica et Cosmochimica Acta*, V. 60, No. 21, P. 4231-4240.
- Zeitler, P., Herczeg, A., McDougall, I., Honda, M. (1987). U-Th-He Dating of Apatite: A Potential Thermochronometer, *Geochimica et Cosmochimica Acta*, V. 51, P. 2865-2868.
- Zuza, A., Cao, W., Hinz, N., DesOrmeau, J., Odlum, M., Stockli, D. (2019). Footwall Rotation in the Regional Detachment Fault System: Evidence for Horizontal-Axis Rotational Flow in the Miocene Searchlight Pluton, NV, *Tectonics*, V. 38, P. 2506-2539.

CURRICULUM VITAE

Molly E. Pickerel

Geoscience Department
4504 S. Maryland Pkwy
Las Vegas, NV 89154
Email: mollypickerel@gmail.com

Education

- Master's student - University of Nevada, Las Vegas – May 2023
- Honors B.S., Geology - University of Oregon, Eugene, OR - June 2019
- A.A.O.T., General - Chemeketa Community College, Salem, OR - June 2013

Research

- *Master's Thesis*
Characterization of Bedrock Fault Scarps and Hematite Fault Mirrors in the Northern Colorado River Extensional Corridor Near Lake Mead, Nevada
Advised by Dr. Margo Odlum
- *Honors Senior Thesis*
Characterizing Differential Stress and Strain Rates of Recrystallized Quartz from the Porphyry Copper Deposit in Butte, Montana through Paleopiezometry
Advised by PhD candidate Marisa D. Acosta, Dr. Mark H. Reed, & Dr. James M. Watkins
- *Lab Assistant in Reed Lab* – August 2018- 2019
- *Post-baccalaureate Research Project*
Surface roughness and overgrowth dynamics: the effect of substrate micro-topography on calcite growth and Sr uptake
Advised by PhD candidate Marisa D. Acosta & Dr. James M. Watkins

Internship Experience

- *Lawrence Livermore National Laboratory* –Summer intern – May-August 2021
Remote internship working on Lonsdaleite research project using Diamond Anvil Cells and Raman Spectroscopy

Skills

- *Field Skills*

Strike and dip measurements; sighting to landmarks; bedrock mapping; hand sample mineral identification; cross section construction and interpretation
- *Sample Prep*

Microprobe round preparation and polishing; hand sample/slab polishing; C-coating samples; Mineral separation processes, Apatite and Zircon picking for dating analysis
- *Data collection and interpretation*
 - Scanning electron microscope (SEM) – used an FEI Quanta environmental SEM to image thin sections with back-scattered electron (BSE) detector, secondary electron (SE) detector, and a cathodoluminescence (CL) detector. Collected and interpreted elemental data with Pathfinder electron dispersive x-ray spectrometry (EDS)
 - 3D SEM-SE image reconstruction – SE images collected on a Helios Focused Ion Beam (FIB) used to generate 3D reconstructions of surfaces and quantify surface roughness parameters in the MeX software.
 - Thin section petrography – Leica Microscope operation and image collecting through Leica Software. Mineral ID and rock history interpretation using textural relations.
- *Computation*
 - SOLVEQ software for determining aqueous equilibrium activity coefficients – given concentrations of elements to determine pH
 - R software for data analysis – Given published work with errors; calculated standard errors, and statistical significance
 - Adobe Illustrator – Used to create scientific figures and academic posters
 - Geographic Information Systems (GIS) – Learned to input data sets, create maps, manipulate digital representation of discrete space, digitized multiple geologic features

- Leica Suite Software for stereograph imaging
- Helium Fission Track (HeFTy) – (U-Th)/He Thermochronometry thermal history modeling program

Field Experience

- Butte, Montana- field assistant for Marisa Acosta's PhD project finding and characterizing alteration zone in the Butte granite, touring and collecting in Montana Resource Mine, and ascertaining specific samples from the core library at Montana Tech.
- Sunset Bay, Oregon- structure course project fault mapping
- Roseburg, Oregon- structure course project mapping the Roseburg Folds
- Dillon, Montana- field camp course project classic mapping and reporting of Frying Pan Gulch and Block Mountain.
- Central Oregon- field camp course project collecting fossils and creating a stratigraphic column of the John Day Formation.
- The Wallowa Mountains, Oregon- field camp course project characterizing feeder vents of Columbia River Basalts and mapping/charactering glacial moraines using MATLAB.
- Lake Mead, NV- master's thesis data collection including sample collection, orientation measurements, and geologic interpretation

Specialized Skills

- Brunton compass measurements
- Billet cutting & thin section preparation
- Thin section & microprobe sample polishing
- Hand sample/slab polishing
- Puck casting in epoxy
- Carbon coating for electron microscopy
- Image collecting on the scanning electron microscope (SEM) back-scattered electron (BSE), secondary electron (SE), cathodoluminescence detection (CL) and use of Pathfinder electron dispersive x-ray spectrometry (EDS)
- Leica Microscope operation and image collecting through Leica Software

- SOLVEQ software for determining aqueous equilibrium
- R software for data analysis
- Jacob's Staff and Abnee Level for stratigraphic
- Vertebrate Fossil surveying and collection
- Picking apatite and zircon for dating
- Loading Diamond Anvil Cells

Instrument and Software Experience

Techniques and instruments, I have used with guided supervision and/or have been exposed to the theory behind and its application to geological samples.

- Electron Probe MicroAnalysis (EPMA) analyze trace elements in quartz
- Focused ion beam (FIB) sample extraction in preparation for further analysis
- Transmission electron microscopy (TEM) to look for nanoparticles, observed EDS data collection and diffraction pattern collection and interpretation.
- Cold seal pressure vessel for experimental crystal growth
- CHIM software for determining heterogeneous aqueous equilibrium
- MeX software for 3d reconstructions of stereoscopic scanning electron microscope images
- MountainsSEM software of 3D reconstructions of stereoscopic scanning electron microscope images
- CrystalMaker analyzing crystal structures
- Diamond Anvil Cells for high pressure experiments
- BADGER Rock Crusher
- Chipmunk Jaw Crusher
- Disk Grinder for rock crushing
- Water table gravity mineral separator
- FRANTZ magnetic mineral separator
- Stereograph Leica software for imaging
- Geographic Information Systems (GIS)
- Laser heating apatite packets
- Running software for apatite samples at ARDHL
- Raman Spectroscopy (experience observing)

Courses Instructed

- GEOG 104 (online) Fall 2020-Spring 2021
- GEOL 101 (grading online) Fall 2021
- GEOL 220L (in person) Fall 2021
- GEOG 104 (in person) Spring 2022

Academic Honors & Awards

- *2022 UNLV Geosymposium 'Outstanding 100-level Teaching Assistant'*
- *2021 UNLV Geosymposium 'Best Graduate Student Poster'*
- *Joint Undergrad-graduate Mentorship Program (JUMP) program mentee*
 - The JUMP program seeks to enhance the retention of undergraduates in all areas of STEM through direct interaction with graduate student mentors.
 - Mentors: Marisa Acosta 2017-2018, Ellen Olsen 2018-2019
- *Youngquist Fellowship Award recipient 2018*
- *David Krinsley Memorial Award recipient 2018*
- *Emeritus Faculty Tribute Endowment Fund recipient 2018*
- *Chemeketa Scholars Award recipient 2010*

Affiliations

- Society of Economic Geologists (SEG)
 - Treasurer for UNLV Chapter 2020-2021
 - Secretary for UNLV Chapter 2021-2022
- Geochemical Society Student Member 2018-2019, 2021-present
- Association of Women Geoscientists
 - President for UNLV Chapter Spring 2023
 - Vice President for UNLV Chapter Fall 2022
 - Secretary for UNLV Chapter 2021-2022
 - Member for UNLV Chapter 2020-2021
- American Association of Petroleum Geologist (AAPG) Student Member 2018-2019
- American Geophysical Union (AGU) Student Member 2018-2019

- Sigma Gamma Epsilon (National Honors Society for Earth Sciences) Member 2018-2019

Events Participated in/Organized

- 2023 18th Annual GeoSymposium Field Trip (April 29th, 2023) – leader and organizer
- 2023 18th Annual GeoSymposium (April 28th, 2023) – head coordinator
- AWG Geoscientist Careers Seminar (December, 2022) – host
- AWG Resume workshop (October, 2022) – Co-organizer
- AWG/SEG Fall 2022 Field day (September, 2022) – Co-organizer
- 2022 17th Annual GeoSymposium (April 2022) – participant
- SEG Nelson day trip (February, 2022) – Officer lead
- AAPG/AWG 2022 ‘Save Our Sands’ Beach Clean-up (Spring 2022) – Participant
- SEG Tonopah field trip (October, 2021) – Officer lead, co-organizer
- SEG Epithermal Deposits Seminar (April 24th, 2021) – Co-organizer, co-host
 - Event raised \$15,000 for UNLV chapter
- 2021 16th Annual GeoSymposium (April 2021) – participant